



**GADOLINIUM OXIDE / SILICON THIN FILM HETEROJUNCTION SOLID-
STATE NEUTRON DETECTOR**

THESIS

Christopher M. Young, Major, USA

AFIT/GNE/ENP/10M-10

DEPARTMENT OF THE AIR FORCE

AIR UNIVERSITY

AIR FORCE INSTITUTE OF TECHNOLOGY

Wright-Patterson Air Force Base, Ohio

APPROVED FOR PUBLIC RELEASE; DISTRIBUTION UNLIMITED

The views expressed in this thesis are those of the author and do not reflect the official policy or position of the United States Air Force, Department of Defense, or the United States Government.

AFIT/GNE/ENP/10M-10

GADOLINIUM OXIDE / SILICON THIN FILM HETEROJUNCTION SOLID-STATE
NEUTRON DETECTOR

THESIS

Presented to the Faculty

Department of Engineering Physics

Graduate School of Engineering and Management

Air Force Institute of Technology

Air University

Air Education and Training Command

In Partial Fulfillment of the Requirements for the
Degree of Master of Science in Nuclear Engineering

Christopher M. Young, BS

Major, USA

March 2010

APPROVED FOR PUBLIC RELEASE; DISTRIBUTION UNLIMITED

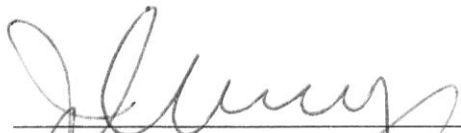
AFIT/GNE/ENP/10M-10

GADOLINIUM OXIDE / SILICON THIN FILM HETEROJUNCTION SOLID-STATE
NEUTRON DETECTOR

Christopher M. Young, BS

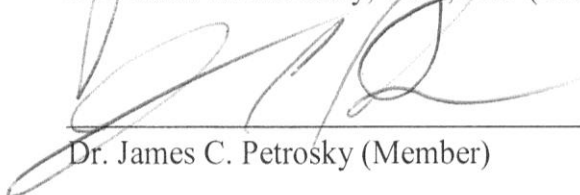
Major, USA

Approved:



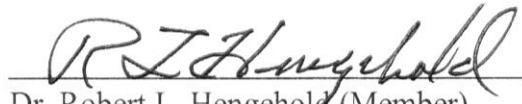
LTC John W. McClory, USA, PhD (Chairman)

12 MAR 10
Date



Dr. James C. Petrosky (Member)

11 Mar 10
Date



Dr. Robert L. Hengehold (Member)

12 Mar 10
Date

Abstract

The internal conversion electron emission from the de-excitation of the Gd-158m nucleus was explored as a means for neutron detection. Thin film gadolinium oxide (Gd_2O_3) and p-type silicon heterojunction diodes were produced using a supercritical water deposition process. Pulse height spectroscopy was conducted on the novel diodes while they were subjected to a moderated plutonium-beryllium (PuBe) source flux of 10^4 thermal neutrons/ cm^2 s. Coincident gamma spectroscopy was employed to verify the 1107.6 keV photon emissions from the diode indicative of successful neutron capture by Gd-157 and the subsequent de-excitation of the Gd-158m nucleus. Neutron capture in the diodes could not be confirmed experimentally. The diodes were found to be sensitive to gamma rays between 10 and 20 keV.

Dedications

To my family.

Table of Contents	Page
Abstract	iv
Dedications	v
Table of Contents.....	vi
List of Figure.....	ix
List of Tables	xiv
List of Abbreviations	xv
I. INTRODUCTION	1
1.1 Theory of Special Nuclear Material Detection	2
1.2 Problem Statement	7
1.3 Document Organization	7
II. BACKGROUND.....	8
2.1 Properties of Detector Materials	8
2.2 Detector Technologies.....	13
2.3 Gadolinium.....	14
III. EXPERIMENTAL APPROACH.....	17
3.1 Introduction	17
3.2 Supercritical Gadolinium Oxide Deposition.....	17
3.3 Diode Fabrication	22
3.4 Initial Device Characterization.....	24
3.5 Feasibility of Neutron Detection	26
3.6 Diode Signal and Neutron Flux.....	30
3.7 Experimental Concept	33
3.7.1 Goal	33
3.7.2 Coincidence Measurements	33
3.7.3 Neutron Source	35
IV. EXPERIMENT, RESULTS, AND ANALYSIS	37
4.1 Experimental Design & Apparatus	37

4.1.1 Construction of the Neutron Howitzer	37
4.1.2 Coincident Gamma-Ray Instrumentation Scheme	43
4.1.3 Establishing the laboratory	46
4.2 Calibration of the Coincident Gamma-Ray Instrumentation	48
4.3 Neutron Detection Experiment using Neutron Howitzer	54
4.4 Neutron Flux Measurement and Calibration	63
4.5 Neutron Detection Experiment using the Graphite Pile	73
4.6 Sr-90 Experiment	87
4.7 Cesium-137 Experiment	95
V. CONCLUSIONS	99
5.1 Conclusions	99
5.2 Recommendations for future work	100
5.2.1 Investigate the photon sensitivity.	100
5.2.2 Calibrate the diode spectrum.	100
5.2.3 Diode modeling.	101
APPENDICES	102
Appendix A: Diode Active Volume and Coincident Counting Time	103
Appendix B: SNM Spontaneous Neutron Emission Rate Calculation	105
Appendix C: PuBe Source Neutron Emission Rate Calculation [30]	106
Appendix D: MCNP Code for Neutron Howitzer Design	108
D.1 Aluminum Howitzer	108
D.2 PVC Howitzer	111
Appendix E: MCNP Code for Graphite Pile Differential Neutron Flux	114
E.1 Differential Neutron Flux at the diode	114
E.2 Differential Neutron Flux at the diode with a Cd absorber	117
Appendix F: Source and Detector Data Sheets	120
F.1 PuBe Source.	120
F.2 Co-60 Source	121
F.3 LaBr(Ce) Detector Data Sheets	122

Appendix G: BF ₃ Calculations	123
G.1 Calculated thermal neutron flux using a BF ₃ detector	123
G.2 Neutron attenuation of the Cd shield	125
G.3 Calibration of the BF ₃ Tube using the Standard Graphite Pile	126
Appendix H: Sr-90 Experiment Calculations	128
H.1 Determine the Beta flux into the diode from the Sr-90 source	128
H.2 Sr-90 Source Protocol	133
Appendix I: MCNP Code for gamma ray energy deposition in the diode	136
I.1 Energy deposition in the diode from a PuBe photon spectrum	136
I.2 Energy deposition in the Cd-covered diode from a PuBe photon spectrum	141
Appendix J: Instrument Settings	146
Appendix K: Equipment List	148
REFERENCES	151

List of Figures	Page
FIG. 1 THE TOTAL NEUTRON CROSS-SECTION OF SEVERAL NUCLIDES USED IN NEUTRON DETECTORS.	9
FIG. 2 TOTAL NEUTRON CROSS-SECTIONS OF SELECTED GADOLINIUM ISOTOPES. OF THE FIVE STABLE ISOTOPES, MASS NUMBERS 157, 155, AND 158 HAVE THE HIGHEST CROSS-SECTIONS.	11
FIG. 3 A CONVERSION LAYER DIODE (TOP LEFT), AN INTRINSIC DIODE (TOP RIGHT), AND A GAS COUNTER (BOTTOM). IN THE CONVERSION LAYER DIODE, AN INCIDENT NEUTRON SAMPLES THE MODERATING LAYER AND EITHER PASSES THROUGH IT WITHOUT INTERACTION (1C) OR SLOWS UNTIL A REACTION OCCURS (1A). A NUCLEAR REACTION PRODUCT CREATES IONIZATION WITHIN THE ACTIVE REGION OF THE DIODE (1B) BUT MAY NOT DEPOSIT ALL OF ITS ENERGY BEFORE IONIZING AN INACTIVE REGION. AN INTRINSIC DIODE DEPLETES THE NEUTRON-REACTIVE LAYER. A NEUTRON CAN EITHER PASS WITHOUT INTERACTION (2C) OR REACT TO FORM AN IONIZING PARTICLE (2A) WHICH IS ALREADY WITHIN THE ACTIVE REGION (2B). A GAS DETECTOR OPERATES ON THE PRINCIPLE THAT THE IONIZING PARTICLE BORN OF THE NEUTRON INTERACTION (3A) DEPOSITS ITS ENERGY BY IONIZING GAS MOLECULES (3B) WHILE THE CHARGE CLOUD IS PULLED INTO A COLLECTING WIRE UNDER A HIGH BIAS.	14
FIG. 4 THE SUMMARIZED DE-EXCITATION SCHEME OF THE EXCITED ^{158}Gd NUCLEUS OF THE $^{157}\text{Gd} (n, \gamma) ^{158}\text{Gd}$ REACTION [16][17].	16
FIG. 5 THE STRUCTURE OF CUBIC AND MONO-CLINIC GADOLINIUM OXIDE. THE DOTS REPRESENT Gd ATOMS [21].	18
FIG. 6 A SCHEMATIC REPRESENTATION OF THE SUPER-CRITICAL WATER CHEMICAL REACTOR (SCWR) SUCCESSFULLY USED AT THE UNIVERSITY OF NEBRASKA, LINCOLN TO DEPOSIT CUBIC Gd_2O_3 ON P-TYPE SILICON. (1) PURIFIED WATER TANK. (2) HIGH PRESSURE PUMPS. (3) FIRST STAGE SOLVENT HEATER. (4) SECOND STAGE SOLVENT HEATER. (5) FILTER BASKET CONTAINING Gd_2O_3 . (6) EXPANSION NOZZLE AND P-TYPE SILICON TARGET. T1, T2, AND T3 ARE TEMPERATURE PROBES.	19
FIG. 7 A TYPICAL PHASE DIAGRAM OF MATTER SHOWING THE LOCATION OF THE CRITICAL POINT, ABOVE WHICH THE MATERIAL ACTS AS A SUPERCRITICAL FLUID.	19
FIG. 8 AN OPTICAL MICROSCOPE VIEW OF THE Gd_2O_3 FILM SHOWING THE FORMATION OF CRYSTALLITES. .	21
FIG. 9 A SAMPLE OF Gd_2O_3 ON SI WITH CONTACTS. (A) A DEPICTION OF THE SAMPLE WITH 25 CONTACTS SPUTTERED OVER THE GADOLINA LAYER. (B) AN END-VIEW OF THE SAMPLE DEPICTING THE CONTACT GEOMETRY (EXAGGERATED DIMENSIONS). (C) A DIMENSIONAL DEPICTION OF THE CROSS-SECTION OF A SINGLE DIODE USING THE BASE OF THE GOLD CONTACT AS A REFERENCE POINT.	24
FIG. 10 THE I(V) RESPONSE FOR CONTACT 5 OF DIODE SAMPLE 1 SHOWING RECTIFICATION AT VARIOUS TEMPERATURES.	25
FIG. 11 THE $1/C^2$ VS. BIAS [V] PLOT FOR CONTACT 5 OF DIODE SAMPLE 1 AT ROOM TEMPERATURE. THE X-AXIS UNITS ARE VOLTS, THE Y-AXIS IS $1/(\text{FARRAD})^2$	26
FIG. 12 A GRAPHICAL DEPICTION OF THE ACTIVE VOLUME OF THE DIODE. THE DEPLETION REGION STRADDLES THE METALLURGICAL JUNCTION. THE REMAINING PARTS OF THE DIODE ARE NOT SHOWN BUT INCLUDE THE NON-DEPLETED SI AND GADOLINA AS WELL AS THE CONTACTS.	28
FIG. 13 THE GRAPHICAL OUTPUT OF A CASINO SIMULATION SHOWING (A) 79 keV ELECTRONS INCIDENT ON A SLAB OF SI WITH FULL ENERGY DEPOSITION IN 40,000NM AND (B) 180 keV ELECTRONS WITH FULL ENERGY DEPOSITION IN 160,000NM. THE OUTER CONTOUR LINE REPRESENTS 5% OF THE INCIDENT ENERGY.	29
FIG. 14 THE ACTIVE REGION WITH 3 NEUTRON INTERACTION SCENARIOS. (A) A NEUTRON PASSES THROUGH THE DEVICE WITHOUT INTERACTION. (B) A NEUTRON INTERACTS WITHIN THE DEPLETED GADOLINA REGION BUT THE INTERNAL CONVERSION ELECTRON (ICE) DOES NOT DEPOSIT ALL OF ITS ENERGY WITHIN THE DEPLETION REGION. (C) A NEUTRON INTERACTS WITHIN THE DEPLETED GADOLINA REGION	

AND THE INTERNAL CONVERSION ELECTRON (ICE) DEPOSITS ALL OF ITS ENERGY WITHIN THE DEPLETION REGION.	30
FIG. 15 A PLOT OF THE EXPECTED ELECTRICAL SIGNAL FROM THE ACTIVE VOLUME (LEFT-SIDE) AND A PRE-AMPLIFIER OUTPUT VOLTAGE (RIGHT-SIDE) AS FUNCTION OF THERMAL NEUTRON FLUX FOR THE 79 KEV ICE. THE CONVERSION OF CURRENT TO VOLTAGE USES THE FACTOR OF 0.64 μ V PER ELECTRON HOLE PAIR WHICH IS TYPICAL OF THE AMPTEK A250CF PREAMPLIFIER.	32
FIG. 16 A SCHEMATIC AND PICTORIAL DEPICTION OF A COINCIDENT DETECTOR ARRANGEMENT TO RECORD A NEUTRON CAPTURE PULSE IN COINCIDENCE WITH A GAMMA EMISSION BORN OF THE SAME REACTION.	34
FIG. 17 A SIMPLIFIED SCHEME OF USING TANDEM “NEUTRON HOWITZERS” POWERED BY PuBe SOURCES TO IRRADIATE A SAMPLE DIODE WITH THERMALIZED NEUTRONS.	36
FIG. 18 A SIMPLIFIED DIMENSIONAL DRAWING OF THE PLANNED NEUTRON HOWITZER THAT WAS TO BE CONSTRUCTED OF ALUMINUM TUBING WITHIN A 55 GALLON DRUM ABLE TO ACCOMMODATE LARGER EXPERIMENTS. THIS HOWITZER WAS NOT BUILT.....	37
FIG. 19 THE DIMENSIONS OF THE NEUTRON HOWITZER AS BUILT WITH PVC PIPE. THE CROSS-SECTION OF THE HOWITZER AS SEE FROM THE SIDE IS SHOWN IN ‘A.’ THE DETAILS OF THE FIXED CENTRAL TUBE AND MOVEABLE INNER TUBE ARE SHOWN IN ‘B.’ ‘C’ SHOWS THE DETAIL OF THE INNER TUBE AS OBSERVED WITH THE SAME ASPECT OF ‘A,’ ‘B,’ AND ‘C’. ‘D’ SHOWS THE INNER TUBE WITH THE SOURCE OPENING ROTATED 90 DEGREES TOWARD THE OBSERVER. DETAILS ‘B,’ ‘C’, AND ‘D’ ARE DRAWN TO SCALE. ‘A’ IS NOT TO SCALE AND REPRESENTS THE DIMENSIONS OF A 55 GALLON DRUM. .	38
FIG. 20 THE NEUTRON HOWITZER PVC COMPONENTS. ‘A’ THE MOVING AND FIXED TUBES WITH PIECES OF WOOD INDICATING THE THICKNESS AND LOCATION OF THE PLUGS INSIDE THE INNER TUBE. ‘B’ A DETAIL OF THE SOURCE HOLDER AS WELL AS THE BOTTOM OF THE CENTER TUBE WHICH IS A CLEAN-OUT THAT IS TO BE ANCHORED INSIDE THE DRUM.	39
FIG. 21 THE FINAL ASSEMBLY OF THE NEUTRON HOWITZER. ‘A’ CAMP STOVES WERE USED TO MELT THE PARAFFIN WAX OUTDOORS. ‘B’ THE PVC TUBES ANCHORED INTO THE DRUM AND A FEW INCHES OF WAX. ‘C’ THE WAX HAD TO BE MELTED A FEW OUNCES AT A TIME. MAINTAINING LIQUID WAX IN THE MELT WAS IMPORTANT FOR HEAT TRANSFER. ‘D’ UNEVEN COOLING OF THE WAX PRODUCED CONTRACTION POCKETS WHICH WERE FILLED WITH WAX IN SUBSEQUENT POURS.....	40
FIG. 22 THE NEUTRON SPECTRUM FROM THE PLUTONIUM-BERYLLIUM SOURCE USED FOR MCNP5 MODELING.	41
FIG. 23 THE DIFFERENTIAL NEUTRON FLUX AT THE BEAM TUBE OUTPUT OF THE PuBe SOURCE FOR THE TWO NEUTRON HOWITZER DESIGNS.....	42
FIG. 24 THE INITIAL INSTRUMENT SCHEME FOR COINCIDENT MEASUREMENT. THE UNEQUAL RESPONSE OF THE PMT’S PROMPTED EXPERIMENTING WITH SEPARATE POWER SUPPLIES BUT THIS ARRANGEMENT WAS EVENTUALLY CHANGED TO EMPLOY SEPARATE SCAS. THE LINEAR AMPLIFIER PROVIDES THE POWER FOR THE PRE-AMPLIFIER.....	44
FIG. 25 THE FINAL INSTRUMENT SCHEME FOR COINCIDENT MEASUREMENT. THE USE OF SEPARATE AMPLIFIERS AND SCAS ALLOWED EACH SCINTILLATOR CIRCUIT TO BE CALIBRATED TO SEND A GATE PULSE UPON THE DETECTION OF AN 1107.6 KEV EVENT.....	45
FIG. 26 BENCH TESTING THE COINCIDENT DETECTION SCHEME. ‘A’ THE INSTRUMENTATION SETUP ON THE BENCH. ‘B’ A DETAIL OF THE LaBr(Ce) SCINTILLATOR AND INTEGRATED PMT’S.	46
FIG. 27 A SCHEMATIC OF THE LABORATORY DEPICTING THE RESULTS OF THE GAMMA RADIATION SURVEY BEFORE AND AFTER LOADING THE HOWITZER. ‘A’ INDICATES BACKGROUND GAMMA LEVELS PRIOR TO LOADING THE HOWITZER, ‘B’ INDICATES THE LEVELS AFTER LOADING WITH THE SOURCE IN THE BEAM POSITION. LOCATION 8 IS A LEAD BOX HOUSING A SMALL Co-60 TEST SOURCE.	47

FIG. 28	A SCHEMATIC OF THE LABORATORY DEPICTING THE RESULTS OF THE NEUTRON RADIATION SURVEY BEFORE AND AFTER LOADING THE HOWITZER. ‘A’ INDICATES LEVELS PRIOR TO LOADING THE HOWITZER, ‘B’ INDICATES THE LEVELS AFTER LOADING WITH THE SOURCE IN THE BEAM POSITION....	47
FIG. 29	THE SCA CONFIGURATION CALIBRATION SCHEME. THE PULSER SIGNAL COULD BE USED WITHOUT AMPLIFICATION, BUT THE AMPLIFIED PULSER SIGNAL EMULATES THE SHAPING EFFECTS FOUND IN THE DETECTOR SIGNAL FOR A MORE ACCURATE CALIBRATION.	48
FIG. 30	A LEAD SHIELD WAS CONSTRUCTED NEXT TO THE NEUTRON HOWITZER AS SHOWN IN ‘A’. ‘B’ IS A VIEW OF THE LEAD PILE FROM BEHIND THE HOWITZER. VISIBLE ARE TWO PIECES OF PVC PIPE THAT CONTAIN THE LABr DETECTORS OPPOSING EACH OTHER. LEAD WOULD NORMALLY COVER THE TOP OF THE CHANNEL BUT IT WAS REMOVED FOR THE PHOTO. THE BEAM TUBE IS CENTERED ON THE CHANNEL CONTAINING THE BLOCK OF WOOD WHICH WAS USED AS A STAND TO RAISE THE Co-60 SOURCE CLOSER TO THE DETECTORS. ALSO VISIBLE IN ‘B’ IS THE Co-60 SOURCE AND A BOTTLE OF GADOLINIUM OXIDE.	51
FIG. 31	THE PULSE-HEIGHT SPECTRUM TAKEN WITH THE LABr DETECTORS AT THE DIODE LOCATION IN THE LEAD SHIELDING NEXT TO THE NEUTRON HOWITZER. THE COUNTING INTERVAL WAS 3600s (1 HR) OF LIVE TIME.....	52
FIG. 32	A (PuBe + Co60) GAMMA SPECTRUM OVERLAID ONTO A PuBe ONLY GAMMA SPECTRUM BACKGROUND. THE 1173.237 AND 1332.501 KEV PEAKS OF Co60 ARE READILY IDENTIFIABLE AT CHANNELS 777 AND 886. THE COUNTING TIMES OF THE TWO SPECTRA ARE NOT THE SAME AND PEAK AMPLITUDES CANNOT BE COMPARED ON THIS FIGURE.	53
FIG. 33	THREE DIODE SAMPLES WERE PREPARED FOR EXPERIMENTATION. DIODE 3, SHOWN IN ‘C’ HAD THE BEST CHARACTERISTICS AND WAS USED FOR ALL EXPERIMENTATION.	55
FIG. 34	THE DIODES WERE PLACED AS CLOSE TO THE LABr CRYSTALS AS POSSIBLE TO MAXIMIZE THE GEOMETRIC EFFICIENCY. ‘B’ IS A CLOSE-UP OF THE DIODE SAMPLE MOUNT SHOWING THE GOLD WIRES LEADING FROM THE DIODE CONTACTS.	55
FIG. 35	A SIMPLE BAND STRUCTURE MODEL OF THE Gd2O3/Si HETEROJUNCTION. THE ELECTRIC FIELD CREATED BY THE APPLIED BIAS IS LIMITED TO A REGION APPROXIMATELY 0.7 μ M IN LENGTH.	57
FIG. 36	THE INSTRUMENT DIAGRAM FOR THE CURRENT MODE MEASUREMENT SCHEME.	60
FIG. 37	THE CURRENT MODE EXPERIMENT REQUIRED A SPLITTER BOX IN ORDER TO CONTINUE THE USE OF COAXIAL CABLES AND BNC CONNECTORS.	61
FIG. 38	THE AVERAGE CURRENT MEASURED IN THE DIODE WITH AND WITHOUT THE PuBe SOURCE PRESENT. THE AVERAGE CURRENT WAS HIGHER WHEN THE SOURCE WAS PRESENT.	62
FIG. 39	THE IDEALIZED PULSE HEIGHT SPECTRUM FROM A BF ₃ DETECTOR SHOWING THE RELATIVE LOCATION OF THE WALL EFFECT.	64
FIG. 40	THE BF ₃ DETECTOR INSTRUMENTATION SCHEME.	65
FIG. 41	THE POSITIONING OF THE BF ₃ DETECTOR FOR A NEUTRON FLUX MEASUREMENT OF THE NEUTRON HOWITZER. A MEASUREMENT WAS TAKEN AT THE REAR OF THE HOWITZER FOR A COMPARISON TO THE BEAM TUBE SIDE AS DEPICTED IN ‘A’. THE MEASUREMENT AT THE DIODE LOCATION REQUIRED THE REMOVAL OF THE LABr DETECTORS SO THE BF ₃ TUBE COULD OCCUPY THEIR LOCATION IN THE LEAD SHIELDING SHOWN IN ‘B’. THE Cd COVER OVER THE BF ₃ TUBE COULD BE SEPARATED TO A PRECISE DISTANCE IN ORDER TO MAKE MEASUREMENTS OF THE COVERED AND BARE DETECTOR. ‘C’ SHOWS A CLOSE-UP OF THE DETECTOR WITH THE Cd SHIELD SEPARATED. THE SQUARE APERTURE IN THE FAR GROUND HAS LINE-OF-SIGHT TO THE BEAM PORT.....	66
FIG. 42	AN EXPERIMENTAL PULSE HEIGHT SPECTRUM TAKEN WITH THE BF ₃ DETECTOR. SHOWN ARE THREE SETS OF DATA FROM A 1 HOUR COUNT I) A 1” SEPARATION OF THE Cd COVER II) A COMPLETELY COVERED DETECTOR, AND III) THE DIFFERENCE BETWEEN I AND II. THE SUM OF THE COUNTS UNDER	

THE NET COUNTS LINE REPRESENTS THE NUMBER OF NEUTRONS THAT WERE ABSORBED BY THE CD SHIELDING.	67
FIG. 43 THE AFIT STANDARD GRAPHITE PILE. ‘A’ SHOWS A DIAGRAM OF THE PILE FROM THE ORIGINAL CALIBRATION DOCUMENT [27]. THE REMOVABLE GRAPHITE STRINGERS, OR DRAWERS, THAT WERE USED FOR DETECTOR CALIBRATION ARE LABELED HERE AS D2, D3, AND D4. ‘B’ SHOWS THE PILE WITH DRAWER 3 WITHDRAWN TO ALLOW THE PLACEMENT OF THE BF_3 DETECTOR INTO THE PILE FROM THE OPPOSITE SIDE. ‘C’ IS A VIEW LOOKING INTO THE PILE WITH THE PRE-AMP VISIBLE IN THE FORGROUND.	70
FIG. 44 A PLOT OF I/I_0 VS. NEUTRON ENERGY IN THE THIN BEAM MODEL FOR THE 0.33CM THICK CD SHIELD COMPARED TO THE TRANSMITTANCE FOR 1/3 AND 1/10 OF THE THICKNESS.....	72
FIG. 45 THE DIODE EXPERIMENT WAS CONDUCTED IN THE GRAPHITE PILE SHOWN AS ‘A’. CD AND Pb COVERS WERE PLACED AROUND THE DIODE TO SHIELD IT FROM THE FLUX IN THE PILE. A Cd SHIELD IS SHOWN COVERING THE DIODE IN ‘B’. NOT VISIBLE IS THE Cd PLATE BENEATH THE DIODE (BUT ON TOP OF THE BOARD) TO COMPLETELY SURROUND IT.	73
FIG. 46 PULSE HEIGHT SPECTRA TAKEN WITH THE DIODE IN THE PILE EXPOSED AND COVERED WITH Cd OR Pb SHIELDING. THE PEAK INCREASES WITH THE ADDITION OF A Cd SHIELD COMPARED TO THE UNSHIELDED DIODE.	74
FIG. 47 PULSE HEIGHT SPECTRA FROM THE DIODE IN THE PILE COUPLED TO THE AMPTEK PREAMP. THE SPECTRA ARE OF HIGHER RESOLUTION THAN WITH THE ORTEC PREAMP AND SHOW TWO ENERGY PEAKS.	75
FIG. 48 THE GEOMETRY OF THE MCNP5 MODEL OF THE DIODE IN THE PILE (LEFT) AND THE RESULTING NEUTRON DIFFERENTIAL FLUX AT THE DIODE (RIGHT). THE MODEL RESULTS SHOW THAT Cd ABSORBS THE LOW ENERGY NEUTRONS AS EXPECTED AND THE THERMAL NEUTRON POPULATION IS GREATLY REDUCED COMPARED TO THE UNSHIELDED POPULATION.....	76
FIG. 49 THE TOTAL NEUTRON CROSS-SECTION FOR NATURALLY ABUNDANT Gd. THE CROSS-SECTION IS GREATER THAN 1% OF 46000 B, THE THERMAL ENERGY CROSS SECTION, FOR ALL ENERGIES GREATER THAN 0.13 eV.	77
FIG. 50 A DIMENSIONAL DRAWING OF THE DIODE AS MODELED IN MCNP5.....	78
FIG. 51 A COMPARISON IF INITIAL AND FINAL PHOTON INTENSITY IN THE NARROW BEAM MODEL FOR DIFFERENT THICKNESSES OF Si IN VARIOUS REGIOS OF THE DIODE. THE INITIAL PHOTON INTENSITY IS I_0 , THE FINAL INTENSITY IS I. THE THICKER THE Si, THE LOWER THE VALUE OF I/I_0 WHICH IMPLIES INSENSITIVITY AT THAT ENERGY. THE THICKNESSES USED ARE 550×10^{-4} , 6.18×10^{-3} , AND 1.59×10^{-4} CM CORRESPONDING TO THE WAFER THICKNESS, DEPLETION PLUS DIFFUSION LENGTH, AND THE DEPLETION LENGTH. THE SPIKE IN I/I_0 IS DUE TO A K SHELL ENERGY LEVEL AT 1.83 keV.....	79
FIG. 52 THE INSTRUMENT DIAGRAM USED FOR THE GAMMA SPECTRUM MEASUREMENT.	80
FIG. 53 THE LABr SCINTILLATOR WAS MOUNTED TO A BOARD WHICH WAS PLACED INTO THE PILE. THIS ALLOWED THE DETECTOR TO BE REPLACED IN THE SAME LOCATION EACH TIME IT WAS REMOVED. THE DETECTOR WAS PLACED INTO THE PILE WITHOUT ANY COVERING ‘A’ AND WITH BOTH LEAD AND CADMIUM SHIELDS BOTH OF WHICH ARE SHOWN IN ‘B’.....	80
FIG. 54 PULSE HEIGHT SPECTRA DATA TAKEN WITH A LABr DETECTOR INSIDE THE GRAPHITE PILE AT THE DIODE LOCATION. THE PRESENCE OF SHIELDING MATERIAL SOFTENS THE SPECTRA.....	81
FIG. 55 THE PHS FROM THE DIODE (LEFT) AND THE PHS FROM THE LABr DETECTOR (RIGHT). THE ARROWS SHOW THE RELATIONSHIP BETWEEN THE DIODE RESPONSE AND THE GAMMA RAY ENERGY THAT PRODUCED IT.	82
FIG. 56 THE DIODE RESPONSE EXPLAINED BY THE ENERGY DEPOSITION BY GAMMA RAY PHOTONS.	84

FIG. 57	THE PHOTON ENERGY SPECTRUM OF THE PuBe SOURCE USED FOR MCNP SIMULATION. THE SPECTRUM WAS DEVELOPED FROM PUBLISHED DATA TAKEN WITH A HIGH-PURITY GERMANIUM DETECTOR [26].	85
FIG. 58	THE DEPOSITION OF ENERGY IN THE DIODE FROM A PuBe PHOTON SPECTRUM AS DEPOSITED IN SI OVER AN ELECTRON DIFFUSION LENGTH FROM THE METALLURGICAL JUNCTION. THE MODEL DOES NOT AGREE WITH THE HYPOTHESIS THAT MORE ENERGY IS DEPOSITED IN THE DEVICE WHEN A Cd COVER INCREASES THE LOW-ENERGY PHOTON POPULATION.	86
FIG. 59	THE DECAY SCHEMES FOR Sr-90 AND Y-90.	88
FIG. 60	THE OVERLAPPING BETA-PARTICLE ENERGY DISTRIBUTIONS OF Sr-90 AND Y-90.	89
FIG. 61	THE Sr-90 SOURCE WAS ORIGINALLY PRODUCED AS A MEDICAL APPLICATOR SHOWN IN ‘A’. THE SOURCE, PICTURED IN ‘B’ HAS A PLASTIC SHIELD THAT SLIDES UP AND DOWN THE SHAFT WHICH IS DESIGNED TO SHIELD THE OPERATOR FROM RADIATION. THE SOURCE IS SITTING HEAD-DOWN AND IS COVERED BY A THICK ALUMINUM SHIELD FOR STORAGE WHICH IS REMOVED FOR USE. THE Sr-90 IS ENCLOSED IN A STAINLESS STEEL AND ALUMINUM ELEMENT ON THE END OF THE APPLICATOR ROD.	90
FIG. 62	THE ENERGY DISTRIBUTION OF THE BETA PARTICLES EMITTED FROM THE SOURCE.	92
FIG. 63	A DIAGRAM OF THE Sr-90 EXPERIMENT. PICTURED INSIDE ALUMINUM SHIELDING ‘4’, ARE THE DIODE AND SIGNAL WIRES ‘2’, THE SOURCE ‘1’, THE CONCRETE FLOOR ‘3’, AND THE SOURCE AND SAMPLE STAND ‘5’.	93
FIG. 64	THE PULSE HEIGHT SPECTRUM TAKEN WITH THE DIODE EXPOSED TO A BETA SOURCE. THE DIODE RESPONSE WAS HIGHER CLOSER TO THE SOURCE.	94
FIG. 65	THE DECAY OF Cs-137 TO Ba-137.	95
FIG. 66	THE Cs-137 SOURCE BELONGED TO AFFRAD AND IS USED FOR CALIBRATING INSTRUMENTATION. THE SOURCE IS STORED INSIDE A CONTAINMENT VESSEL LOCATED AT THE END OF A MOVABLE STAND SHOWN IN ‘A’. THE DIODE WAS PLACED 1.608” AWAY FROM THE EXPOSED SOURCE. THIS DISTANCE WAS ACHIEVED BY PLACING THE DIODE INSIDE THE LINE-OF-SIGHT PORT OF THE PIG AS SHOWN IN ‘B’ AND ‘C’. CLOSE PLACEMENT MAXIMIZED THE GAMMA FLUX.	97
FIG. 67	THE PULSE HEIGHT SPECTRUM TAKEN FROM THE DIODE DURING IRRADIATION FROM THE 1.2 Ci Cs-137 SOURCE.	98

List of Tables

TABLE I THE HALF-LIVES, PRIMARY DECAY MODES, AND SPONTANEOUS NEUTRON EMISSION RATE OF SELECTED SPECIAL NUCLEAR MATERIAL	4
TABLE II THE MAJOR GAMMA EMISSIONS OF PU-239 AND U-235	5
TABLE III PROMPT ENERGY DISTRIBUTION OF FISSION FOR U-235 AND PU-239. UNITS ARE MeV.....	6
TABLE IV THE COMPOSITION OF NATURALLY OCCURRING GADOLINIUM	12
TABLE V DEPOSITION CONDITIONS FOR THE SAMPLES PREPARED AT THE UNIVERSITY OF NEBRASKA.....	22
TABLE VI PARAMETERS USED TO CALCULATE THE EXPECTED ELECTRICAL SIGNAL.....	32
TABLE VII A SUMMARY OF THE COINCIDENT GAMMA DETECTION CALIBRATION	49
TABLE VIII THE PARAMETERS USED TO CALCULATE THE THERMAL NEUTRON FLUX USING THE BF ₃ DETECTOR.....	68
TABLE IX THE CALCULATED THERMAL NEUTRON FLUX FROM THE NEUTRON HOWITZER.....	69
TABLE X A SUMMARY OF THE CALCULATED AND CALIBRATED THERMAL NEUTRON FLUX IN THE AFIT STANDARD GRAPHITE PILE BY DRAWER POSITION.	71
TABLE XI THE COMPUTED ABSORBANCE FRACTION OF GAMMA RAYS IN SILICON.	83
TABLE XII THE PARAMETERS OF AFIT SOURCE NUMBER 00365, THE SR-90 EYE APPLICATOR.	88
TABLE XIII THE LINEAR STOPPING POWER OF THE SR-90 SOURCE HOUSING.....	91

List of Abbreviations

<u>Abbreviation</u>	<u>Description</u>
α	Alpha Particle
n	Neutron
DoD	Department of Defense
DTRA	Defense Threat Reduction Agency
SNM	Special Nuclear Material
eV	Electron Volt
MCNP	Monte Carlo Neutral Particle
Ci	Curie
PuBe	Plutonium-Beryllium
β -	Beta Particle, an electron
HV	High Voltage
LV	Low Voltage
PMT	Photomultiplier Tube
DLA	Delay Line Amplifier
TSCA	Timing Single-Channel Analyzer
LLD	Lower Level Discriminator
MCB	Multi-Channel Buffer
Cd	Cadmium
Pb	Lead
LaBr	Lanthanum Bromide
TSCA	Timing Single Channel Analyzer
UPS	Uninterruptible Power Supply

PHS	Pulse-Height Spectrum
Gd ₂ O ₃	Gadolinium Oxide, Gadolina
Cs	Cesium
Sr	Strontium
Co	Cobalt
Y	Yttrium
Ce	Cerium
Hf	Hafnium
PPSN	Probability per source neutron
MATLAB	Matrix Laboratory
UNL	University of Nebraska at Lincoln
PLD	Pulse Laser Deposition
SCWCR	Super Critical Water Chemical Reactor
ICe	Internal Conversion electron
AFRRAD	Air Force Radiological Recycling and Disposal
SCS	Semiconductor Characterization System
NIST	National Institute of Standards

GADOLINIUM OXIDE / SILICON THIN FILM HETEROJUNCTION SOLID-STATE NEUTRON DETECTOR

I. INTRODUCTION

During the Cold War (1945-1991), the national resources of the world's superpowers were allocated to the enrichment and production of fissile materials and the means to deliver them in a weaponized form. The detection of radioactivity was paramount to protecting both the technicians and scientists creating these stockpiles and the sizeable armed forces ready to operate in the environment following a nuclear exchange. Thus, the detection of radioactive material has been a key component to radiation protection. Until 1991, the stockpiles of special nuclear material were tightly controlled and protected. With the dissolution of the former Union of Soviet Socialist Republics, the control of special nuclear material (SNM) has been less certain. Special nuclear material as defined by Title I of the Atomic Energy Act of 1954 includes plutonium, uranium-233, and uranium enriched in the isotopes uranium-233 or uranium-235 [1]. Since 1991, several nations are in possession of SNM. Unfortunately, some do not have stable governments and at least two of them, namely Iran and Pakistan, have national borders adjacent to active combat zones. The September 11, 2001 attacks on the US have shown that extremist organizations have the desire and means to inflict harm on the US and her allies and are limited only in their ability to obtain the weapons to do so. The post-Cold War era finds the detection of SNM a vital interest of national security.

Primitive portal monitors have been installed along sensitive transportation nodes in the US and work continues on building robust systems to expand detection capability

[2]. The US Defense Threat Reduction Agency (DTRA) is tasked “with a vital national security mission: to safeguard America and its allies from Weapons of Mass Destruction (chemical, biological, radiological, nuclear, and high explosives) by providing capabilities to reduce, eliminate, and counter the threat, and mitigate its effects [3].” As one of its priorities, DTRA actively pursues new technology initiatives to detect SNM [4]. There are several existing methods to detect SNM but recent developments in materials have made solid-state detectors attractive because of their potential portability and low-cost.

1.1 Theory of Special Nuclear Material Detection

Plutonium-239 and uranium-235 are the well-known fissile materials used to construct nuclear weapons. Uranium is mined from natural deposits that are nominally 0.7% U-235 and enriched to over 80% U-235 for use in a weapon [5]. Pu-239 is formed from U in a reactor. This process inevitably produces a material enriched in Pu-239 but Pu-240 and, to some degree, Pu-241 will be present. Table I lists some SNM decay modes, half-lives, and spontaneous fission neutron emission rates. Unfortunately, for the purpose of detection, SNM is relatively stable (it decays with long half-lives) and therefore does not betray its presence through decay product emission with great frequency.

When a sample of SNM is observed with a detector in the traditional sense, it is termed ‘passive’ detection and the detector measures the naturally occurring emissions from the sample. It follows that a drawback to passive detection is the long counting

time required to successfully observe the infrequent decay events of SNM. Active detection techniques are being developed to reduce the observation time. The term ‘active’ describes the use of photons or neutrons to cause excitation or even fission in SNM. This technique has the advantage of producing a more active signature over a shorter period of observation. Unfortunately, this technique also has application limitations due to personnel exposure and the difficulties inherent in the fielding of an activation source. Regardless of the technique, detecting SNM centers chiefly on detecting its characteristic radio-emissions. Like most nuclear reactions, nuclear decay produces a product nucleus that is generally in an excited state. The decay of SNM is primarily by alpha emission with subsequent de-excitation gamma emission. The alpha particles are generally not useful for detection because they are stopped by the material itself or the device housing. U-235 emits a variety of low energy gamma-rays in conjunction with alpha emission. The most prevalent U-235 gamma-rays are 143.76 keV (relative intensity 11%) and 163.33 keV (relative intensity 5%) as listed in Table II. The best photon signature for detecting U-235 is not from U-235 itself, but an emission of a decay product of U-238. Since weapons-grade uranium always has U-238 present, its decay to Protactinium-234m provides an opportunity to measure a characteristic, high energy, 1001 keV gamma ray as Pa-234m transitions to Pa-234.

TABLE I The half-lives, primary decay modes, and spontaneous neutron emission rate of selected special nuclear material.

	Half-Life [year]	Primary Decay Mode	Spontaneous Fission Neutron Emission Rate [n / 100 g s]*
²³⁹ Pu	24110	α Emission	2
²⁴⁰ Pu	6564	α Emission	138359
²⁴¹ Pu	14.4	α Emission	23
²³⁵ U	7.04E+08	α Emission	0.14
²³⁸ U	4.50E+09	α Emission	1.5

* Emission rate based upon an average of 2.89 neutrons per Plutonium fission and 2.44 neutrons per Uranium fission.

As it has already been inferred, there is a problem with using photon detection to identify SNM. Since most of the decay energy is carried-off by the alpha particle, the photons are low energy and there are many of them. Table II outlines the characteristic gamma-lines and their relative intensities for Pu-239 and U-235. It can be difficult to distinguish the relatively low energy signatures from the background continuum of gamma and x-rays from naturally occurring cosmic and terrestrial radiation sources. However, at least one controlled experiment has been successful at detecting fissile material in a naval cruise-missile warhead [6]. The purposeful masking of SNM gamma signatures by collocating high-activity sources can make successful identification difficult.

TABLE II The major gamma emissions of Pu-239 and U-235

²³⁹ Pu Decay		²³⁵ U Decay	
Gamma ray [keV]	Relative Intensity	Gamma ray [keV]	Relative Intensity
38.66	10500	109.16	1.54
46.21	737	140.76	0.22
51.62	27100	143.76	10.96
56.83	1130	163.33	5.08
98.78	1220	182.61	0.34
116.26	597	185.72	57.2
129.93	6310	194.94	0.63
203.55	569	202.11	1.08
345.01	556	205.31	5.01
375.05	1554	221.38	0.12
413.71	1466	279.50	0.27

Neutron detection provides a less ambiguous means of detecting SNM which, by its very nature and intended use, begs to be detected by its neutron emissions.

Spontaneous fission, a quantum tunneling phenomenon, is a natural decay mode for SNM making passive detection possible. Fission can also be induced by incident neutrons either cosmic in nature or from an active source. The fission reactions are summarized in (1) and (2) [7].



The energy distribution of (1) and (2) are well-known and are summarized in Table III [7]. The neutrons born of these reactions have a spectrum of energies which are determined, in part, by the number emitted which in turn is a function of the fissile

material and the incident neutron energy. Using an average neutron emission of 2.89 neutrons per fission of Pu and 2.44 from U, the energies of the emitted neutrons are found to be on the order of 2 MeV for both materials with a most-probable energy of 1 MeV [7].

TABLE III Prompt Energy Distribution of Fission for U-235 and Pu-239. Units are MeV.

	²³⁵ U	²³⁹ Pu
Fission Fragment Kinetic Energy	168	172
Neutron Kinetic Energy	5	6
Prompt Gamma Energy	7	7
Total Prompt Energy	180	185

An advantage of using neutrons to detect SNM is their relatively low natural background. In general, only the transuranic elements are sources of naturally occurring terrestrial neutrons [8]. However, SNM, especially plutonium with any appreciable amount of plutonium-240, spontaneously emits neutrons at a rate above the background. Table I, previously presented, lists the spontaneous fission neutron emission rates per 100g of material for several important nuclides. The calculation of these values is included in Appendix B. Since the neutron emissions have a relatively narrow energy distribution, their presence is a good indicator of SNM that cannot be masked.

One of the difficulties in detecting neutrons is that they are neutral particles. The difficulty in constructing a neutron detector lies in the ability to create an interaction with neutrons that is detectable. The most useful signals of detection are electric or photonic pulses. Recent advances in the field of semi-conducting dielectric materials, such as

gadolinium oxide, make it possible to produce semi-conductor devices that have a high probability of neutron interaction.

1.2 Problem Statement

Can a heterojunction diode made from a thin film of gadolinium oxide (Gd_2O_3) deposited on p-type silicon detect neutrons via conversion electron conversion?

1.3 Document Organization

This document is written to emphasize four areas. The first is an appreciation for the advantages of gadolinium-based neutron detector materials. The second area develops a method of depositing Gd on silicon with subsequent device fabrication. The third is a feasibility study that outlines the potential of using the device to detect neutrons using the $^{157}\text{Gd}(n,\gamma)^{158}\text{Gd}$ reaction. And finally, a set of experiments and their findings are presented addressing the feasibility of using the device to detect neutrons.

II. BACKGROUND

2.1 Properties of Detector Materials

Neutrons are not detected directly, but rather identified by observing the product of a nuclear reaction. The probability that a nucleus will interact with a neutron is termed its neutron cross-section. Because “interaction” has a variety of meanings, specific cross-sections have been determined for absorption and elastic / in-elastic scattering. Fig. 1 illustrates the total neutron cross-section for several nuclides of interest used for neutron detection. The cross-section trends illustrated in Fig. 1 show that, in general, lower energy neutrons have a higher probability of interacting with a target nucleus. It is customary to refer to neutrons by their kinetic temperature. When the kinetic temperature of a neutron is 0.025 eV or below, it is said to be “thermal.” This follows from (3) where k is Boltzmann’s constant (8.62×10^{-5} eV/K), T is the absolute temperature, and \bar{E} is the average neutron energy of a Maxwell-Boltzmann energy distribution.

$$\bar{E} = \frac{3}{2}kT \tag{3}$$

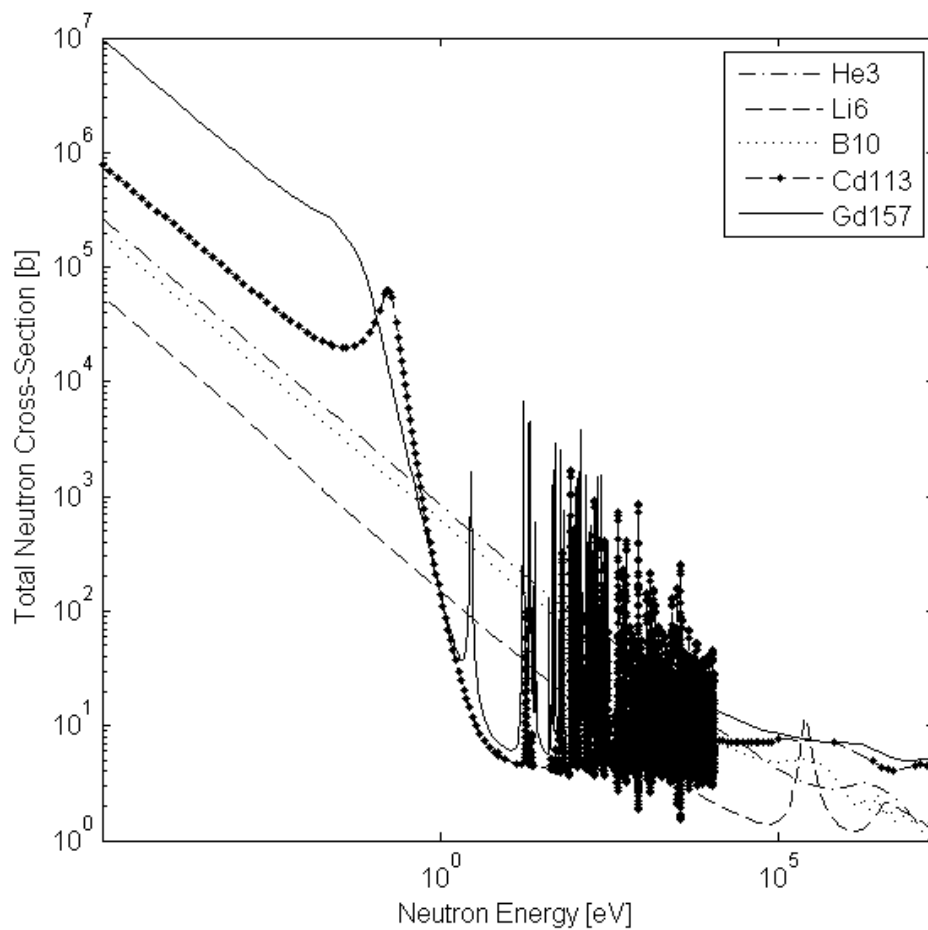
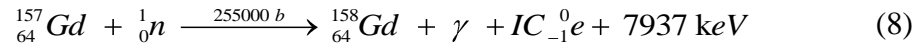
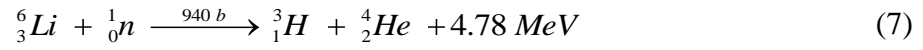
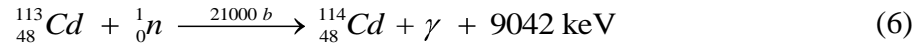
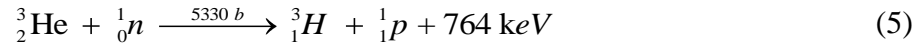
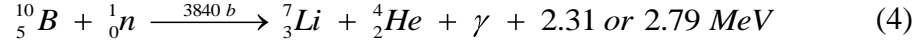


Fig. 1 The total neutron cross-section of several nuclides used in neutron detectors.

At ~300K, or room temperature, the average energy is ~0.025 eV. Neutrons faster than thermal up to ~1 MeV are considered “epi-thermal” and beyond that they are “fast.” Fig. 1 shows a peak for Cd-113 at 0.17 eV. The trailing edge of this out to 0.4 eV has a relatively large cross-section which is referred to as the “Cadmium cut-off” and can be used as a benchmark for describing neutron energies.

Each of the nuclides in Fig. 1 have been exploited for their interaction with neutrons as a detector medium. The reactions are summarized in (4) through (8) and include the thermal neutron cross section for absorption in units of barns = [b] = 10^{-24} [cm²].



Boron, which exists naturally as 19.7% B-10, is used extensively for neutron detection and the resulting alpha particle is an efficient agent for ionization in a detector [9].

Helium-3 produces tritium and a proton which can be detected in a proportional gas detector which is the common application for this isotope. Cadmium-114 produced from neutron capture in Cd-113 de-excites through a readily observable gamma emission to its stable state [11][12]. Cadmium is commonly used as a shielding material in order to harden a spectrum by absorbing thermal neutrons. The Li-6 reaction produces an alpha particle and a triton, or tritium particle. This reaction is often employed in conjunction with iodine in the form of LiI scintillators sensitive to thermal neutrons [9].

Gadolinium-157 has the highest total neutron cross-section of all known nuclides.

Fig. 2 shows the highest 3 cross-sections for the isotopes of Gadolinium.

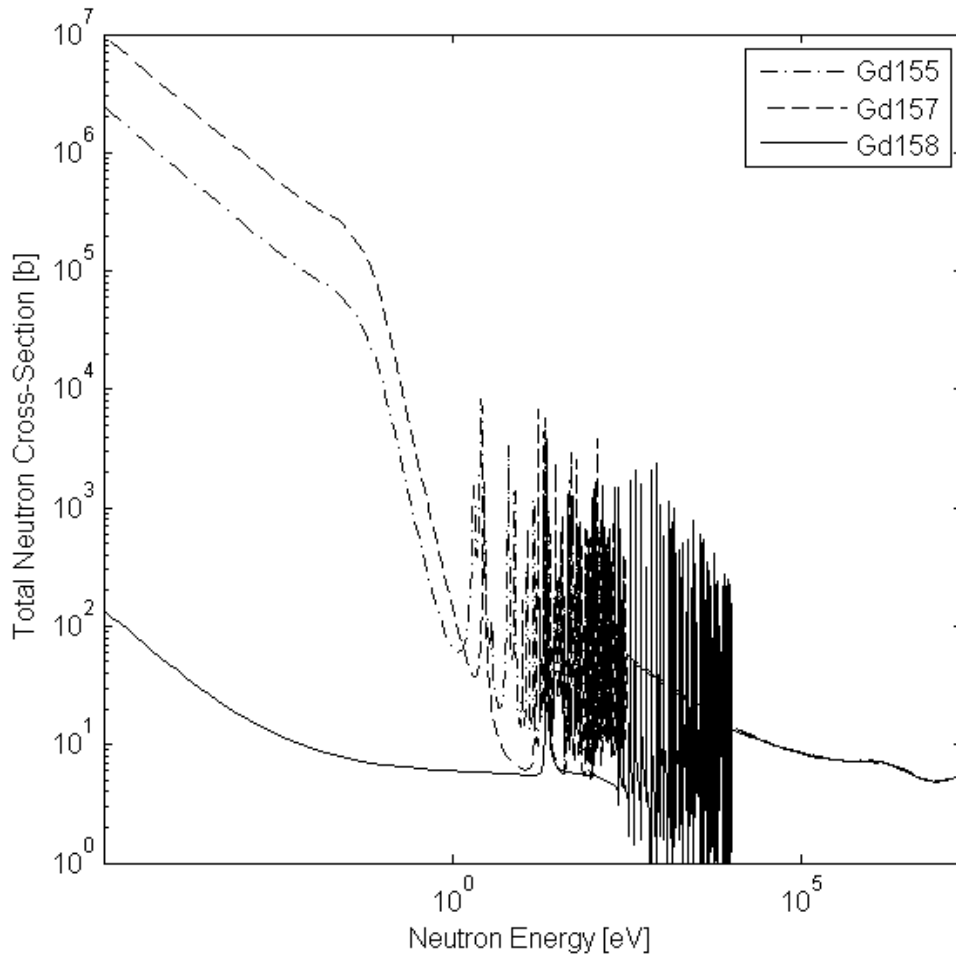


Fig. 2 Total neutron cross-sections of selected Gadolinium isotopes. Of the five stable isotopes, mass numbers 157, 155, and 158 have the highest cross-sections.

Naturally occurring Gd has 5 stable isotopes of which mass numbers 155 and 157 represent 14.8% and 15.65% of the natural abundance. Table IV summarizes the isotopic composition of natural Gd.

TABLE IV The composition of naturally occurring Gadolinium

	Natural Abundance [weight %]	Half-Life [years]
¹⁵² Gd	0.20%	1.08E+14
¹⁵⁴ Gd	2.18%	Stable
¹⁵⁵ Gd	14.80%	Stable
¹⁵⁶ Gd	20.47%	Stable
¹⁵⁷ Gd	15.65%	Stable
¹⁵⁸ Gd	24.84%	Stable
¹⁶⁰ Gd	21.86%	1.30E+21

Accounting for its isotopic composition, natural Gadolinium has a thermal neutron capture cross section of 46,000 b [10].

Unlike (4) and (7), the $^{157}\text{Gd}(n,\gamma)^{158}\text{Gd}$ reaction produces low energy conversion electrons instead of heavily ionizing alpha particles making the reaction less attractive for a detector. However, semiconductor manufacturing has reached the point at which Gd_2O_3 is readily available for making semiconducting devices.

2.2 Detector Technologies

There are several detector technologies which fall into the broad categories of scintillators, proportional counters, solid-state conversion layer detectors, and neutron absorbing solid-state detectors. Scintillators use the luminescent response of the detector to ionizing radiation as the indicator of neutron interaction. Unlike gamma scintillators in which ionization directly follows the gamma energy absorption, neutron scintillator materials are ionized by recoiling ions following neutron collisions. Scintillator light must be collected and amplified, requiring photomultiplier tubes which are powered by a high-voltage power source and are inherently inefficient [8]. Proportional counter neutron detectors often use He-3 as a stopping gas which relies on (5) for the $^3\text{He}(n,p)^3\text{H}$ reaction. Proportional counters also require a high-voltage power supply and are not very portable. The need for high-voltage and, in many cases, a high-pressure tube to increase gas density makes them less rugged for remote applications.

Solid-state conversion layer detectors utilize a layer of neutron-reactive material that acts both as a moderator and a source of particles to cause ionization in the active volume of the detector. The probability of neutron interaction increases with conversion layer thickness, but the ionization track of the daughter particle within the sensitive region decreases. Neutron absorbing solid-state detectors overcome this by incorporating high neutron absorption cross section material as a part of the diode junction. Boron-carbide and gadolinium-doped hafnium oxide diodes have been fabricated for this purpose and have achieved some success [13][14]. A diode made from gadolinium oxide should have similar success to the gadolinium doped hafnium oxide device

considering the same principle reaction applies for signal generation but will contain a higher number density of gadolinium nuclei.

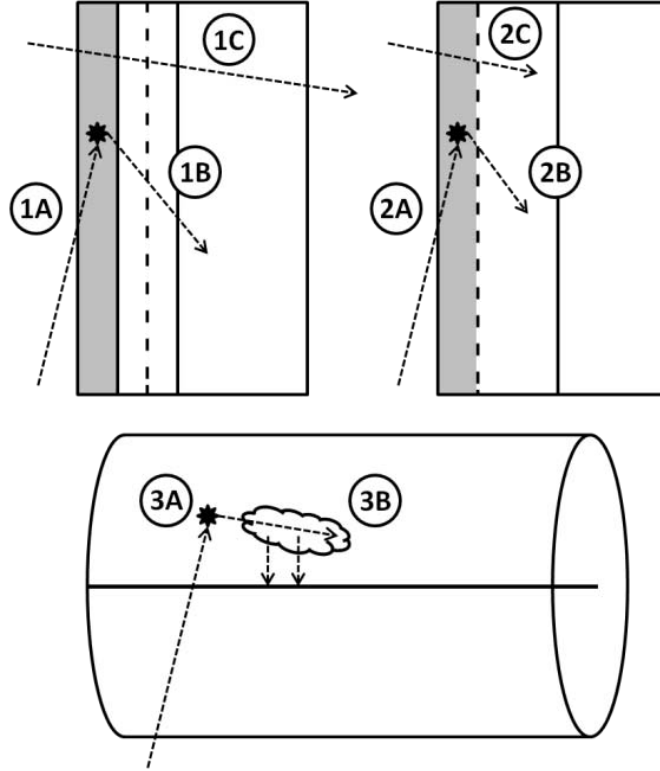


Fig. 3 A conversion layer diode (Top Left), an intrinsic diode (Top Right), and a gas counter (Bottom). In the conversion layer diode, an incident neutron samples the moderating layer and either passes through it without interaction (1C) or slows until a reaction occurs (1A). A nuclear reaction product creates ionization within the active region of the diode (1B) but may not deposit all of its energy before ionizing an inactive region. An intrinsic diode depletes the neutron-reactive layer. A neutron can either pass without interaction (2C) or react to form an ionizing particle (2A) which is already within the active region (2B). A gas detector operates on the principle that the ionizing particle born of the neutron interaction (3A) deposits its energy by ionizing gas molecules (3B) while the charge cloud is pulled into a collecting wire under a high bias.

2.3 Gadolinium

The $^{157}\text{Gd}(n,\gamma)^{158}\text{Gd}$ reaction is more complex than presented earlier as (8). The Gd-158 nucleus is often produced in an excited state and de-excites through various means. This process is understood for 19.1% of the Gd-158* de-excitations and is summarized in Fig. 4. There are two distinct excited energy states achieved by the

nucleus upon simultaneous emission of a pair of gamma rays referenced as γ_1 and γ_2 in Fig. 4. Lines A and B list the 5 most intense coincident gamma-rays emitted prior to an emission of a 261, 182, or 79 keV photon or internal conversion electron [16][17].

Internal conversion (IC) occurs when the excited nucleus transfers energy to an atomic electron, usually in the K or L shell, with subsequent emission of the electron from the atom. This process competes with gamma emission. Observation of an atom's preference for each process is expressed as the internal conversion coefficient, α , given by (9). The number of internal conversion emissions and photon emissions of the same energy are given by λ_e and λ_γ . In general, α is higher for large atoms and scales as Z^3 [15]. The coefficient also varies inversely with both the transition energy and scales with principle quantum number as $1/n^3$ [15]. In other words, large transitions are preferentially gamma emission, and K-shell electrons are more likely than L-shell as IC candidates [15].

$$\alpha = \frac{\lambda_e}{\lambda_\gamma} \quad (9)$$

It is expected that the internal conversion coefficient for the 79 keV emission will be as high as 30% due to the low energy emission and Gd's large nucleus [14]. Assuming a Gd-158 nucleus de-excites along path B, the probability that a single de-excitation results in a 79 keV IC electron is 3.4%. The loss of the IC electron triggers a cascade of electron wave function changes to "re-shuffle" the orbitals and fill the core vacancy. This cascade emits a series of low energy X-rays on the order of 7 keV (L-Shell) to 43 keV (K-Shell) for Gd [17]. A process competing with the X-ray emission is Coster-Kronig (CK)

emission whereby an electron is emitted similar to IC. The energy of a CK electron from the L-shell of GD is 1 keV [17].

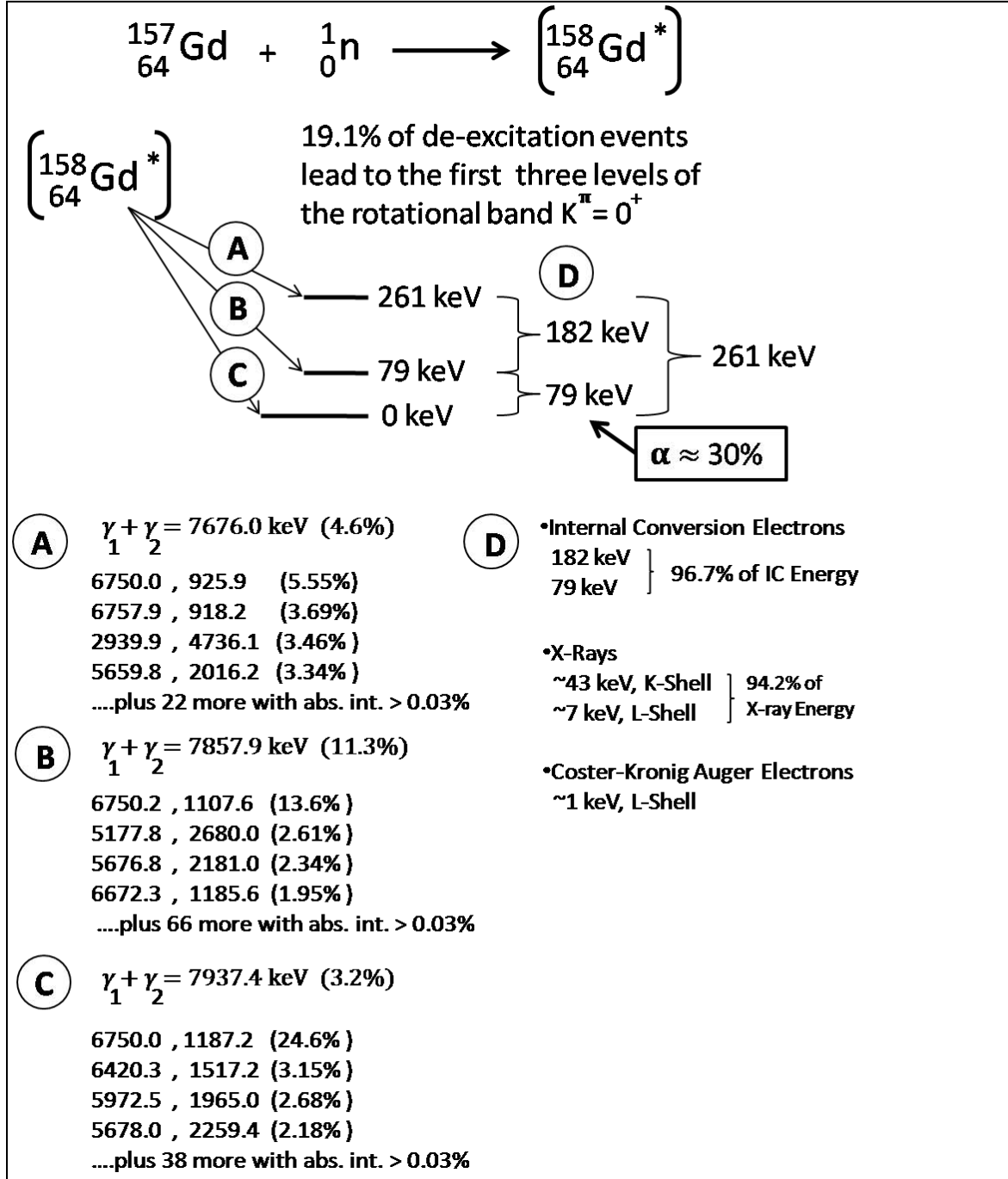


Fig. 4 The summarized de-excitation scheme of the excited ^{158}Gd nucleus of the $^{157}\text{Gd}(\text{n},\gamma)^{158}\text{Gd}$ reaction [16][17].

III. EXPERIMENTAL APPROACH

3.1 Introduction

The experimental approach covers four areas. First, the application of a thin film of Gd_2O_3 on p-type silicon using a supercritical water system is described. Next, the fabrication of a diode from the deposition sample is explained. Third, the feasibility of the device as a neutron detector is discussed. Lastly, the design of an experiment to determine if the diode can successfully detect neutrons is presented.

3.2 Supercritical Gadolinium Oxide Deposition

Gadolinium oxide (Gd_2O_3 , or gadolina) has been explored commercially as a high-k dielectric to replace SiO_2 in traditional metal-oxide-semiconductors. The use of a high-k material provides a gate that is thicker than SiO_2 but electrically equivalent, thus reducing leakage currents [19]. As a result, the process of fabricating a semiconductor from gadolina and silicon has been recently developed by the semiconductor industry [19]. The advances have been in the interest of miniaturization, not neutron detection.

Diodes made from Gd_2O_3 deposited on p-type silicon have been successfully fabricated at the University of Nebraska, Lincoln (UNL) by both pulsed laser deposition (PLD) and supercritical water deposition. The use of pulsed laser deposition to deposit gadolina on Si yielded a monoclinic Gd_2O_3 crystal structure. The use of supercritical water deposition yielded a cubic Gd_2O_3 structure. Fig. 5 illustrates the arrangement of the atoms in the two crystal structures.

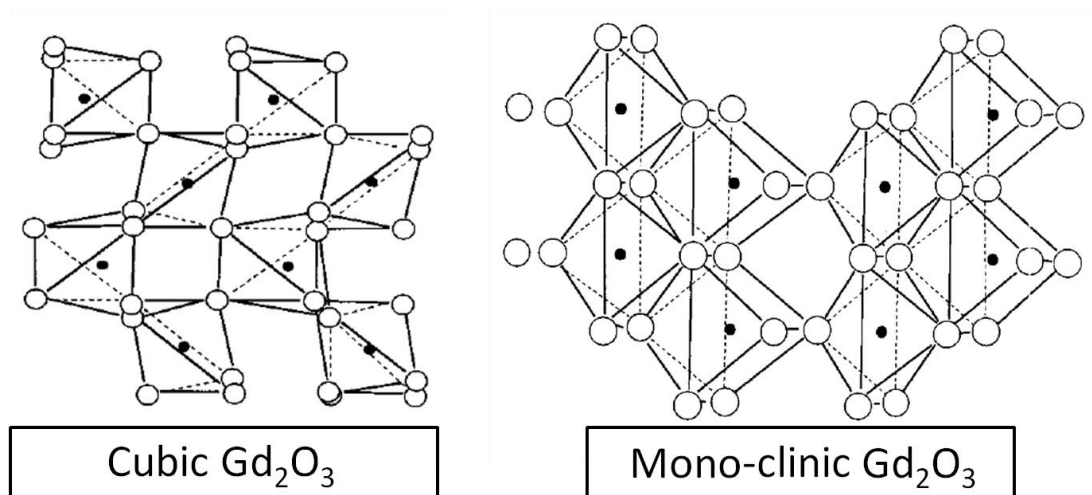


Fig. 5 The structure of cubic and mono-clinic Gadolinium Oxide. The dots represent Gd atoms [21].

Both techniques produced diodes that successfully rectified but fabricating contacts was difficult on the monoclinic structure. Contacts were more easily fabricated on cubic gadolima and recent work suggests that the cubic structure on p-type silicon (100) is also the better semi-conductor [20].

The super-critical water chemical reactor (SCWR) is schematically depicted in Fig. 6. The process uses water to solvate Gd_2O_3 and supersonically deposit it on p-type silicon. In this context, “supercritical” means that the solvent is above the critical point. Fig. 7 illustrates the location of the supercritical regime of a typical phase diagram. The supercritical point for water is 647 K and 218 atm. Gadolina is not soluble in water ordinarily, but is soluble in supercritical water.

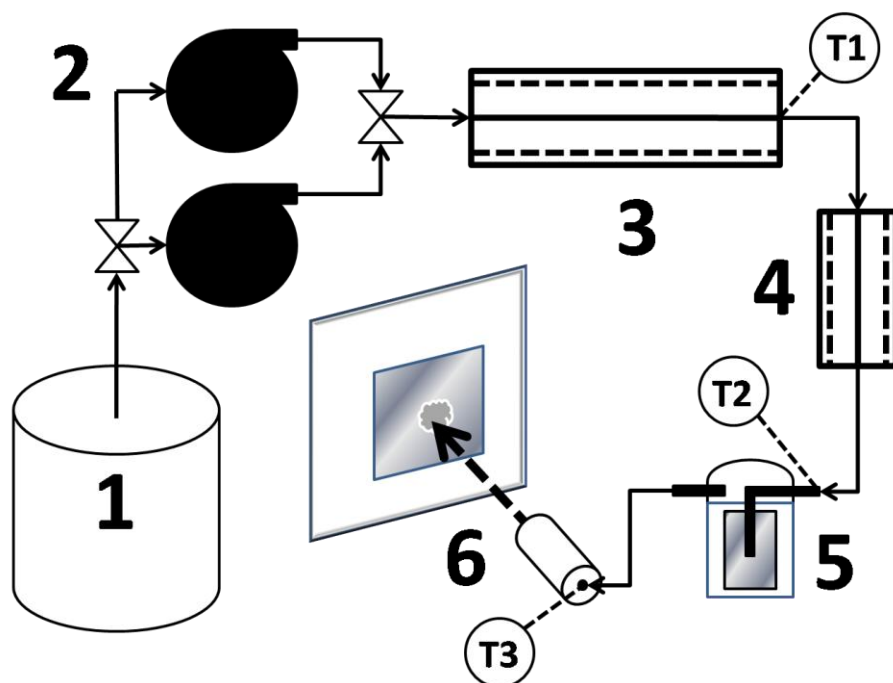


Fig. 6 A schematic representation of the super-critical water chemical reactor (SCWR) successfully used at the University of Nebraska, Lincoln to deposit cubic Gd_2O_3 on p-type silicon. (1) Purified Water Tank. (2) High Pressure Pumps. (3) First Stage Solvent Heater. (4) Second Stage Solvent Heater. (5) Filter Basket containing Gd_2O_3 . (6) Expansion Nozzle and p-type silicon target. T1, T2, and T3 are temperature probes.

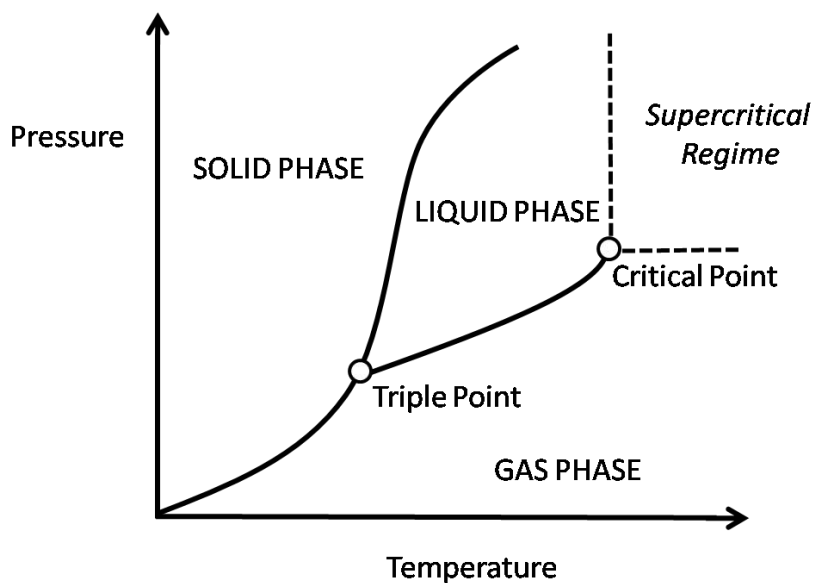


Fig. 7 A typical phase diagram of matter showing the location of the Critical Point, above which the material acts as a supercritical fluid.

The deposition process requires solvent and target substrate preparation. Ultra-filtration of de-ionized water is performed until the nominal resistivity is approximately 17 M Ω cm. Nitrogen gas is bubbled through the water to displace dissolved gases. The silicon substrate sample is washed for 10 minutes in both acetone and ethanol using an ultrasonic bath to remove organic surface contaminants. A 5% hydrofluoric (HF) acid etch is then used to remove a surface layer followed by a water rinse prepared as stated.

The system uses two parallel syringe pumps, each with a 266 mL capacity, to provide high pressure water. Only one pump is used at a time for semi-continuous operation. The primary heating coil is used to bring the water temperature into the super critical region. The secondary heating coil is located next to the 0.5 micron sintered stainless steel filter basket in which 0.9 g of Gd₂O₃ is loaded. The system is optimized to create stagnation conditions within the filter basket. At the stagnation point, all of the kinetic energy of the fluid is converted to pressure. The fluid saturates with Gd₂O₃ and is expanded supersonically through a 50 micron orifice across a 1 to 2 cm air gap onto the substrate.

Although the operating conditions of the reactor are varied as part of ongoing research, there are some nominal operating conditions. The primary coil is operated at 600 °C, the secondary at 460 °C. In order to achieve stagnation conditions, the nozzle temperature must be the product of 0.88 and the absolute temperature of the fluid in the filter basket. This equation is summarized in (10) and is the result of thermodynamic modeling by Dr. Jennifer Brand of the UNL Chemical Engineering Department who is currently researching supercritical deposition methods.

$$\text{Nozzle Temperature}[^{\circ}\text{C}] = 0.88 \times 460^{\circ}\text{C} + 273.15 \quad (10)$$

The silicon substrate is fixed to the sample holder. The sample holder is monitored for temperature but no effort is made to apply heat or electrical bias. The average deposition time is 1 hour with water flow rates nominally 7mL/min. The Gd_2O_3 is deposited as a film on the substrate with rods and crystallites visible on the surface of the film under an optical microscope inspection illustrated in Fig. 8.

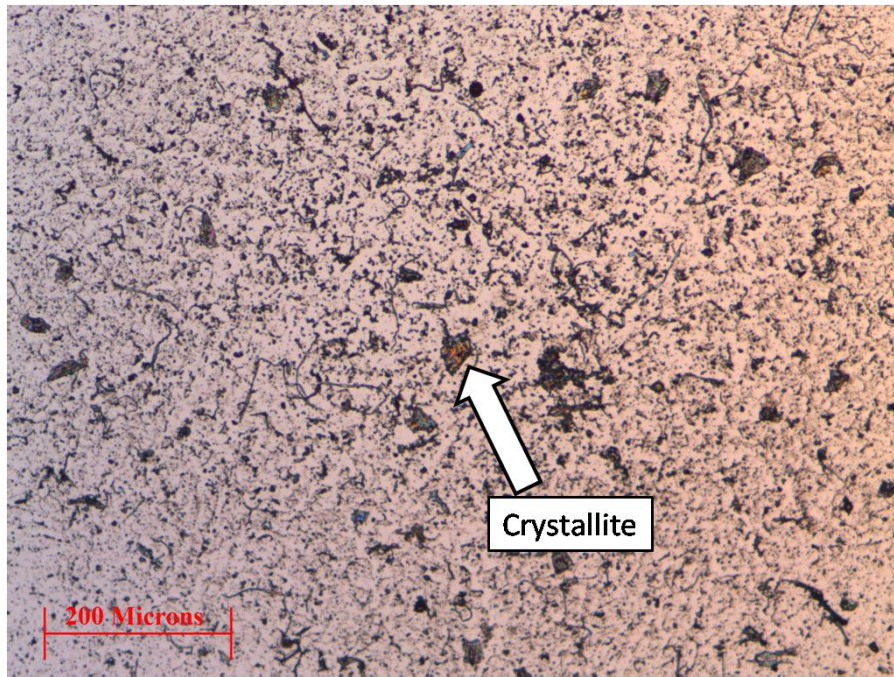


Fig. 8 An optical microscope view of the Gd_2O_3 film showing the formation of crystallites.

Using a profilometer, it was determined that a 1 hour deposition yielded a 1000 \AA film. The film thickness peaks near the focal point of deposition and tapers at the edges. Table V is a compendium of deposition parameters for the samples produced at UNL.

TABLE V Deposition conditions for the samples prepared at the University of Nebraska

Abr. Sample #	University of Nebraska Sample #	Super-Critical Water Deposition Conditions					
		Stagnation Temp [°C]	Press. [bar]	Nozzle Temp [°C]	Substrate Temp [°C]	Nozzle-Substrate Spacing [cm]	Deposition Time [min]
11	061509-MP-Gd ₂ O ₃ -pSi-11	455	240	*	*	2	60
12	061209-MP-Gd ₂ O ₃ -pSi-12	450	240	340	48	2	60
21	061009-MP-Gd ₂ O ₃ -pSi-21	500	240	344	54	1	60
31	061009-MP-Gd ₂ O ₃ -pSi-31	470	240	355	60	1	60
JS	XXXXXX-XX-Gd ₂ O ₃ -pSi- JS	*	*	*	*	*	*
* Indicates the parameter is unknown							

3.3 Diode Fabrication

After deposition, contacts were sputtered onto the sample in order to create a working device. The samples of Gd₂O₃ on silicon were prepared using a contact mask which has a 5-hole by 5-hole grid in a 1 cm square on the deposited side. Copper tape was used to build-up layers to provide indirect contact and mask the surface to shield from over-sputter. The samples were attached to a carousel using tape and glass microscope slides to protect the sample from the carousel's rough surface. The loaded carousel is placed upside down onto a spindle affixed to the sputter chamber lid and a moveable shield is placed on the spindle such that it protects the samples from the targets. Gold and aluminum targets were placed into the magnetron "gun" positions inside the

chamber and a collimator was placed over them. The lid was set in place and the chamber was pumped-down in 2 stages to a vacuum condition of approximately 10^{-7} torr. The evacuation of the chamber required 12 hours to reach high vacuum. Power was applied to the targets and argon gas was introduced. A plasma was ignited over the targets which caused material to be spalled-off of the face of the target by impact of heavy argon ions. It is the ejected material that deposits onto the sample face. The time required for deposition is a function of both the desired deposition thickness and the calibrated sputtering rate of the apparatus. The calibrated sputtering rate was a linear fit of 2 points utilizing X-ray Diffraction techniques (XRD) to determine the film thickness for each target at a prescribed power applied to the magnetron. The nominal thickness for the multilayer contact was 150 angstroms of Al followed by 500 angstroms of Au. This contact recipe was developed at UNL by several months of trial and error.

$$Al[\frac{Angstrom}{s}] = 0.026 \times Power[Watt] + 0.505 \quad (11)$$

$$Au[\frac{Angstrom}{s}] = 0.127 \times Power[Watt] + 2.245 \quad (12)$$

The samples were inverted and a single contact was sputtered onto the backside using the same recipe. The back contact is a common contact for the entire set of diodes. Fig. 9 shows the idealized final product and nominal dimensions of a diode fabricated in the fashion described.

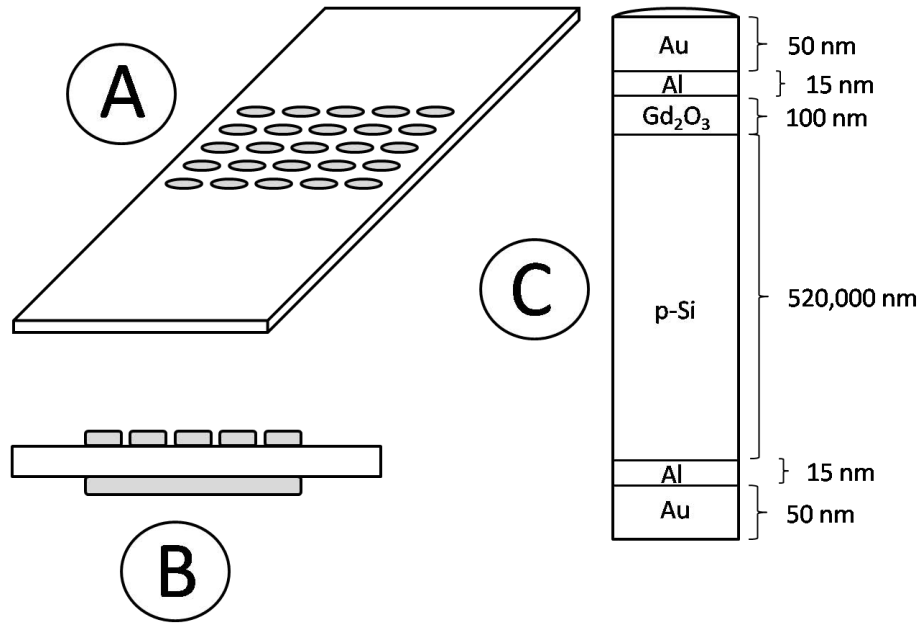


Fig. 9 A sample of Gd_2O_3 on Si with contacts. (A) A depiction of the sample with 25 contacts sputtered over the Gadolina layer. (B) An end-view of the sample depicting the contact geometry (exaggerated dimensions). (C) A dimensional depiction of the cross-section of a single diode using the base of the gold contact as a reference point.

3.4 Initial Device Characterization

Characterization of the diodes was done to verify rectification. Fig. 10 illustrates the current-voltage, or $I(V)$, response of a single diode in sample 1, prepared from 061009-MP-Gd2O3-pSi-31, at various temperatures. The reverse bias region appears relatively stable from 0 to -1 V. The diode, modeled as Fig. 9 detail C, contains regions of gadolina and silicon through which the charge carriers must move in order to reach the contacts. The conductivity of the diode appears to decrease with decreased temperature indicating that impurity scattering in the non-depleted regions is affecting conductivity. Phonon scattering is not a contributing factor since decreased temperature decreases the lattice vibration. The use of cold temperature conditions to reduce diode signal noise would be offset by signal loss.

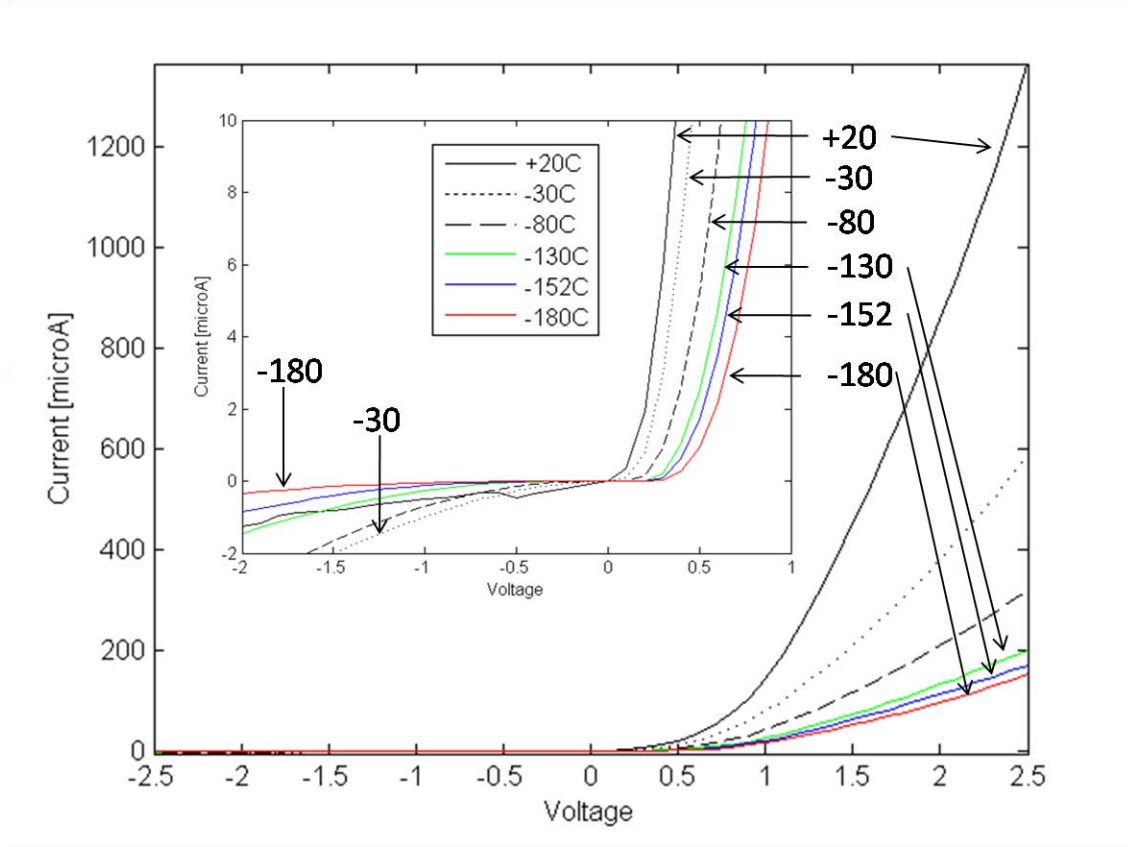


Fig. 10 The I(V) response for contact 5 of diode sample 1 showing rectification at various temperatures.

Capacitance-Voltage, C(V), measurements were conducted at room temperature in order to determine the silicon substrate doping concentration and the threshold voltage. A plot of $1/C^2$ vs. bias indicated a carrier concentration of $2 \times 10^{19} \text{ 1/cm}^3$ which is suspect for p-type silicon. Although the relatively linear plot indicates that an abrupt junction approximation might be appropriate, the deposition method does not support it. The junction will be sufficiently infused that C(V) data cannot be used to determine carrier concentration. Intrinsic p-type silicon has a nominal carrier concentration of 10^{15} 1/cm^3 which was used for calculations to determine the depletion region boundaries.

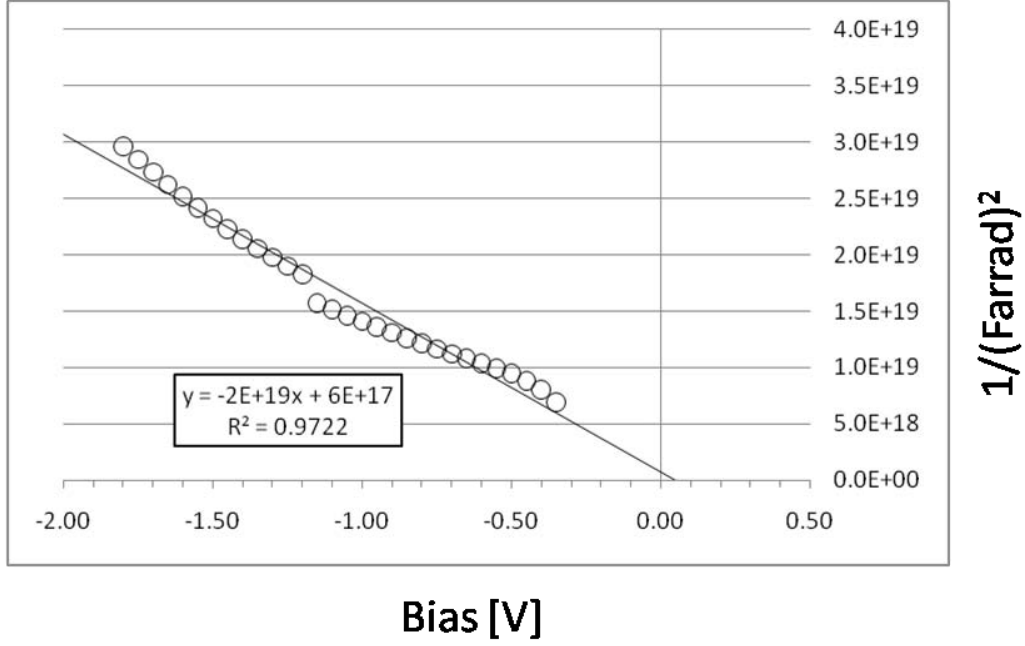


Fig. 11 The $1/C^2$ vs. bias [V] plot for contact 5 of diode sample 1 at room temperature. The X-axis units are Volts, the Y-axis is $1/(\text{Farrad})^2$.

3.5 Feasibility of Neutron Detection

The active detector volume must be large enough to capture the full energy deposition of the internal conversion electrons from the $^{157}\text{Gd}(n,\gamma)^{158}\text{Gd}$ reaction. A diode was modeled as depicted in Fig. 9 detail C with carrier concentrations of $N_A = 10^{15} \text{ [1/cm}^3\text{]}$ in the p-type Si and $N_D = 5 \times 10^{19} \text{ [1/cm}^3\text{]}$ in the Gd_2O_3 layer. An abrupt heterojunction model was assumed. The depletion width was approximated using (13), (14), and (15) assuming the depleted volume will be mostly Si. The depletion width is abbreviated as W [22]. X_p and X_n are the depletion distances from the metallurgical junction into silicon and Gd_2O_3 respectively.

$$\frac{N_A(q)Xp^2}{2(kSi)\epsilon_0} + \frac{N_D(q)Xn^2}{2(kGd_2O_3)\epsilon_0} = -(V_{BuiltIn} + V_{applied}) \quad (13)$$

$$W = Xp + Xn \quad (14)$$

$$Xp(Na)q = Xn(Nd)q \quad (15)$$

The built-in voltage was taken as 0.15V which is the average value attained from the $1/C^2$ vs. bias plots for sample 1. The dielectric constant for Si, k_{Si} , is 11.9 and 17 for Gd_2O_3 , $k_{Gd_2O_3}$. Solving (13) and (15) simultaneously for a bias of -1.5V yields a depletion width, W , of 1.592×10^{-4} cm or 1592 nm. Assuming cylindrical geometry, the active volume of the diode as a detector can be determined by assuming a diameter equal to the sputtered contact region. Depicted in Fig. 12, the active volume of the detector is the region straddling the metallurgical junction in which the full energy deposition of an IC electron will result in a detected pulse.

Electrons produced by ionization outside of the depletion region are much less likely to be collected out to a diffusion length away from the depletion region. Beyond a diffusion length, the charge can be considered lost to the diode. The diffusion length of an electron, L_n , in Si was computed to be 16 μ m. Computing the active diode volume using only the depletion width provides conservative results as the active volume is somewhat larger.

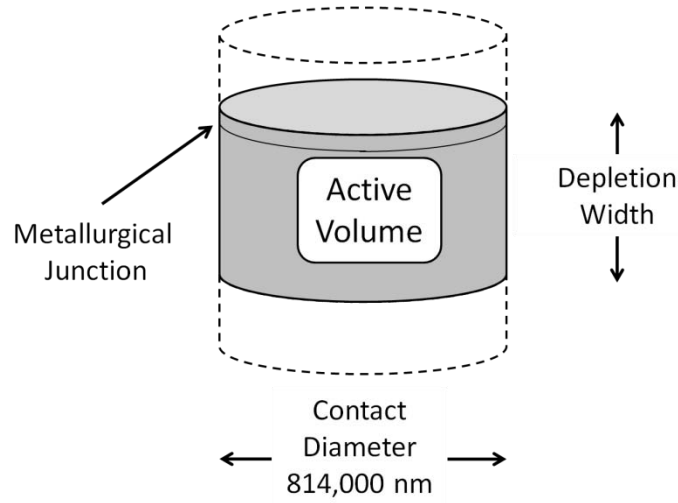


Fig. 12 A graphical depiction of the active volume of the diode. The depletion region straddles the metallurgical junction. The remaining parts of the diode are not shown but include the non-depleted Si and gadolima as well as the contacts.

The diameter of a contact was measured to be 814×10^3 nm using a scaled enlargement of the sputtered region. The resulting volume was calculated to be $4.14 \times 10^{-6} \text{ cm}^3$ using (16) and is mostly silicon.

$$ActiveVolume = \frac{X_p (\pi)(Contact\ Diameter)^2}{4} \quad (16)$$

The calculation of (13), (14), (15), and (16) using Mathematica[®] is included in Appendix A [34].

A CASINO simulation was conducted to determine if the dimensions of the active region were large enough to detect an IC electron [31]. The simulation output is graphically shown in Fig. 13. The code simulates a monoenergetic electron beam of specified energy traveling into a material which is silicon for this simulation. The color-coded regions represent energy deposition in terms of initial energy. The outermost contour is light blue and represents 5% of the initial energy, or 95% energy deposition.

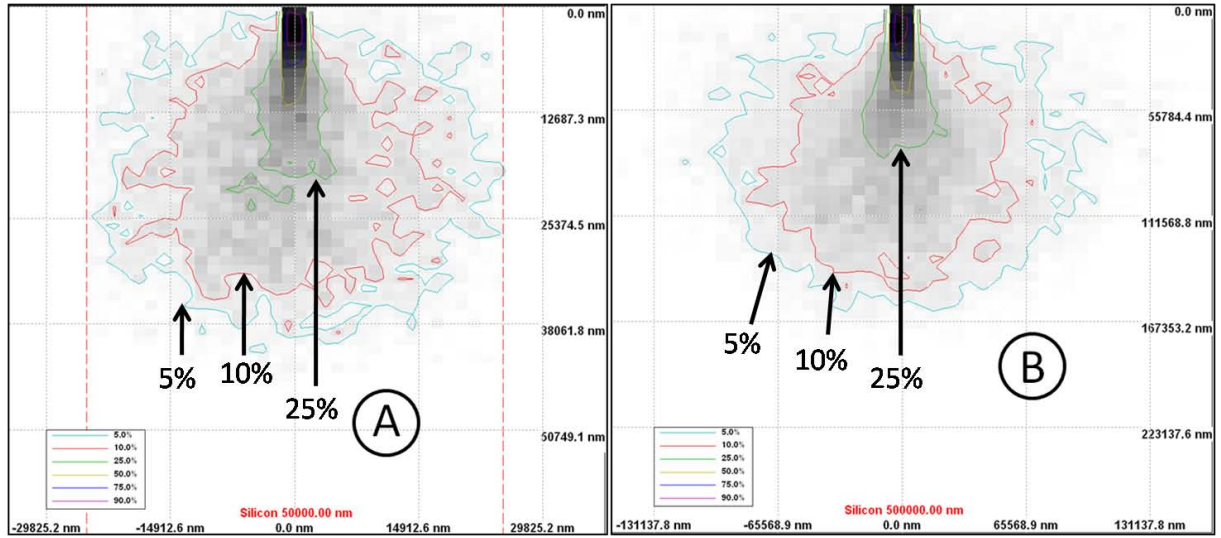


Fig. 13 The graphical output of a Casino simulation showing (A) 79 keV electrons incident on a slab of Si with full energy deposition in 40,000nm and (B) 180 keV electrons with full energy deposition in 160,000nm. The outer contour line represents 5% of the incident energy.

With an active volume diameter of 814,000 nm, a 79 and 180 keV IC electron (ICe) will both have the potential to be detected as a pulse. The 79 keV electrons in the CASINO simulation deposited all of their energy in under 40,000 nm. The 180 keV electrons deposited their total energy in 168,000 nm. Since the depletion width is only 1592 nm, electrons with a trajectory parallel to the metallurgical junction will be able to deposit their full energy as depicted in Fig. 14 detail C.

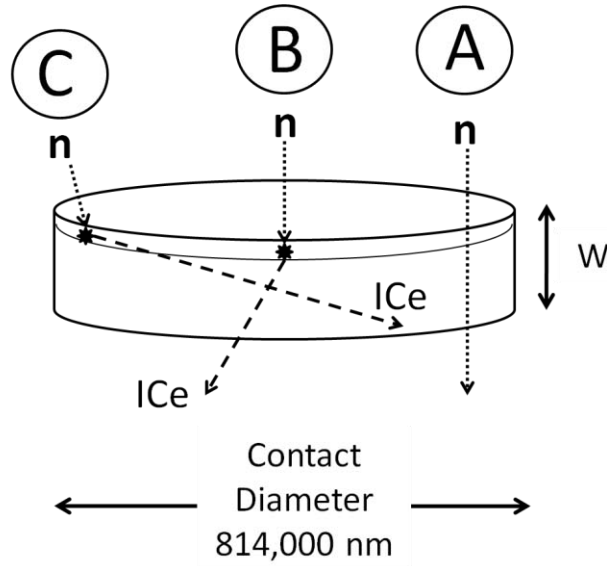


Fig. 14 The active region with 3 neutron interaction scenarios. (A) A neutron passes through the device without interaction. (B) A neutron interacts within the depleted Gadolina region but the Internal conversion electron (ICe) does not deposit all of its energy within the depletion region. (C) A neutron interacts within the depleted gadolina region and the internal conversion electron (ICe) deposits all of its energy within the depletion region.

3.6 Diode Signal and Neutron Flux

There are several factors that determine the probability of neutron detection by the diode. Material and device properties are somewhat fixed or have narrow limits. The determination of the minimum neutron flux needed for successful detection is important for experimental design. It is assumed for the purpose of calculating the minimum flux needed to produce a detectable signal that the flux consists of only 0.025 eV neutrons and that the detector is operating in current mode. Both of these assumptions yield a conservative estimate for minimum neutron flux.

The macroscopic cross-section, Σ , for gadolina was determined using (17) where σ is the microscopic cross section for natural Gd ($46000 \times 10^{-24} \text{ cm}^2$) and N is the number of Gd

nuclei per volume given by (18) to be 2.53×10^{22} Gd nuclei/cm³. $MW_{Gd_2O_3}$ represents the molecular weight of gadolite, and $\rho_{Gd_2O_3}$, its density.

$$\Sigma = \sigma N \quad (17)$$

$$N = \frac{(\rho_{Gd_2O_3})(N_{Avogadro})}{MW_{Gd_2O_3}} \left[\frac{\text{moles Gd}}{\text{mole Gd}_2\text{O}_3} \right] \quad (18)$$

The reaction rate density (RRD) was then computed by (19) which is the product of the macroscopic cross-section and the neutron flux.

$$RRD = \Sigma \phi \quad (19)$$

The expected electrical signal (EES) is the product of the RRD, active detector volume, average crystal ionization energy, and the probabilities of producing an ICe. The EES is summarized in (20).

$$EES = RRD \text{ Vol } \lambda_{Branch} \alpha \frac{q_e \times E_{ICe}}{E_{ionization}} \quad (20)$$

The term Vol is the active detector volume, γ_{Branch} is the probability of de-excitation to a specific energy state, α is the internal conversion coefficient, q_e is the charge of an electron, E_{ICe} is the energy of the IC electron, and $E_{ionization}$ is the average energy required to create an electron/hole pair in the material. The average ionization energy for gadolite was approximated as 18 eV which is the value of SiO₂. Fig. 15 shows the EES as a function of thermal neutron flux calculated from (20) using the factors of Table VI. The result indicates that a thermal neutron flux of 1×10^6 [n/cm² s] is barely adequate to achieve a reasonable signal. However, this is a conservative estimate in that it does not consider that the charge is integrated over a pulse of a micro-second or less, producing a

stronger signal. This is termed ‘pulse mode’ operation and is common to most spectroscopic measurement systems [8]. Conservatively, the calculation shows that non-reactor neutron sources could be used which simplified experimental design.

TABLE VI Parameters used to calculate the expected electrical signal.

Factor	Constant	Units
$\rho \text{ Gd}_2\text{O}_3$	7.41	g/cm^3
$\text{MW Gd}_2\text{O}_3$	352	g/mole
Vol	4.14×10^{-4}	mm^3
$\sigma \text{ Gd}$	46000	b
α	30	%
γ_{Branch}	11.3	%
$E_{\text{ionization}}$	18	eV
E_{ICe}	79,000	eV

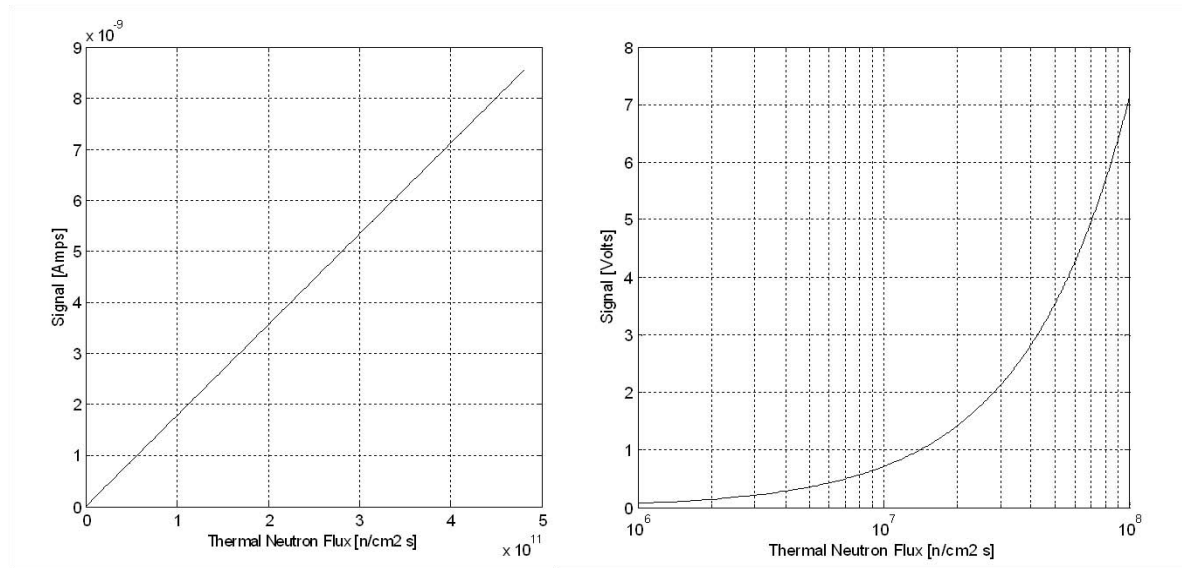


Fig. 15 A plot of the expected electrical signal from the active volume (Left-Side) and a pre-amplifier output voltage (Right-Side) as function of thermal neutron flux for the 79 keV ICe. The conversion of current to voltage uses the factor of 0.64 μV per electron hole pair which is typical of the Amptek A250CF preamplifier.

3.7 Experimental Concept

3.7.1 Goal

The goal of the experiment was to determine if a semiconducting diode made from gadolinium oxide (Gd_2O_3) and p-type silicon could detect neutrons. The theory and modeling supported that the diode could produce a detectable electrical signal based upon the $^{157}\text{Gd}(n,\gamma)^{158}\text{Gd}$ reaction. An investigation of a gadolinium-containing diode in 2008 claimed to have identified the 79 keV signal pulse [14]. This diode contained hafnium oxide enriched with gadolinium up to 15%. A diode fabricated with Gd_2O_3 should produce a larger signal corresponding to a higher reaction rate density.

3.7.2 Coincidence Measurements

In order to determine if the detected signal was from the $^{157}\text{Gd}(n,\gamma)^{158}\text{Gd}$ reaction, coincident gamma emissions were to be used in order to corroborate the claim of neutron detection. The 6750.2/1107.6 keV binary gamma ray pair is the most likely emission in coincidence with a 79 keV ICE. Large diameter sodium-iodide (NaI) detectors were readily available but did not have the resolution to discriminate between the 1107.6 keV and 1187.2 keV gamma ray emissions, the two most likely emissions. The resolution of an energy feature in a pulse-height spectrum can be represented as the full-width at half maximum (FWHM) of the energy divided by the centroid (H_0) energy. Resolution can also be represented as a proportionality constant, K, divided by the square root of energy as in (21) [8].

$$R = \frac{FWHM}{H_0} = \frac{K}{\sqrt{E}} \quad (21)$$

Using a nominal K value for NaI of 3.14 [8], the resolutions for energies of 1187 and 1107 keV are 9.1% and 9.4%. The peaks for these centroids would overlap at FWHM by 5 keV if a NaI detector were used. Cerium doped Lanthanum Bromide, LaBr(Ce), scintillators have a resolution as high as 3% at 662keV which will provide the appropriate resolution. Fig. 16 illustrates, in simplest form, the coincident measurement scheme for recording a pulse-height spectrum from the diode in coincidence with a characteristic gamma-emission.

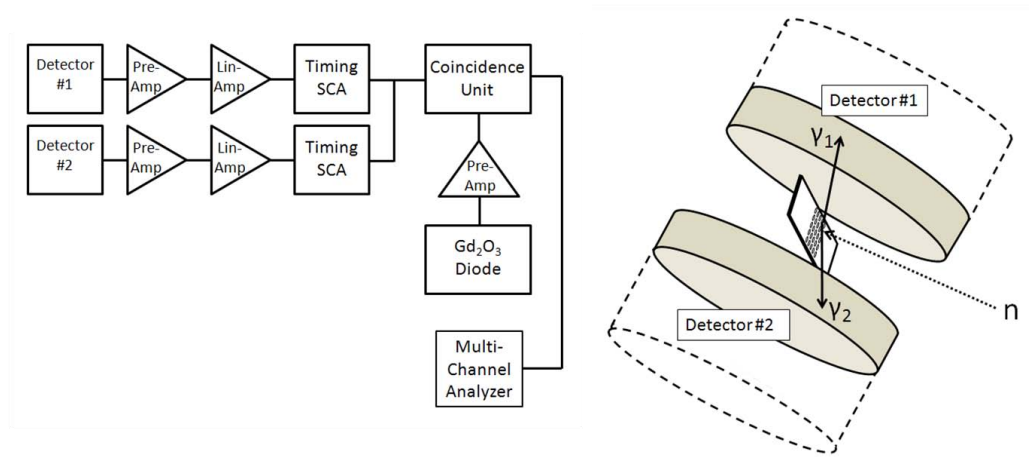
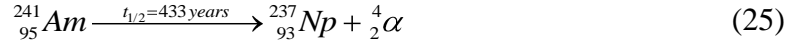
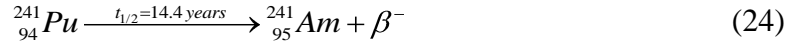
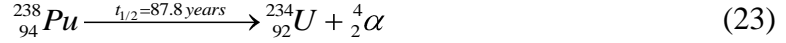
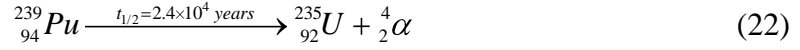


Fig. 16 A schematic and pictorial depiction of a coincident detector arrangement to record a neutron capture pulse in coincidence with a gamma emission born of the same reaction.

The technique reduces noise and couples the diode signal to neutron capture with high confidence. This arrangement is only feasible if the neutron source geometry allows for effective shielding of the scintillators from gamma rays emitted from the source.

3.7.3 Neutron Source

Two 5 Ci Plutonium-Beryllium (PuBe) sources were available as a source of neutrons. The PuBe source is a mixture of Pu and Be completely mixed together and sealed in a stainless steel casing. The decay of Pu produces an alpha particle as shown in (22) and (23) which interact with the Be to produce a neutron (26). The presence of Pu-241 which decays to Am-241 shown as (24) provides an increasing neutron emission rate for several years after the production of the source.



Calculating the neutron emission rate of a PuBe source requires the use of the Bateman equations for the decay reactions listed above. This calculation was performed by [30] and a modified calculation is included in Appendix C. The neutrons born of the ${}^9\text{Be}(\alpha, n){}^{12}\text{C}$ reaction are fast and must be moderated to produce a sizeable thermal neutron population. A neutron howitzer provides neutron moderation and allows for the construction of a coincident gamma-ray detection system. Using paraffin wax as the howitzer moderator is simple, cost effective, and efficient. Stoichiometrically, paraffin can be modeled as $\text{C}_{32}\text{H}_{68}$ and has a density of 0.93 g/cm^3 [23]. The large fraction of

hydrogen makes it an excellent moderator material. The construction of two howitzers would allow for the use of both 5 Ci PuBe sources as depicted in Fig. 17.

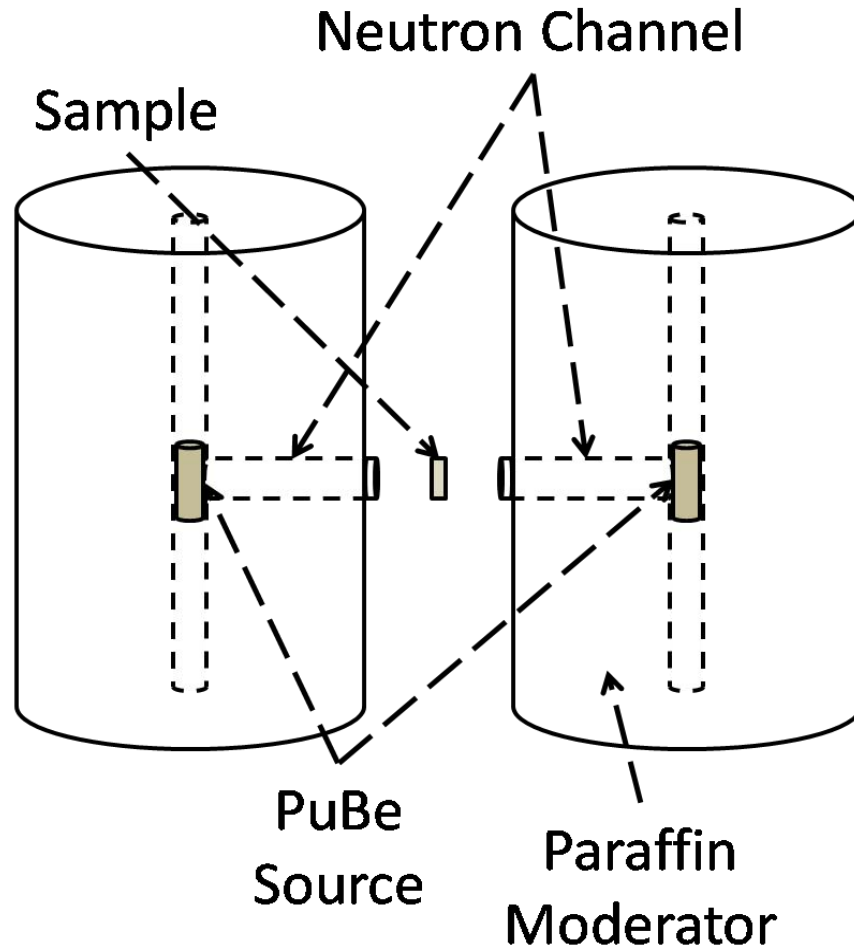


Fig. 17 A simplified scheme of using tandem “neutron howitzers” powered by PuBe sources to irradiate a sample diode with thermalized neutrons.

The actual howitzer was built using PVC pipe due to time constraints. Fig. 19 shows the dimensions of the simplified design.

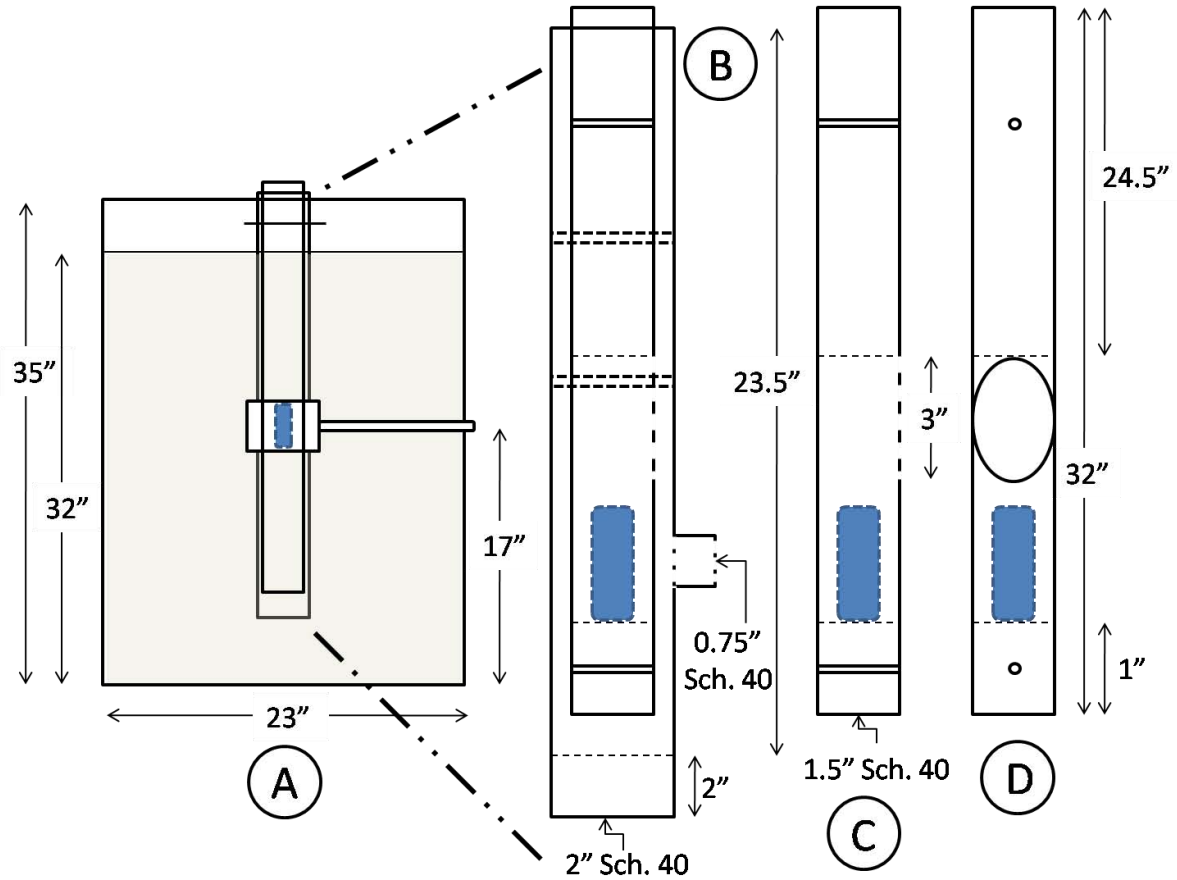


Fig. 19 The dimensions of the Neutron howitzer as built with PVC pipe. The cross-section of the howitzer as seen from the side is shown in 'A.' The details of the fixed central tube and moveable inner tube are shown in 'B.' 'C' shows the detail of the inner tube as observed with the same aspect of 'A', 'B', and 'C'. 'D' shows the inner tube with the source opening rotated 90 degrees toward the observer. Details 'B', 'C', and 'D' are drawn to scale. 'A' is not to scale and represents the dimensions of a 55 gallon drum.

The howitzer is loaded in 3 steps: 1) Raise and rotate the inner tube to the 'load' position and partially insert the positioning peg 2) Remove the PuBe source from the storage container and place it into the recess of the inner tube using a remote handling tool 3) Remove the positioning peg and allow the inner tube containing the source to

drop into the safe position under its own weight. The source can be raised to the ‘beam’ position when needed.

The construction of the howitzer was straight forward. The PVC pipe was cut to length and the source opening was cut and shaped. Wooden plugs were cut to seal the bottom of the fixed center tube as well as the top and bottom of the inner tube where the source is housed. Care was used to make sure that the top of the source access hole was flush with the bottom of the wooden plug. A lip at this location could cause the source to ‘stick’ in the tube during removal. Fig. 20 shows the working components of the howitzer during pre-assembly. A hole matching the outer diameter of the beam tube was drilled in the 55 gallon drum. The pipe and fittings were assembled inside the drum and fixed using a wooden foot anchored to the bottom of the drum.

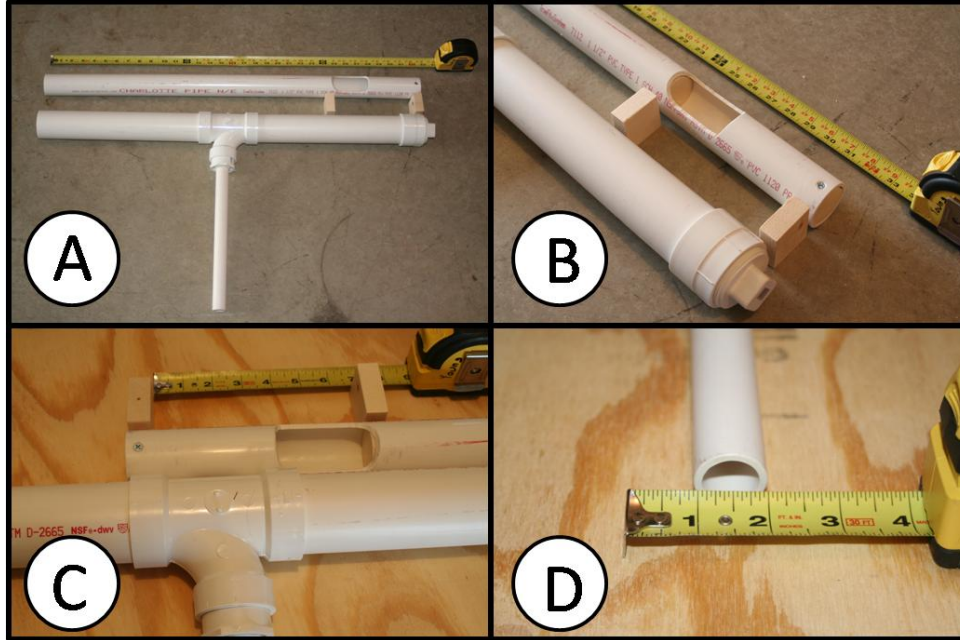


Fig. 20 The Neutron Howitzer PVC components. ‘A’ The moving and fixed tubes with pieces of wood indicating the thickness and location of the plugs inside the inner tube. ‘B’ A detail of the source holder as well as the bottom of the center tube which is a clean-out that is to be anchored inside the drum.

Fig. 21 illustrates the final assembly of the howitzer with paraffin. Small propane camp stoves were used to melt the wax which was then poured into the howitzer. Paraffin wax melts between 135 and 145° F and has a flash-point between 248 and 254° F making it a safe product to work with. The howitzer required approximately 500 pounds of paraffin to fill.

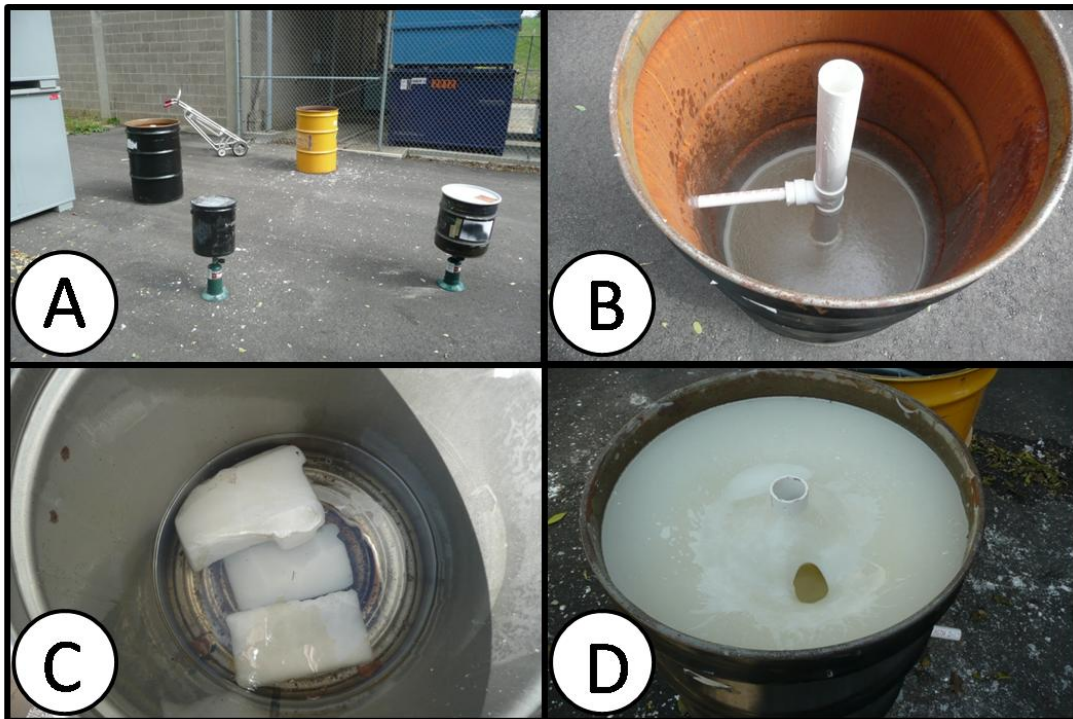


Fig. 21 The final assembly of the Neutron Howitzer. ‘A’ Camp stoves were used to melt the paraffin wax outdoors. ‘B’ The PVC tubes anchored into the drum and a few inches of wax. ‘C’ The wax had to be melted a few ounces at a time. Maintaining liquid wax in the melt was important for heat transfer. ‘D’ Uneven cooling of the wax produced contraction pockets which were filled with wax in subsequent pours.

The wax was poured over several days outdoors with ambient temperatures in the 40 to 60 °F range. The first day of work filled the drum up to ~18 inches from the bottom. A leak developed around the beam tube which was sealed by allowing a cylinder of wax to partially cool and forming it around the seam like a putty. Subsequent pours melted the previously cooled wax with each addition to the drum. On the second day of work, it was

found that the uneven cooling of the previously added wax caused a contraction void. The void was filled and subsequent pours re-melted several inches of the previously added wax. The drum cooled for 4 days before the last of the wax was solidified. A final pour was required to remove the last air pocket. The fixed center tube was filled with 2” of wax and the entire inner tube above the source was filled. Holes were drilled in the tubes for a positioning peg made from a wire rod. The howitzer was moved into the basement of building 470 using the external North stairwell.

Monte Carlo Neutral Particle transport code (MCNP5) was used to model the differential neutron flux at the beam tube output of each howitzer design [32]. The PuBe source differential flux was modeled as depicted in Fig. 22 [25].

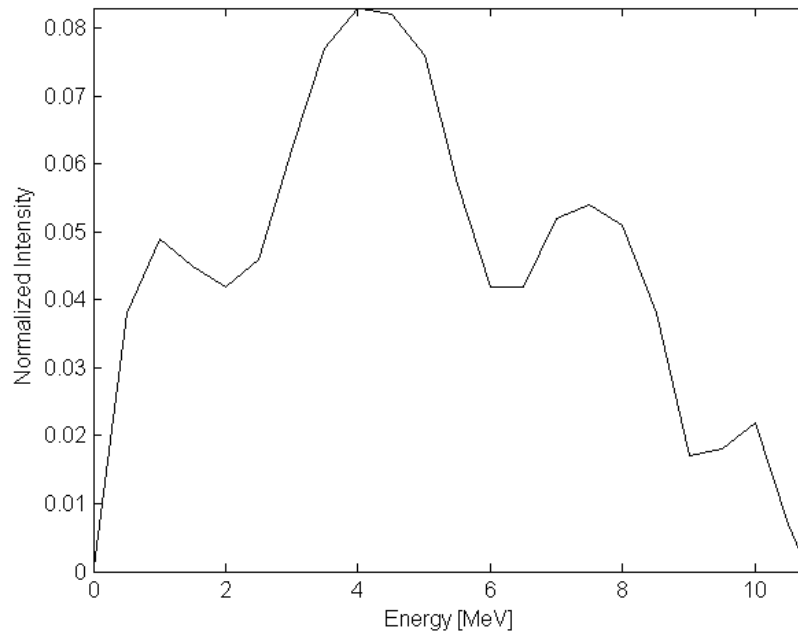


Fig. 22 The neutron spectrum from the Plutonium-Beryllium source used for MCNP5 modeling.

The moderated spectrum at the beam tube output, as modeled in MCNP, is graphically depicted in Fig. 23 for the neutron population below 1 eV. The input code for this simulation is found in Appendix D.

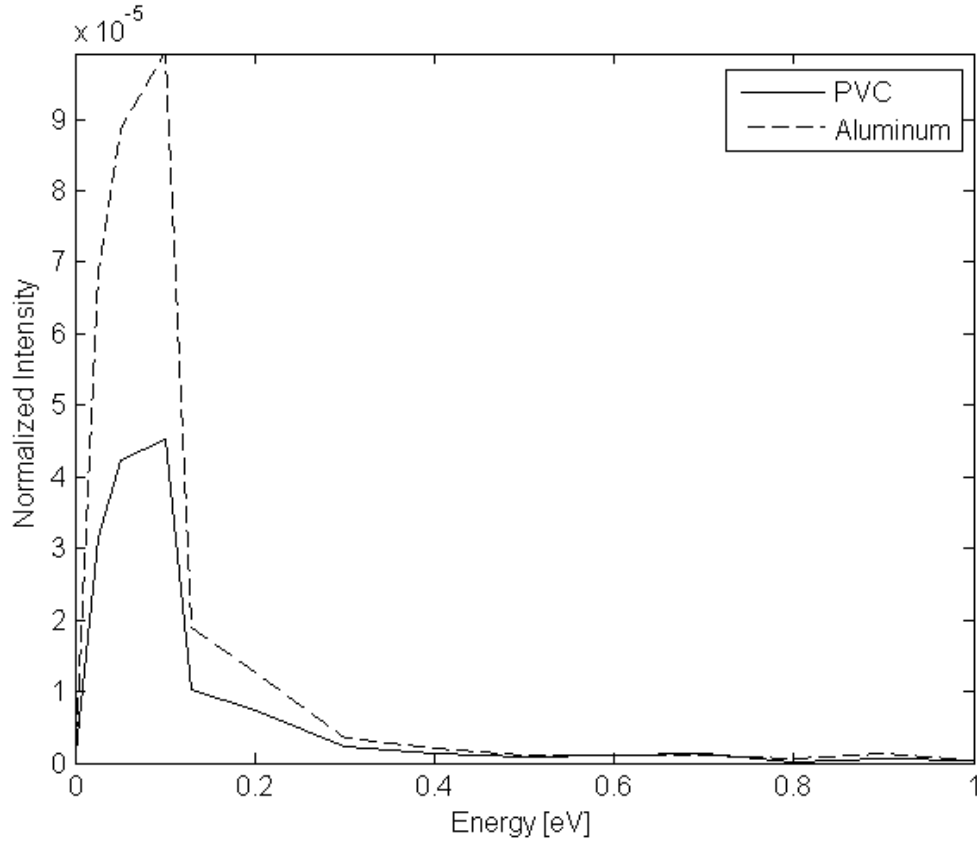


Fig. 23 The differential neutron flux at the beam tube output of the PuBe source for the two neutron howitzer designs.

Because the lowest energy of the PuBe spectrum was modeled as 0.5 MeV, it is believed that the model produced conservative results since the differential neutron flux of the PuBe source does have a low energy component which would add to the population of Fig. 23. The ‘normalized intensity’ is a model output parameter that can be thought of as the probability per source neutron, PPSN. It is the fraction per emitted source neutron

that would be present at the modeled location. For example, the output of the PuBe source in December of 2009 was approximately 1.14×10^7 n/s according to Appendix C. The howitzer output with PVC construction should yield a 0.1 eV flux of approximately $500 \text{ n/cm}^2 \text{ s}$ which results from multiplying the neutron activity by the normalized intensity of $\sim 4.5 \times 10^{-5}$.

4.1.2 Coincident Gamma-Ray Instrumentation Scheme

In order to add credibility to the detection of a neutron pulse, LaBr(Ce) scintillation detectors were emplaced to provide a gate signal to the multi-channel buffer (MCB) when an 1107.6 keV gamma ray was detected. An 1107.6 KeV emission corresponds to an excited Gd-158 nucleus emitting a pair of gamma-rays of energy 6750.2 and 1107.6 keV. It is known that, of the 19.1% of the Gd-158 de-excitations following neutron capture, 11.3% will result in the sum emission of 7857.9 keV which will be the mentioned binary pair 13.6% of the time (See Fig. 4). The initial instrument scheme was established as illustrated in Fig. 24. It was discovered that the PMTs integrated with the scintillators had a significantly different response and that the use of only one Single Channel Analyzer (SCA) would not work.

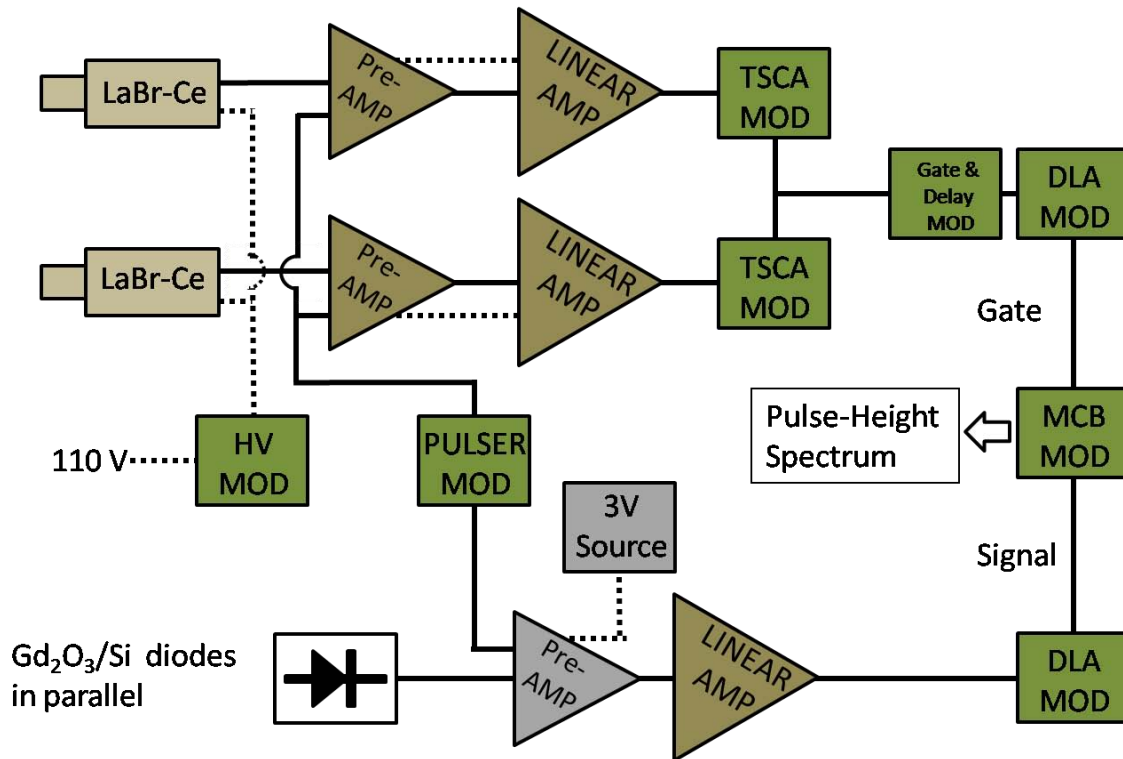


Fig. 25 The final instrument scheme for coincident measurement. The use of separate amplifiers and SCAs allowed each scintillator circuit to be calibrated to send a gate pulse upon the detection of an 1107.6 keV event.

A digital signal from either SCA provided the Multi-Channel Buffer (MCB) with a gate signal. The MCB would only accept an analog signal from the diode when a gate pulse was present. The delay line amplifiers (DLA) in the scheme are needed to compensate for the delay in receiving the gamma signal and the collection of the diode signal following a neutron capture. The gate and delay module allowed for amplitude and duration adjustments of the gate signal fed to the MCB. A bench-test of the system using a pulser and a Co-60 source was conducted to proof the scheme and roughly calibrate the delay required in each leg. The test arrangement is depicted in Fig. 26.

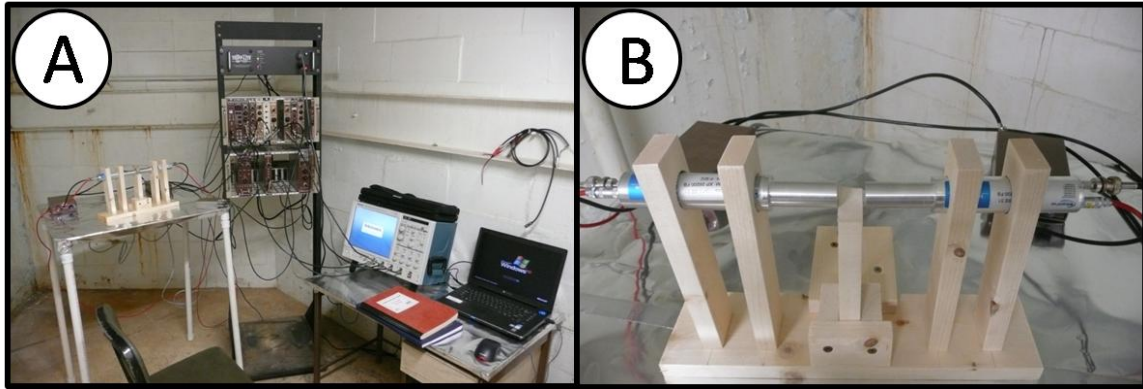


Fig. 26 Bench testing the coincident detection scheme. ‘A’ The instrumentation setup on the bench. ‘B’ a detail of the LaBr(Ce) scintillator and integrated PMTs.

A complete listing of the equipment and the instrument settings can be found in Appendix K. The pulse height spectra were produced using the software package GammaVision version 6.01 [33].

4.1.3 Establishing the laboratory

The laboratory was established in the ‘Neutron Room’ located in the basement of building 470. The room is constructed with borated concrete in the ceiling and walls. The electrical circuit powering the room was found to be noisy and both an uninterruptible power supply (UPS) and a power conditioner were placed in the lab. A neutron and gamma survey was conducted in the lab before and after the neutron howitzer was loaded with the 5 Ci PuBe source. Fig. 27 and Fig. 28 graphically depict the surveys of the lab.

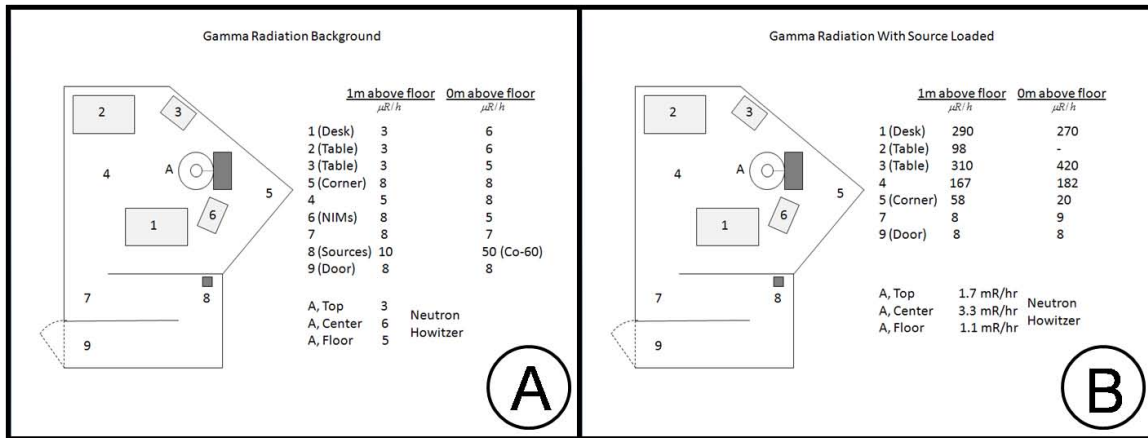


Fig. 27 A schematic of the laboratory depicting the results of the gamma radiation survey before and after loading the howitzer. 'A' indicates background gamma levels prior to loading the howitzer, 'B' indicates the levels after loading with the source in the beam position. Location 8 is a lead box housing a small Co-60 test source.

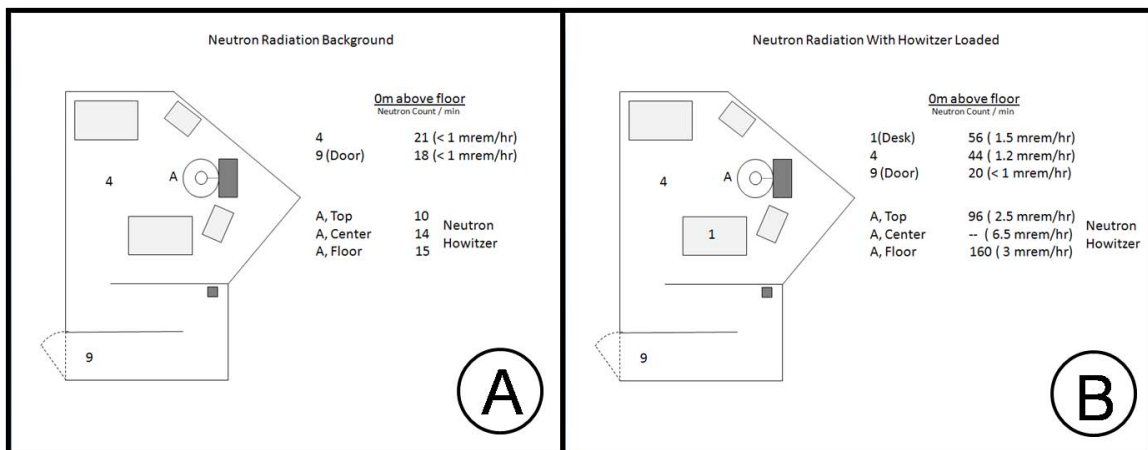


Fig. 28 A schematic of the laboratory depicting the results of the neutron radiation survey before and after loading the howitzer. 'A' indicates levels prior to loading the howitzer, 'B' indicates the levels after loading with the source in the beam position.

The WPAFB Radiation Safety Office conducted an independent survey of the lab and surrounding basement area and concluded that this laboratory setup did not pose a risk to non-research personnel working in the basement.

4.2 Calibration of the Coincident Gamma-Ray Instrumentation

Each scintillator ‘leg’ of the coincident detection scheme was independently calibrated using a pulser and a Co-60 source that provided 2 readily identifiable peaks at 1173.237 and 1332.501 keV. After establishing the amplification settings that placed the Co-60 peaks near the midpoint (5V) of the pulse-height spectrum (PHS), an amplified pulser signal of known amplitude was fed into each SCA. The output of the SCA was fed into a counter module as illustrated in Fig. 29.

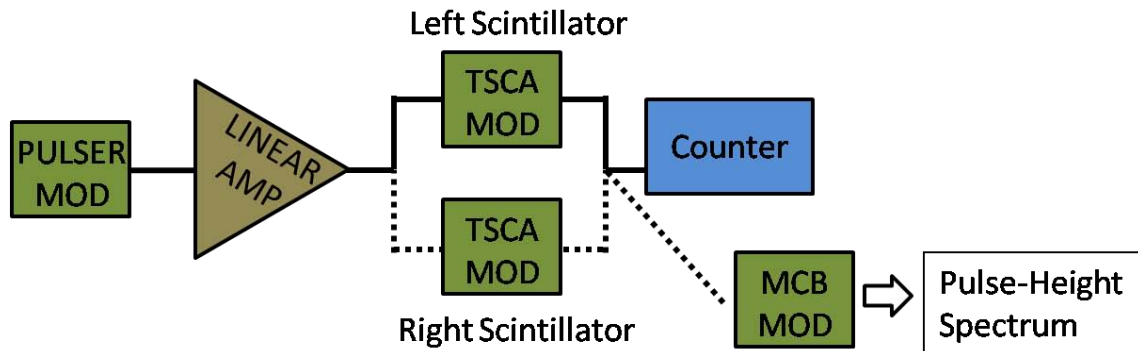


Fig. 29 The SCA configuration calibration scheme. The pulser signal could be used without amplification, but the amplified pulser signal emulates the shaping effects found in the detector signal for a more accurate calibration.

With the SCA in normal mode, the upper and lower adjustment knobs were used to find the point at which the SCA stopped sending a digital pulse to the counter. The same pulser signal was sent to the MCB and the centroid of the peak was determined. A nearly-linear relationship was determined between the signal amplitude, PHS channel, and SCA dial settings. For the same amplification settings, a Co-60 PHS provided a 2 point energy calibration that was used to determine the channel at which an 1107.6 keV pulse would bin. To this channel was added half the number of channels required to reach the centroid of the 1187.2 keV peak. This is next most likely peak emitted as a

binary pair from a de-excitation of a Gd-158 directly to the ground state (see Fig. 4).

The upper and lower channels were then converted to dial settings for the SCA. The SCA will now pass a gate pulse whenever an 1107.6 ± 40 keV signal is detected. The non-linear response of the detector and 2-point calibration was offset by the close proximity of the Co-60 peaks and the narrow region of interest around 1107.6 keV. Table VII summarizes the data used to calibrate both detection circuits. The instrument settings used for calibration can be found in Appendix J as Setting Group 1.

TABLE VII A summary of the Coincident Gamma Detection calibration

Left Detector (SN# P902)				Right Detector (SN# P572)			
Linear Amplifier Settings				Linear Amplifier Settings			
CG	FG	Shape Time	Input negative	CG	FG	Shape Time	Input negative
20	5	0.5 μ s	e	20	5.02	0.5 μ s	e
Pulse [V]	Centroid	UL Dial	LL Dial	Pulse [V]	Centroid	UL Dial	LL Dial
10.06	1805	10.02	8.70	10.06	1805	na	na
5.08	903	5.03	4.98	5.08	903	5.15	5.02
1.99	357	2.01	2.00	1.99	357	2.08	2.00
0.996	176	1.00	1.01	0.996	176	1.03	1.00
Co-60 Peaks [Chan.]		Peak of 1107.6 keV [Chan.]		Co-60 Peaks [Chan.]		Peak of 1107.6 keV [Chan.]	
1312.26	1488.27	1272.57		751.04	852.83	732.1	
Number of Channels for 80 keV:			91.92	Number of Channels for 80 keV:			54.75
Lower Limit [Channel]:			1228	Lower Limit [Channel]:			705
Upper Limit [Channel]:			1318	Upper Limit [Channel]:			759
Lower Dial Setting of SCA:			6.13	Lower Dial Setting of SCA:			3.67
Upper Dial Setting of SCA:			7.28	Upper Dial Setting of SCA:			4.20

The data in Table VII was used to find the relationships between PHS channel as it relates to both SCA dial settings and energy. These relationships are summarized in (27) through (32) where LSUD is left side SCA, Upper Dial Setting, and LSE is left side energy in keV *etc.* All dial setting relationships had R^2 values of over 98% indicating that a linear relationship is appropriate.

$$LSUD = 0.0055(PHS_{Channel}) + 0.0301 \quad (27)$$

$$LSLD = 0.0047(PHS_{Channel}) + 0.3534 \quad (28)$$

$$RSUD = 0.0029(PHS_{Channel}) - 0.2107 \quad (29)$$

$$RSLD = 0.0028(PHS_{Channel}) - 0.2215 \quad (30)$$

$$LSE_{keV} = 0.8703(PHS_{Channel}) + 0.0792 \quad (31)$$

$$RSE_{keV} = 1.4611(PHS_{Channel}) + 37.933 \quad (32)$$

In the course of calibration, it was observed that the gamma background from the PuBe source was significant even though lead shielding surrounded the scintillators. The detectors were set in a lead pile next to the neutron howitzer as shown in Fig. 30.

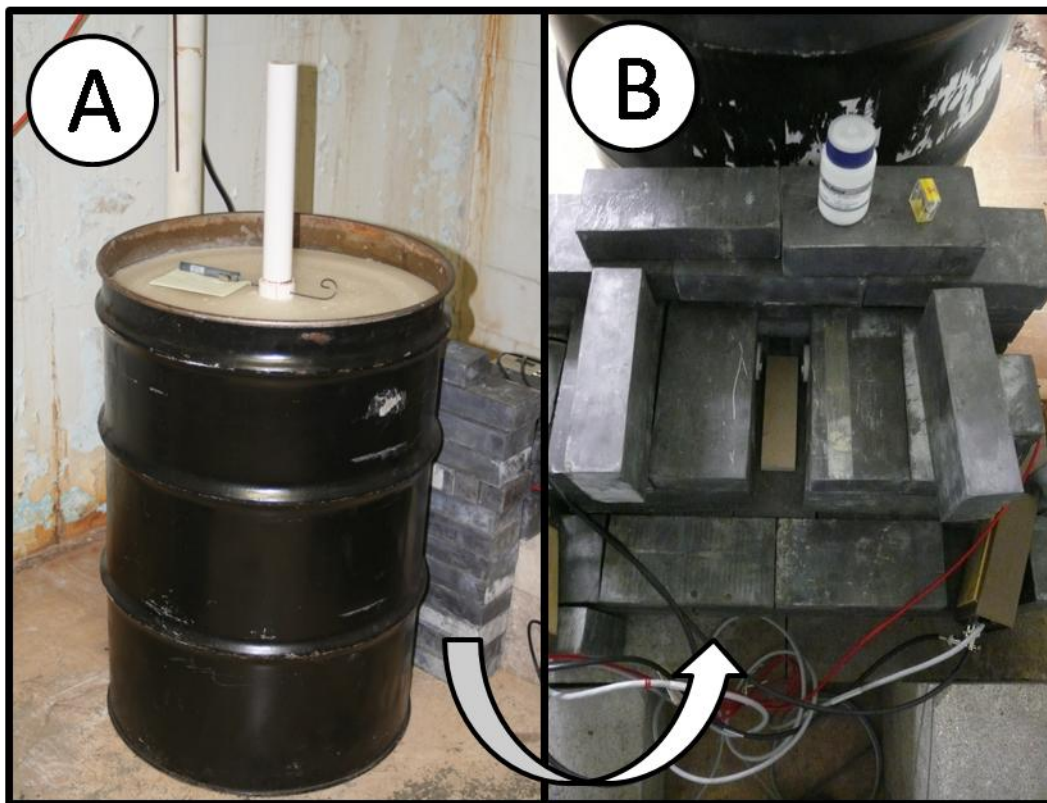


Fig. 30 A lead shield was constructed next to the neutron howitzer as shown in ‘A’. ‘B’ is a view of the lead pile from behind the howitzer. Visible are two pieces of PVC pipe that contain the LaBr detectors opposing each other. Lead would normally cover the top of the channel but it was removed for the photo. The beam tube is centered on the channel containing the block of wood which was used as a stand to raise the Co-60 source closer to the detectors. Also visible in ‘B’ is the Co-60 source and a bottle of Gadolinium Oxide.

The initial shielding around the LaBr detectors was 4” of lead. The nominal activity of the PuBe source is 5 Ci, or 1.85×10^{11} gammas per second. Using the average gamma energy value of 200 keV, the 10th thickness of lead is 0.08”. Achieving a 10^{10} reduction of the average gamma intensity required 10” of lead. The lead shielding was re-built to provide 12” of lead between the PuBe source and the scintillators. The background decreased as expected. Fig. 31 shows a comparison of the pulse-height spectra using both a 4” and 12” lead shield. The spectra agree with published photon spectra of PuBe sources [26].

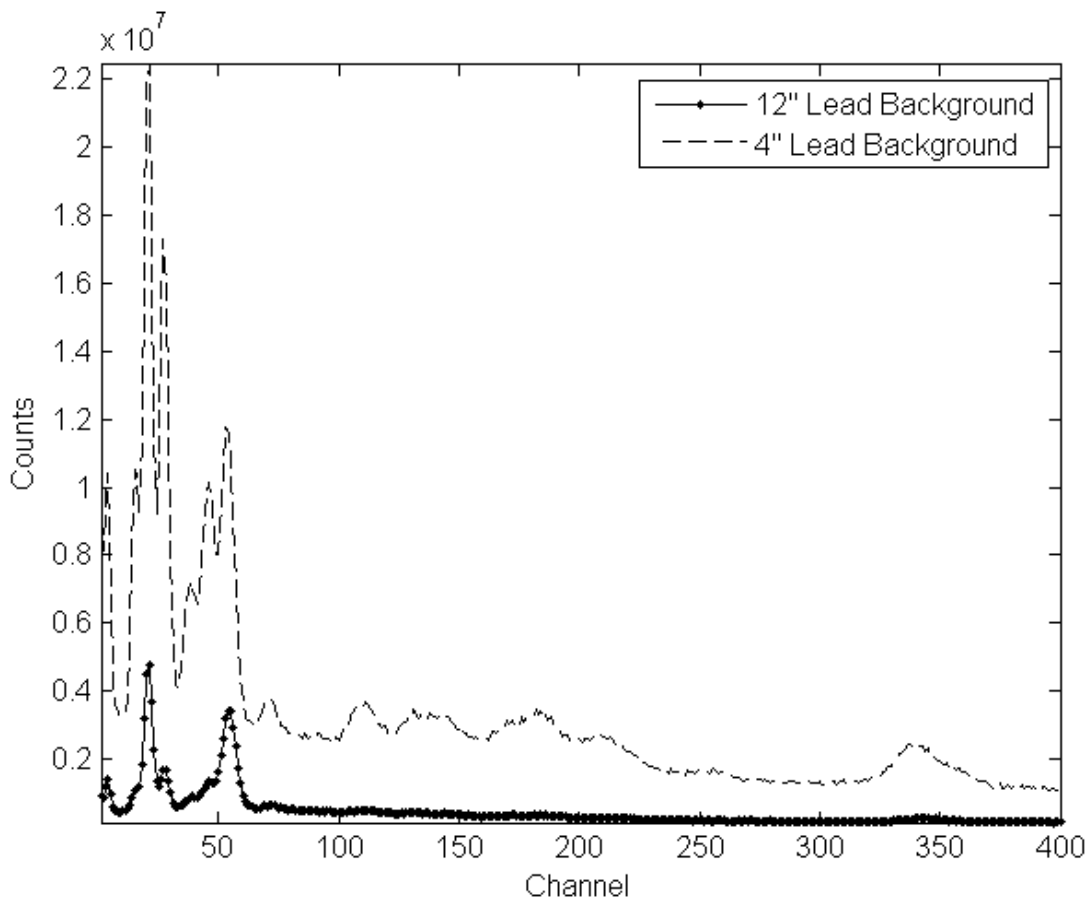


Fig. 31 The pulse-height spectrum taken with the LaBr detectors at the diode location in the lead shielding next to the neutron howitzer. The counting interval was 3600s (1 hr) of live time.

A Co-60 source was used to provide an energy reference in order to identify the region of interest for the 1107.6 keV peak. Fig. 32 is an example of a pulse-height spectrum of the PuBe gamma background with a Co-60 spectrum overlaid. The peak amplitudes for comparison are somewhat arbitrary due to different sample times, but the Co-60 peaks in this spectrum are clearly visible at channels 777 and 886. Using the calibration procedure previously presented, the centroid of the 1107.6 keV peak would be expected in channel 732.

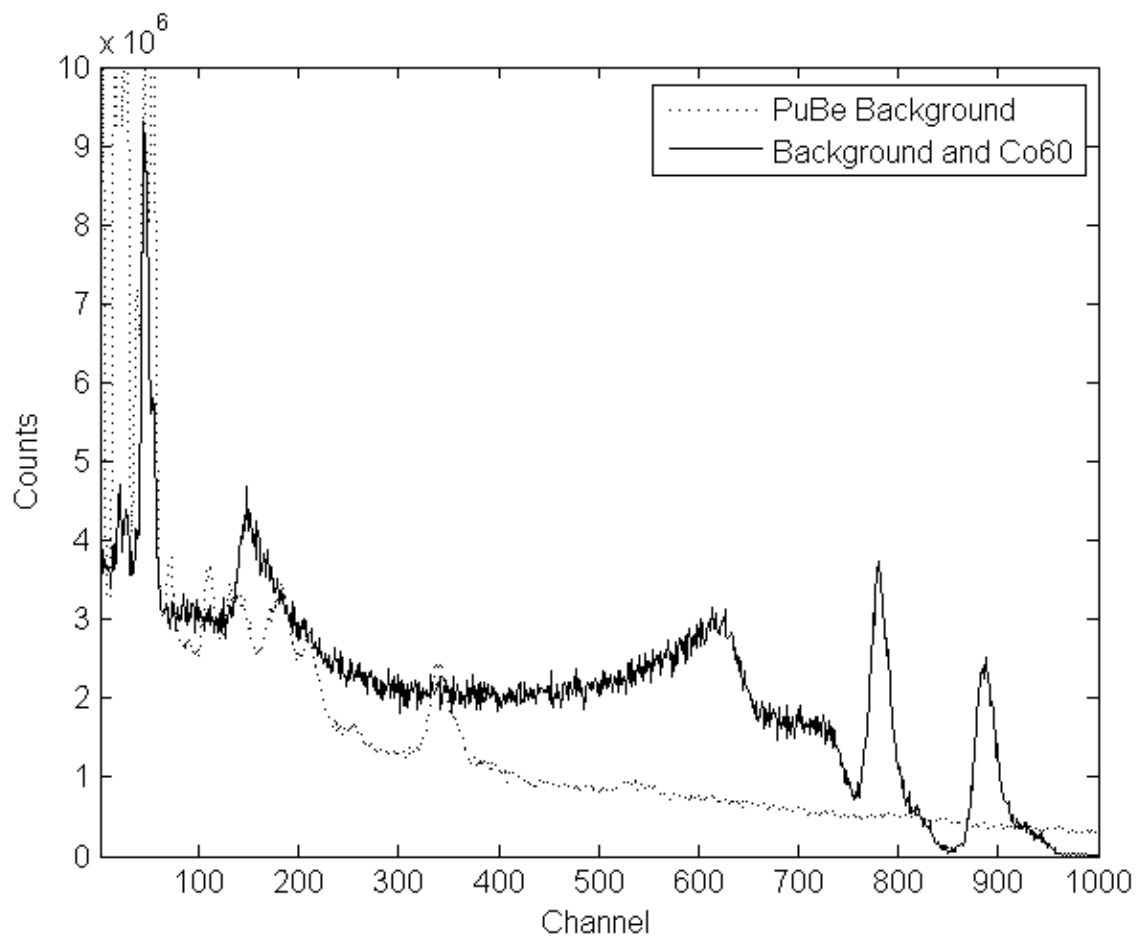


Fig. 32 A (PuBe + Co60) gamma spectrum overlaid onto a PuBe only gamma spectrum background. The 1173.237 and 1332.501 keV peaks of Co60 are readily identifiable at channels 777 and 886. The counting times of the two spectra are not the same and peak amplitudes cannot be compared on this figure.

4.3 Neutron Detection Experiment using Neutron Howitzer

The diodes were ruggedized for experimentation by fixing the wafer containing the diodes onto a plastic frame. Metal leads were set into the plastic frame to which gold wires were affixed, terminating at the diode contacts. Silver paint was used to make these connections. Wire was soldered to the leads on the outside of the plastic frame. The wires were connected in parallel and terminated with a BNC connector. Prior to assembly, each diode was verified for rectification by observing the $I(V)$ response using a Kiethley 4200 SCS. After assembly, each diode was again verified for rectification to ensure all contacts were acceptable. Three diode samples were prepared, each containing 4 to 6 individual diodes in parallel to increase the detector volume as depicted in Fig. 33. The samples were placed between the LaBr scintillators as closely as possible to maximize geometric efficiency as pictured in Fig. 34.

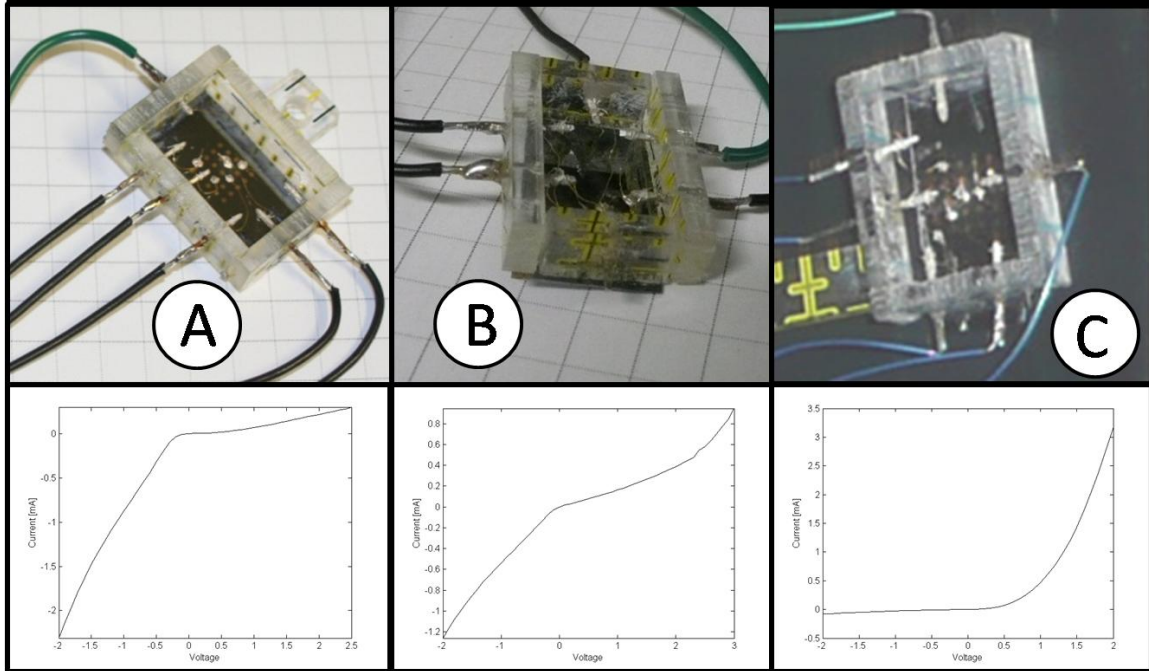


Fig. 33 Three diode samples were prepared for experimentation. Diode 3, shown in 'C' had the best characteristics and was used for all experimentation.

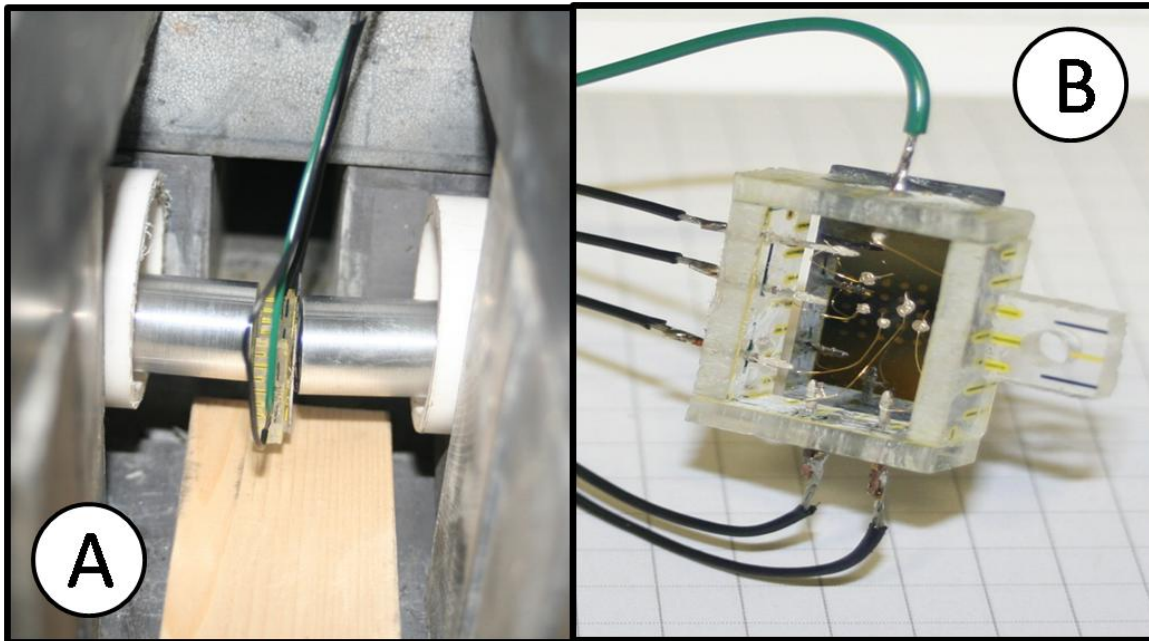


Fig. 34 The diodes were placed as close to the LaBr crystals as possible to maximize the geometric efficiency. 'B' is a close-up of the diode sample mount showing the gold wires leading from the diode contacts.

The samples were connected to 1 of 2 different powered pre-amps in an AC coupled mode. An ORTEC Model 142IH pre-amp was used as well as an Amptek A250CF which is self-cooled and has exceptionally low noise characteristics. The bias was provided through the pre-amp from a Mastech HY3006D digital power supply set at -1.500 V. The pre-amp signal was output to an ORTEC 572A linear amplifier which was set at the lowest gain, nominally a factor of 10. The amplifier contains an active filter circuit and requires a shaping time input which is nominally the time required for the detector to collect a pulse. The charge collection time was calculated by determining the electron velocity within the active detection region of the diode. Because the majority of the depleted region is silicon, the electron mobility was taken as $1400 \times 10^{-4} \text{ m}^2/\text{V s}$ and the relative permeability as 11.68. The electron velocity was calculated from (33) where V is the drift velocity, μ is the mobility, and ε is the electric field. The field is represented by (34). The distance, d , is the region over which the bias generates a field. This distance, taken as $0.7 \text{ }\mu\text{m}$, is graphically depicted in Fig. 35 as the region of energy band ‘bending’ in the heterojunction band structure model.

$$V_n = -\mu_n \varepsilon \quad (33)$$

$$\varepsilon = \frac{\text{Bias}}{d \times k} \quad (34)$$

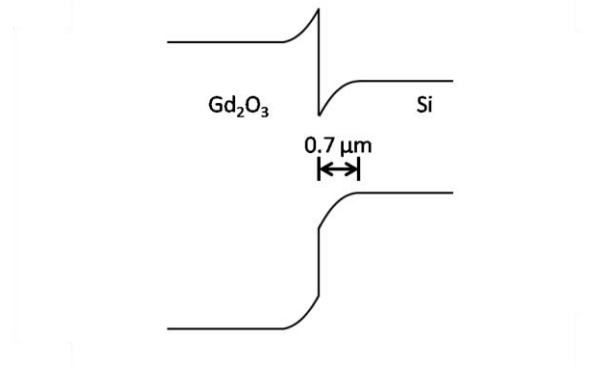


Fig. 35 A simple band structure model of the Gd2O3/Si heterojunction. The electric field created by the applied bias is limited to a region approximately 0.7 μm in length.

The distance over which the electrons must move in order to be collected is the diffusion length of an electron in p-Si. Taking the effective mass of an electron as 26% of the electron rest mass m_0 , the electron recombination time, τ_n , is determined by (35) where q is the electronic charge [22]. In practice, this is a difficult factor to determine and was taken to be 1 μs which is a nominal value for p-Si.

$$\tau_n = \frac{(0.26)m_0\mu_n}{q} \quad (35)$$

The diffusivity, D_n , was calculated using (36) assuming a temperature of 300K. The diffusivity is $3.6 \times 10^3 \text{ m}^2/\text{s}$.

$$D_n = \frac{kT}{q} \times \mu_n \quad (36)$$

The diffusion length, L_n , is calculated by (37) once diffusivity and the recombination time are known. The diffusion length was determined to be approximately 60 μm .

$$L_n = \sqrt{(D_n\tau_n)} \quad (37)$$

The time required to collect a pulse is then the length the electrons travel to the depletion region divided by their velocity depicted as (33). The collection time was found to be 0.3 μs using (38). The lowest shaping time constant of 0.5 μs was selected.

$$\text{Collection Time} = \frac{L_n}{V_n} \quad (38)$$

In order to calculate the time required to observe neutron pulses in coincidence with detected 1107.6 keV gamma rays, the reaction rate was calculated assuming a thermal neutron flux of 500 /cm² s and 5 diodes wired in parallel. The reaction rate was calculated using (39) where ϕ is the thermal neutron flux, σ , is the thermal neutron cross-section for absorption, and #Gd is the number of Gadolinium nuclei in the active region of the diode.

$$\text{Reaction Rate} = (\#Gd) \times \phi \times \sigma \quad (39)$$

The reaction rate was determined to be 2.42 reactions per second. In order to determine the rate at which 1107.6 keV gammas may be detected in coincidence with a neutron capture, the rate is multiplied by several factors. First, the known de-excitation fractions from Fig. 4 and the internal conversion coefficient (30%) are applied to the reaction rate (39) to find the rate at which 79 keV internal conversion electrons are produced simultaneously with coincident 1107.6 keV gamma emissions.

$$\text{Rate of coincident emissions} = \text{Reaction Rate} \times 0.113 \times 0.136 \times 0.30 \quad (40)$$

The rate of coincident emissions was found to be 0.0056 per second. To this rate, an efficiency factor is applied for the LaBr detectors. The geometric efficiency was

determined by using the solid angle between the detectors and the diode. This quantity was calculated to be 0.132 using two 0.18 cm diameter LaBr crystals spaced 0.75 and 0.1 cm away from the diode. Because there is no published efficiency data available for these detectors at the energy of interest, the geometric efficiency was taken as the total efficiency. The final factor is the number of internal conversion electrons that will not deposit an appreciable amount of their energy within the active volume. A first order estimate for this value is 0.25 which is only a qualitative value. A more rigorous approach to determine this value using a numerical model was not performed. Multiplying the rate of coincident emissions by the geometric efficiency and fraction of lost internal conversion electrons yields 0.00018 countable events per second. In order to count 100 neutron capture events capable of being detected by coincident gamma emission, it would require 6.3 days of counting. The details of this calculation can be found in Appendix A.

In order to increase the reaction rate and validate the scintillator instrumentation, a bottle of gadolinium oxide was placed between the detectors. This provided a Gd target for neutrons in order to provide a large number of neutron interactions and subsequent emission of 1107.6 keV gammas. This energy peak was expected to have a higher intensity than the other known lines from the de-excitation of meta-stable Gd-158 as depicted in Fig. 4. However, the energy peak was not identified above the background using the 12" thick lead shielding arrangement. It could roughly be expected that the neutron flux would be diminished by 1/9 when the shielding was increased from 4" to 12". In an effort to increase the neutron flux, the shielding was reduced to 4" and the

experiment was repeated. Either the target gamma was present and could not be distinguished from the background or too few neutron interactions were being observed. Several experiments were conducted over count times as long as several days but a signal indicative of neutron interaction was not observed in either the diode or the scintillator spectra.

A current mode measurement scheme was developed to observe the diode energy signal as an alternative to the pulse mode scheme previously developed. The instrument configuration is graphically depicted in Fig. 36 where a pico-ammeter is placed in a closed loop between the diode and the bias source.

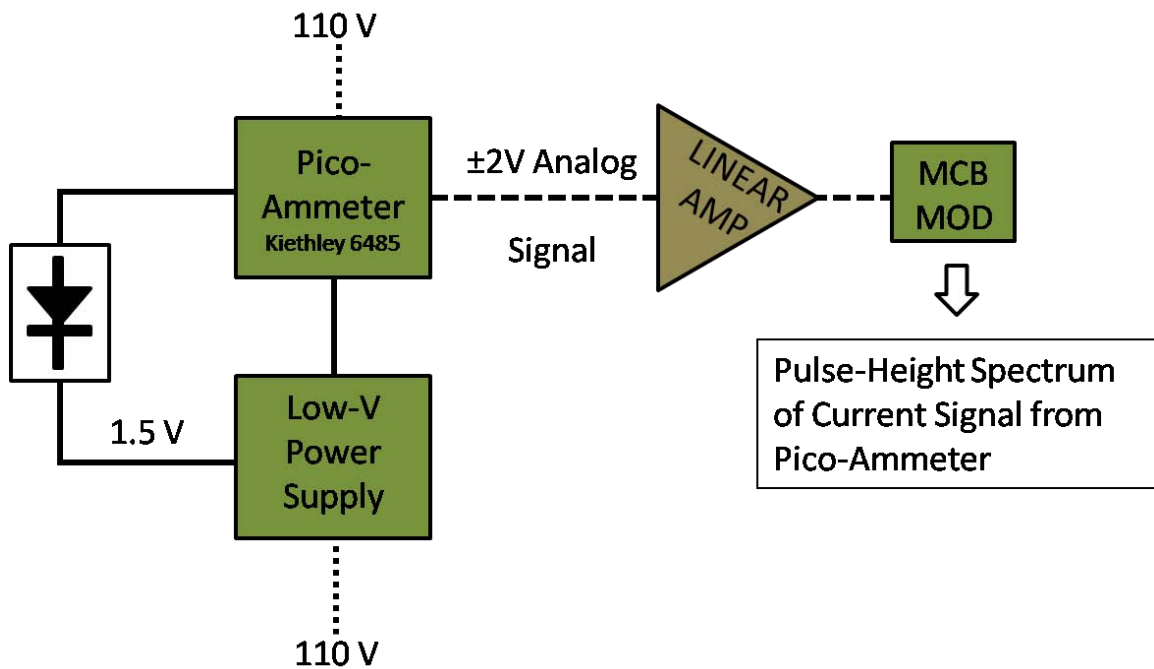


Fig. 36 The instrument diagram for the current mode measurement scheme.

This arrangement records the average current as developed over many pulses. The Kiethley 6485 Pico-Ammeter was set to operate in the nano-amp range with a 2 nA full scale setting. This provided an analog output representing 2.1 nA as a full 2V signal which was input to the linear amplifier set at a gain of 1500. The instrument settings can be found in Appendix J under Group 2. This high-gain regime allowed for the use of a larger portion of the MCB channels but also caused a high dead time which was reduced by setting the low level discriminator on the MCB to 2.28V. The instrument settings used for this experiment can be found in Appendix J as Setting Group 2. A splitter box was constructed in order to maintain the use of coaxial cables and connect the devices as described. A diagram and picture of the splitter box is shown in Fig. 37.

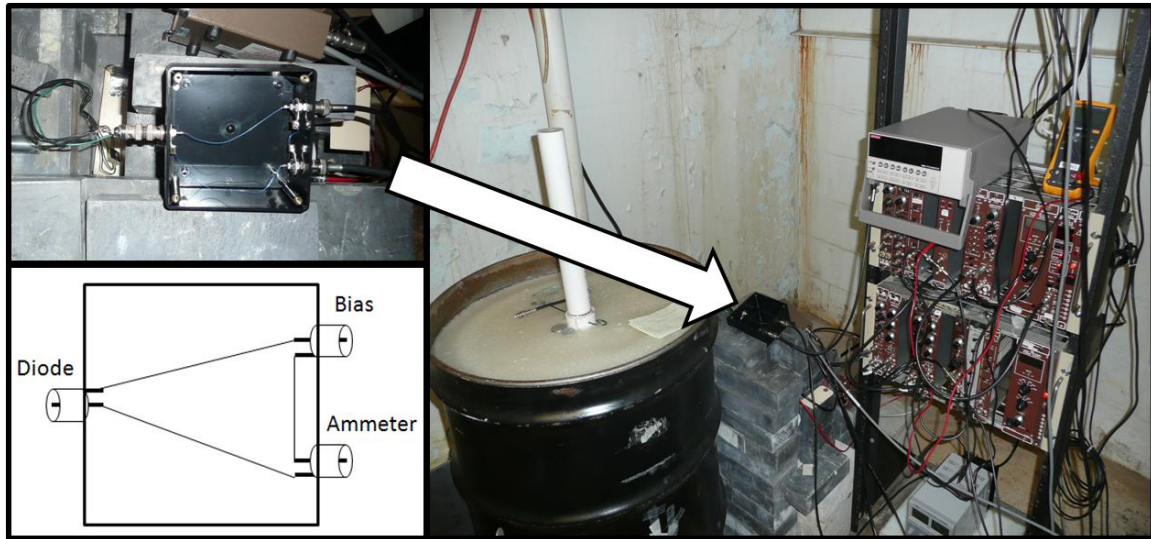


Fig. 37 The current mode experiment required a splitter box in order to continue the use of coaxial cables and BNC connectors.

A pulse-height spectrum produced in accordance with Fig. 36 represents an average current value measured by the ammeter multiple times over the counting period. After the instrumentation was established, a system noise measurement was made by turning

the power off at the ammeter and recording a PHS for 1 hr. The largest pulse amplitude was below 200 counts. The bias was applied and the current was measured for 1 hour with the source present followed by a similar count with the source removed. Fig. 38 graphically depicts the results. Comparing the two spectra, the diode developed a higher current in the presence of the source. The down-turn at channel 365 is an artifact of the MCB and is the LLD threshold that was set to reduce dead-time. This was the first evidence that the diode responded to radiation of some type.

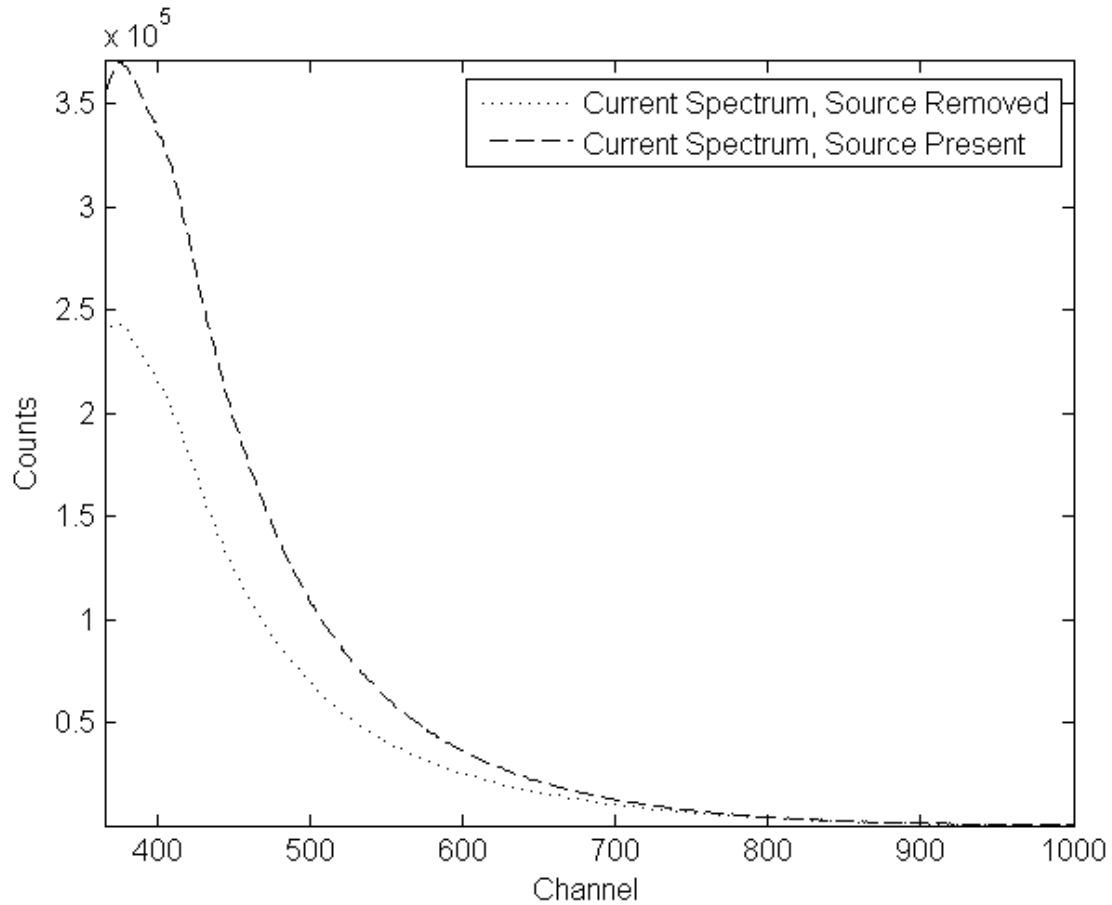


Fig. 38 The average current measured in the diode with and without the PuBe source present. The average current was higher when the source was present.

4.4 Neutron Flux Measurement and Calibration

A neutron counting experiment using a BF_3 detector was conducted in order to determine the actual thermal neutron flux at the diode location. BF_3 detectors are sensitive to slow neutrons and use the B-10 reaction presented as (4). The products of a B-10 neutron capture reaction are Li-7, an alpha particle, and a gamma ray. The heavy products have significant recoil energy and cause secondary ionization in the BF_3 gas. The range of the alpha particle in BF_3 gas is approximately 0.375'' which makes it likely that some of them will strike the wall of the tube before depositing all of their energy as ionization in the BF_3 [8]. A nominal pulse-height spectrum for a BF_3 detector is shown in Fig. 39 [8]. The wall effect is shown by the two steps leading to the full energy peak. The 2.31 MeV peak results from the 94% of the reactions in which the Li-7 is born in an excited state [8]. The 2.79 MeV peak results from the 6% of the reactions that result in the production of a ground-state Li-7 nucleus [8].

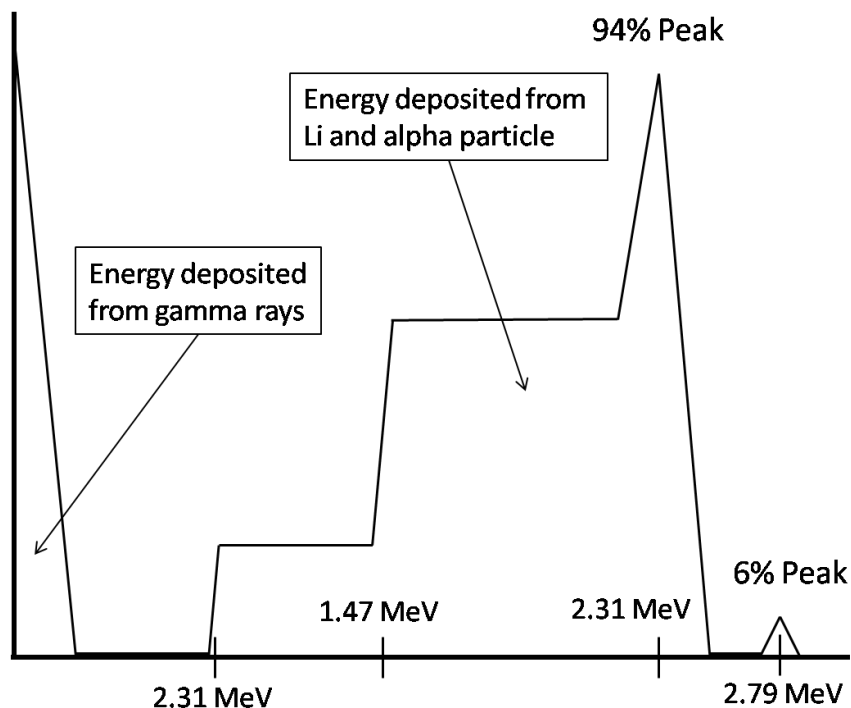


Fig. 39 The idealized pulse height spectrum from a BF_3 detector showing the relative location of the wall effect.

The BF_3 tubes available in the AFIT laboratory are legacy items and manufacturer specification are not known. Serial number H6058 was selected from a group of detectors measuring approximately 14"x1" bearing the part number RS-P4-0812-217. Experiment determined that the appropriate bias for this detector was 1200V. The instrumentation scheme for counting neutron interactions is shown in Fig. 40.

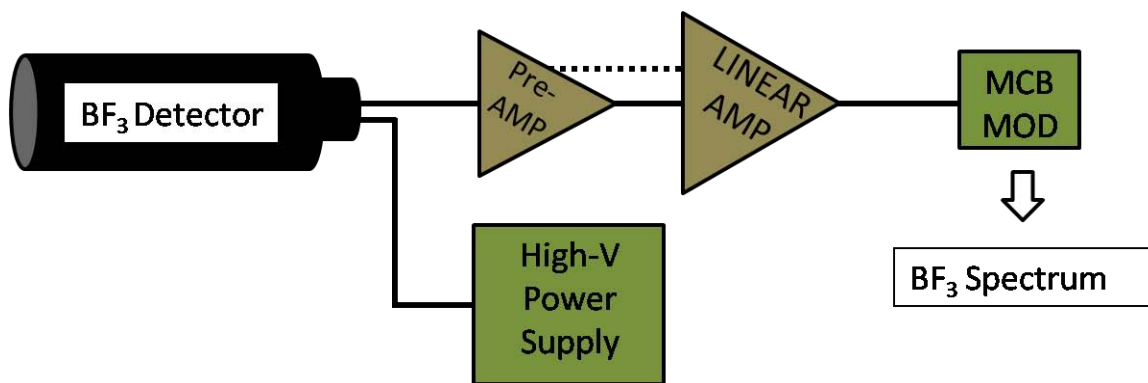


Fig. 40 The BF₃ detector instrumentation scheme.

The detector was biased using an ORTEC 556 high-voltage power supply and coupled to an ORTEC model 113 preamplifier. The signal was input to an ORTEC 572 linear amplifier set to a gain of 25 with a 2 μ s shaping time constant. The LLD was set to exclude channels below 2.31 MeV. The equipment settings are also summarized in Appendix J as Group 6.

Spectra were taken using a 0.33 cm thick Cd shield that could separate in the center to allow a window through the cadmium. The difference between the number of neutron events counted by the Cd covered tube and the partially uncovered tube is the number of neutrons absorbed by the Cd which has a high absorption cross-section as previously discussed. The Cd cover was not completely removed because the internal geometry of the tube was not explicitly known. The use of an exposed region of controlled size in the center of the tube mitigated the existence of insensitive areas of the detector. It was also determined that measurements in the AFIT calibrated graphite pile would experience unmanageable dead-time without partial shielding. The detector was placed into the location normally housing the scintillators in the lead shielding next to the

howitzer. A spectrum was taken with the detector fully shielded and another with a 1'' separation between shield halves. The experiment was repeated to observe the effect on the flux at the diode location when the PuBe was lowered from the beam position to the storage position. Another experiment determined the count behind the howitzer at a point in space analogous to the diode location but not in line-of-sight of the beam tube. The detector was placed 5.25'' away from the howitzer and 17'' up from the floor, the analog to the diode position. The detector was placed as depicted in Fig. 41.

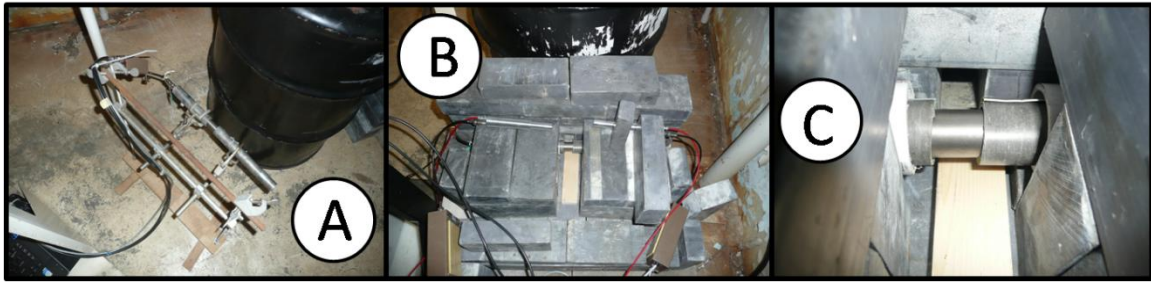


Fig. 41 The positioning of the BF_3 detector for a neutron flux measurement of the neutron howitzer. A measurement was taken at the rear of the howitzer for a comparison to the beam tube side as depicted in 'A'. The measurement at the diode location required the removal of the LaBr detectors so the BF_3 tube could occupy their location in the lead shielding shown in 'B'. The Cd cover over the BF_3 tube could be separated to a precise distance in order to make measurements of the covered and bare detector. 'C' shows a close-up of the detector with the Cd shield separated. The square aperture in the far ground has line-of-sight to the beam port.

A typical experimental pulse height spectrum is shown as Fig. 42. It is believed that the old age of the detector was a contributing factor to the non-ideal spectrum. The sum of the non-gamma ray induced counts was computed using the GammaVision Region of Interest Tool [33]. This sum represents the total number of neutron interactions in the counting period but does not provide information about the energy of the neutrons.

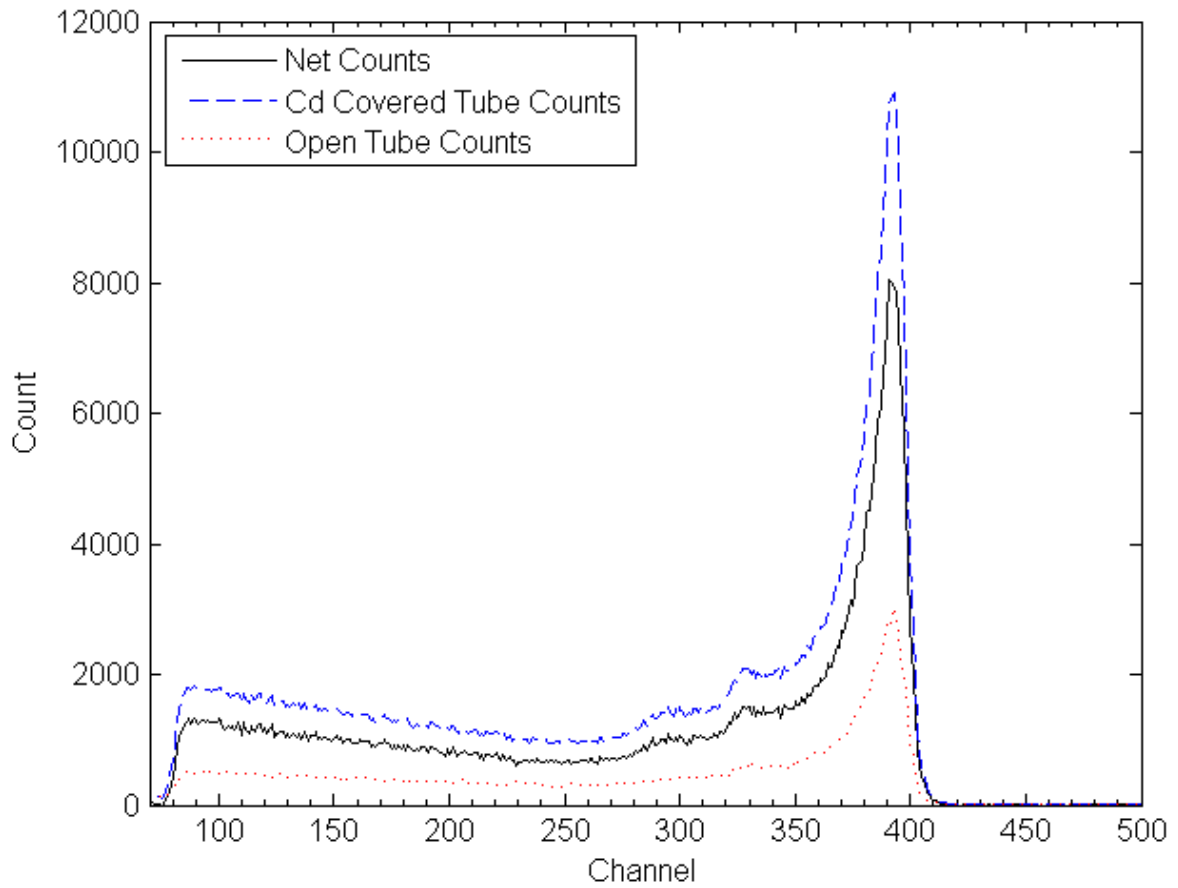


Fig. 42 An experimental pulse height spectrum taken with the BF_3 detector. Shown are three sets of data from a 1 hour count i) a 1" separation of the Cd cover ii) a completely covered detector, and iii) the difference between i and ii. The sum of the counts under the Net Counts line represents the number of neutrons that were absorbed by the Cd shielding.

Using some nominal parameters for BF_3 detectors, the thermal neutron flux was calculated for each data pair. The values used in this calculation are listed in Table VIII. MATLAB[®] was used to compute the flux as described below and the code is included in Appendix G [35].

TABLE VIII The parameters used to calculate the thermal neutron flux using the BF₃ detector.

Parameter	Value
Tube O.D.	1.008"
Tube thickness	0.0825"
Temperature	305.3 K
σ B-10	$3840 \times 10^{-24} \text{ cm}^2$
Pressure	0.9 atm
Count Time	3600 s
PuBe n activity, Sep. 1960	$8.92 \times 10^6 \text{ n/s}$
PuBe n activity, Dec. 2009	$1.13 \times 10^7 \text{ n/s}$
Gas Constant, R	0.0821 L atm/K mol

It was assumed that the macroscopic cross section for BF₃ was primarily from B-10. Rearranging the ideal gas law, the molar density was determined by (41) where V is volume, N is the number of moles of B-10, T is the absolute temperature, P is the absolute pressure, and R is the ideal gas constant.

$$\frac{N}{V} = \frac{P}{RT} \quad (41)$$

The molar density was determined to be 3597 mol/cm³. The macroscopic cross section was then determined by (42) where N_{Avogadro} is Avogadro's Number and σ_{B10th} is the microscopic cross section of thermal neutron absorption for B-10.

$$\Sigma = N_{avogadro} \times \frac{N}{V} \times \sigma_{B10th} \quad (42)$$

The flux was then computed by (43) where t is the counting time, V_{tube} is the volume of the detector exposed by the Cd window, and Σ is the macroscopic cross section from (42).

$$Flux = \frac{(Counts_{Net})}{t \times V_{tube} \times \Sigma} \quad (43)$$

This flux assumes that the Cd shielded neutrons of energy < 0.025 eV and that the detector is 100% efficient. An initial assumption of 10% detector efficiency was applied. The resulting calculated thermal neutron flux at each location is summarized in Table IX.

TABLE IX The calculated thermal neutron flux from the neutron howitzer.

BF ₃ Detector Location	Source Position	Net Counts	Calculated Flux [n/cm ² s]	Assumed 10% eff. Flux [n/cm ² s]
Diode Location	Up	465067	170	1700
Diode Location	Down	221220	81	810
Behind Howitzer	Up	204981	75	750

Assuming a 10% efficiency allowed a simple linear correction. The calculated flux values contain some uncertainty in that the detector efficiency is not well characterized and the assembly specifications are not well understood.

The AFIT standard graphite pile, calibrated to a National Institute of Standards (NIST) standard in 1960, was used to calibrate the BF₃ detector. The standard graphite pile is constructed with multiple drawers that allow for sampling the flux at different locations. Fig. 43 shows the general construction of the pile. The thermal neutron flux is known at the center of each drawer as determined by activated foil techniques [27]. The BF₃ detector experiment was repeated using the same instrument settings in drawers 2, 3, and 4. To accommodate the detector, the drawer stringer was withdrawn until the center of the BF₃ detector was in the center of the pile. The calibrated flux was compensated for the increase in PuBe neutron activity by a factor of 1.27, the ratio of the

PuBe neutron activity in September 1960 to December 2009 [30]. The experimentally determined flux was compared to the calibrated flux as summarized in Table X. The calculated flux assumes 100% detector efficiency and is computed using the BF_3 detector data and the assumed parameters of the detector construction.

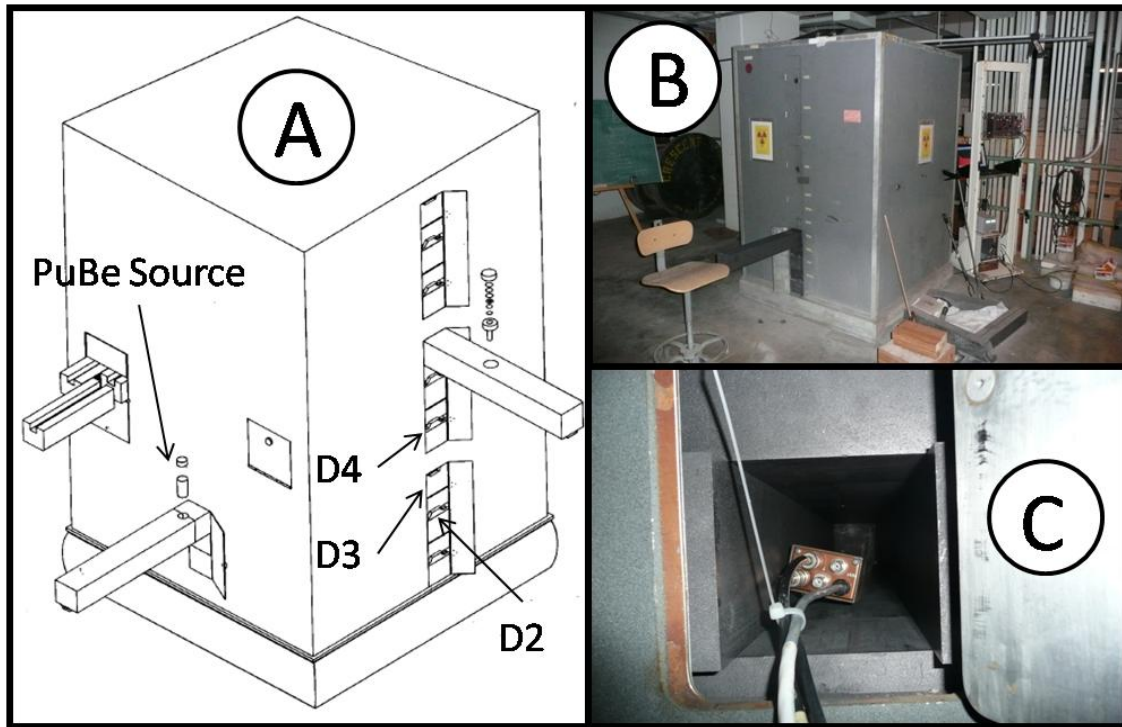


Fig. 43 The AFIT Standard graphite Pile. 'A' shows a diagram of the pile from the original calibration document [27]. The removable graphite stringers, or drawers, that were used for detector calibration are labeled here as D2, D3, and D4. 'B' shows the pile with drawer 3 withdrawn to allow the placement of the BF_3 detector into the pile from the opposite side. 'C' is a view looking into the pile with the pre-amp visible in the foreground.

TABLE X A summary of the calculated and calibrated thermal neutron flux in the AFIT standard graphite pile by drawer position.

BF ₃ Detector Location	Net Counts	Calculated Flux [n/cm ² s]	Calibrated Flux (compensated) [n/cm ² s]	Calculated / Calibrated
Drawer 2	47519100	17378	8839	1.97
Drawer 3	60250919	22034	10117	2.18
Drawer 4	54478284	19923	7307	2.73

It was determined that the computed thermal neutron flux was a factor of 2-3 times the calibrated flux. The disparity between the calibrated and computed values is most likely due to the Cd shield thickness which determined the energy of the neutrons it absorbed. Modeling the problem as a thin neutron beam moving through the Cd into the detector, the attenuation equation can be used to compare the intensity of the transmitted beam, I , to the intensity of the incident beam, I_0 . The mass attenuation coefficient is energy dependent and represented by μ . The density of the Cd is given by ρ . Rearranging (44) to (45) and plotting the cross-section dependent, and thus energy dependent, ratio of incident intensity to the output intensity for 0.33 cm Cd results in Fig. 44.

$$I = I_0 e^{-\frac{\mu}{\rho} \rho x} \quad (44)$$

$$\frac{I}{I_0}(\mu, E) = e^{-\frac{\mu}{\rho} \rho x} \quad (45)$$

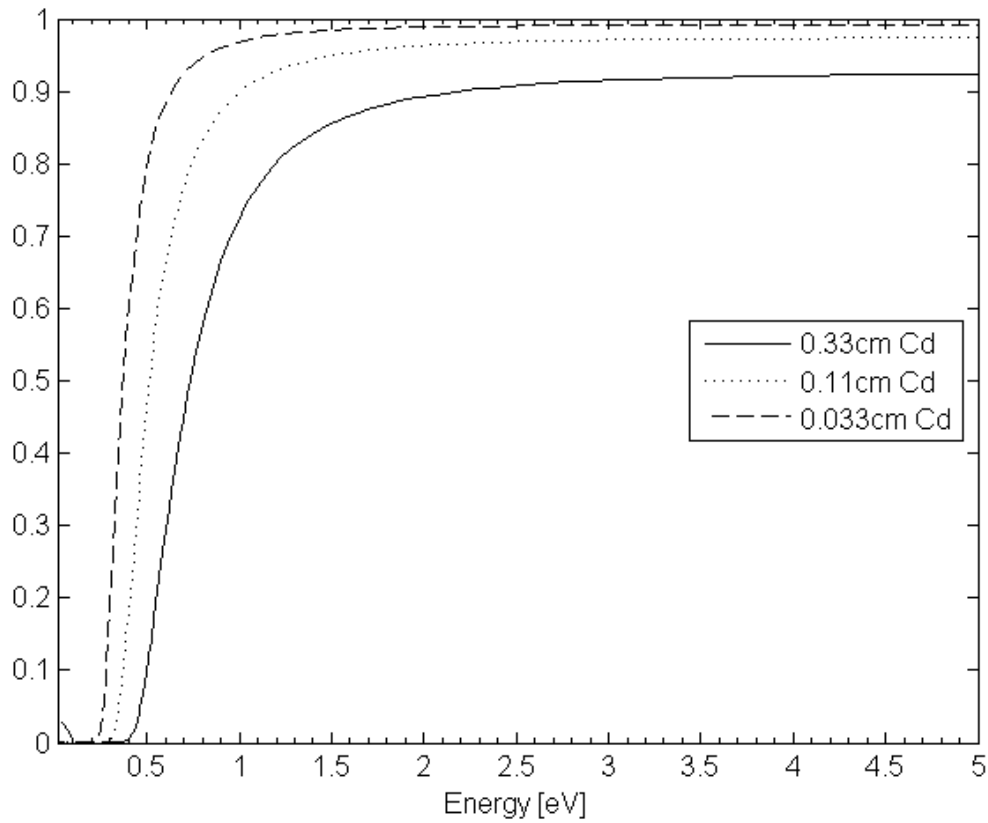


Fig. 44 A plot of I/I_0 vs. neutron energy in the thin beam model for the 0.33cm thick Cd shield compared to the transmittance for 1/3 and 1/10 of the thickness.

The relatively thick Cd absorbed neutrons up to about 0.65 eV. This inflated the computed flux because the thermal neutron cross section for absorption was used as a constant when in fact, a piece-wise calculation using a differential flux would be more appropriate. A thinner Cd shield would have provided a closer fit between the computed and calibrated flux.

The calibration experiment showed that the thermal neutron population in the pile is higher than at the neutron howitzer using the same PuBe source.

4.5 Neutron Detection Experiment using the Graphite Pile

The neutron detection experiment was moved to the graphite pile to capitalize on the higher thermal flux. Unfortunately, the use of the pile precluded the coincident gamma ray detection experiment. The diode sample and ORTEC preamp were set into drawer 3, the highest thermal neutron flux location of the pile shown in Fig. 45.

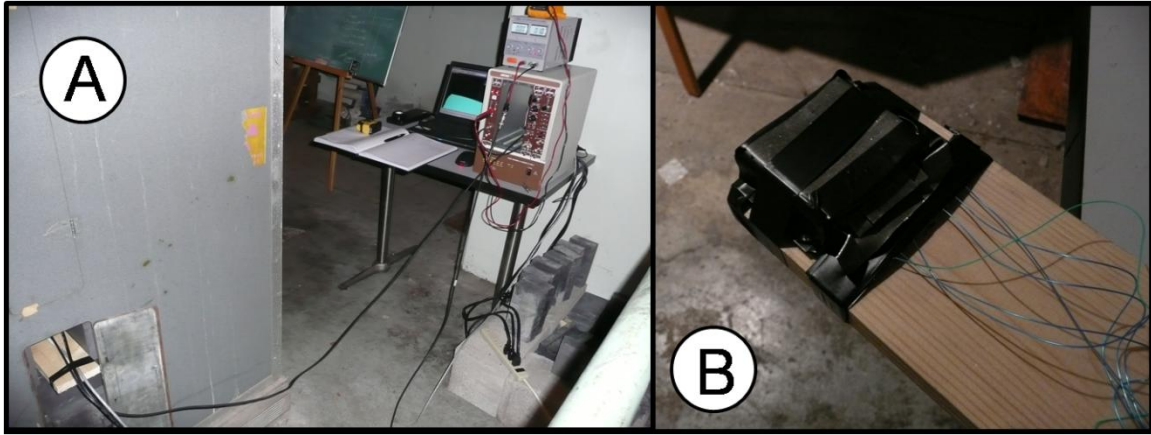


Fig. 45 The diode experiment was conducted in the graphite pile shown as 'A'. Cd and Pb covers were placed around the diode to shield it from the flux in the pile. A Cd shield is shown covering the diode in 'B'. Not visible is the Cd plate beneath the diode (but on top of the board) to completely surround it.

Several experiments were conducted using different gain settings, shaping time constants, and counting periods up to several days. It was discovered that a 3 μ s shaping time constant produced a distinct peak in the spectrum taken with a gain of 10, the lowest gain possible. The integration of the peak yielded 1.84×10^8 counts. This value is 223 times smaller than the total source neutron activity of the counting period, 4.1×10^{10} n/h. A 0.03" thick cadmium cover was placed around the diode to observe the effect of a reduced thermal neutron population on the spectrum. The peak in the spectrum increased in amplitude and the number of counts in the peak increased to 578×10^6 , a factor of 71

times smaller than the entire neutron output of the source. It was highly unlikely that the energy peak was due to neutron interaction because it represented too high of a fraction of the neutron population and it increased when a neutron absorber was introduced. Data was taken with a thicker Cd cover and with a Pb cover. The results are shown in Fig. 46.

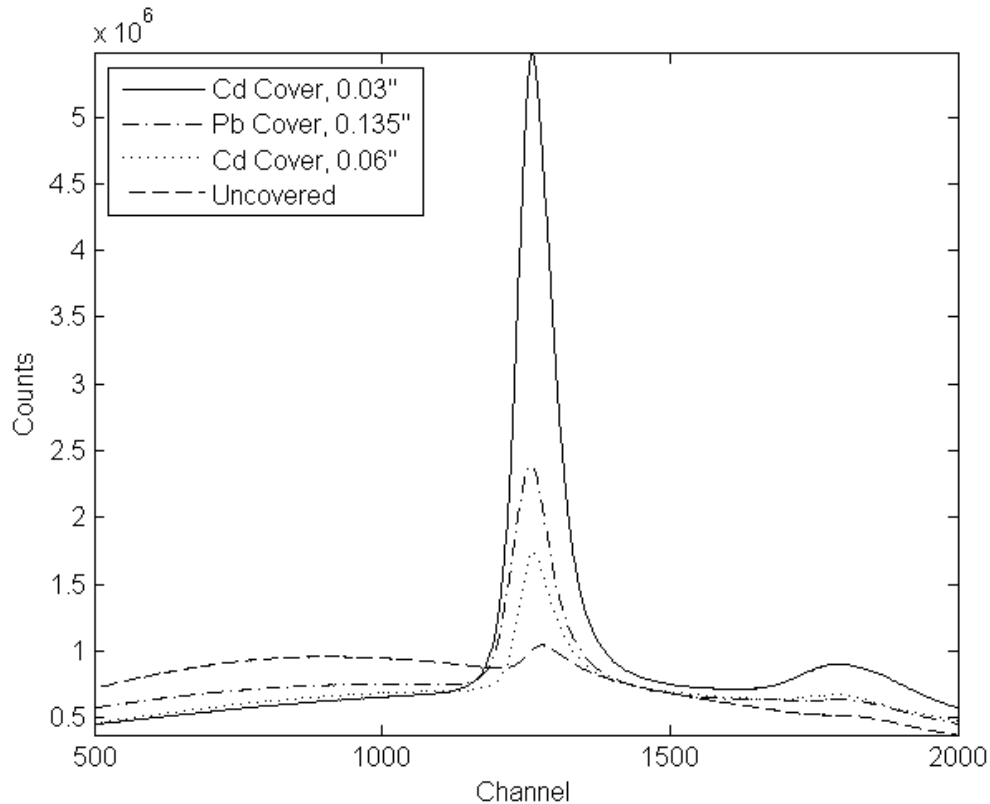


Fig. 46 Pulse height spectra taken with the diode in the pile exposed and covered with Cd or Pb shielding. The peak increases with the addition of a Cd shield compared to the un-shielded diode.

Because this response was only strongly displayed using a shaping time constant of 3 μ s, the instrumentation was changed to reduce the possibility that the signal was an artifact of the electronics. Additional experiments were conducted using the Amptek A250CF preamp which provided a signal with higher resolution and lower noise. A shaping time constant of 0.5 μ s was used with this preamp which agrees with the calculated value for

charge collection time in the diode using (38). The result was generally similar, but the single pronounced peak in the previous experiment was found to be two peaks as shown in Fig. 47.

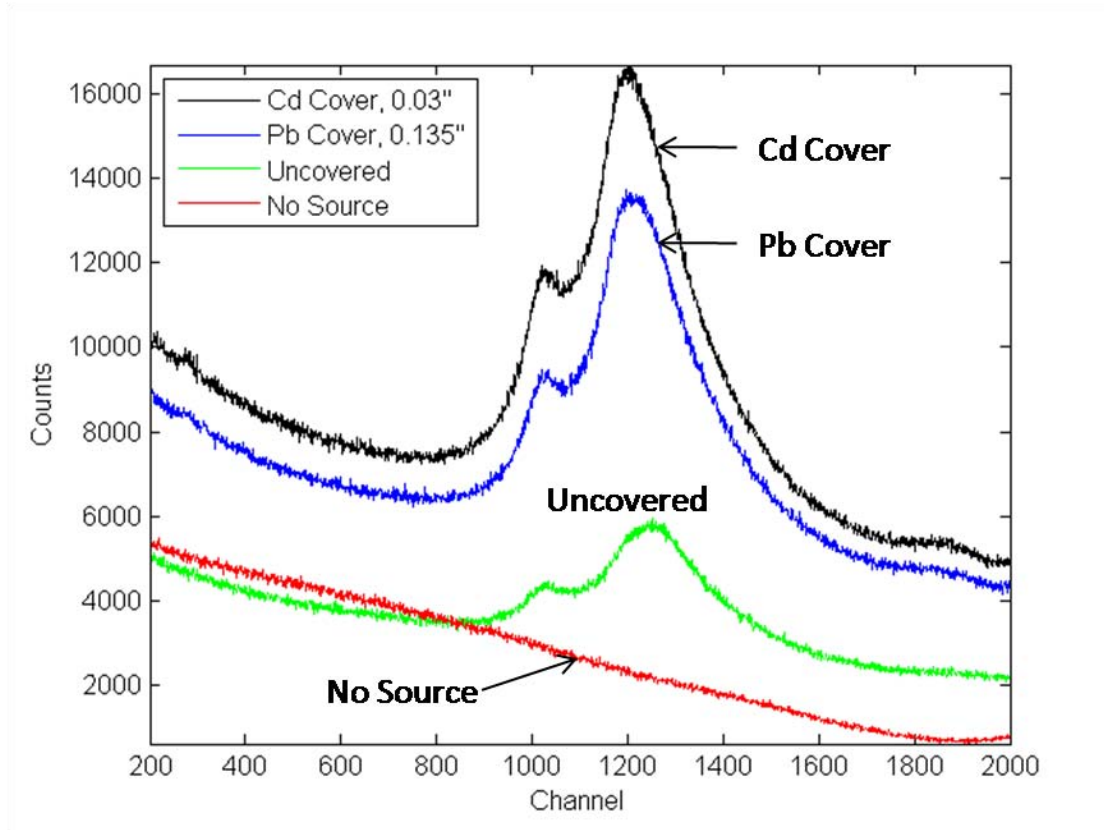


Fig. 47 Pulse height spectra from the diode in the pile coupled to the Amptek preamp. The spectra are of higher resolution than with the ORTEC preamp and show two energy peaks.

The experiment was modeled using MCNP5 in order to determine the differential neutron flux at the diode with and without the Cd covering. The code can be found in Appendix E. Fig. 48 shows the geometry of the model and the results. The Cd shielding decreased the thermal neutron population as expected. The total number of neutrons that the diode could detect depends on the point at which the reaction no longer occurs, i.e.

when the cross section is too low. The reaction was assumed to occur if the cross section was at least 1% of the thermal neutron cross-section of 46000b.

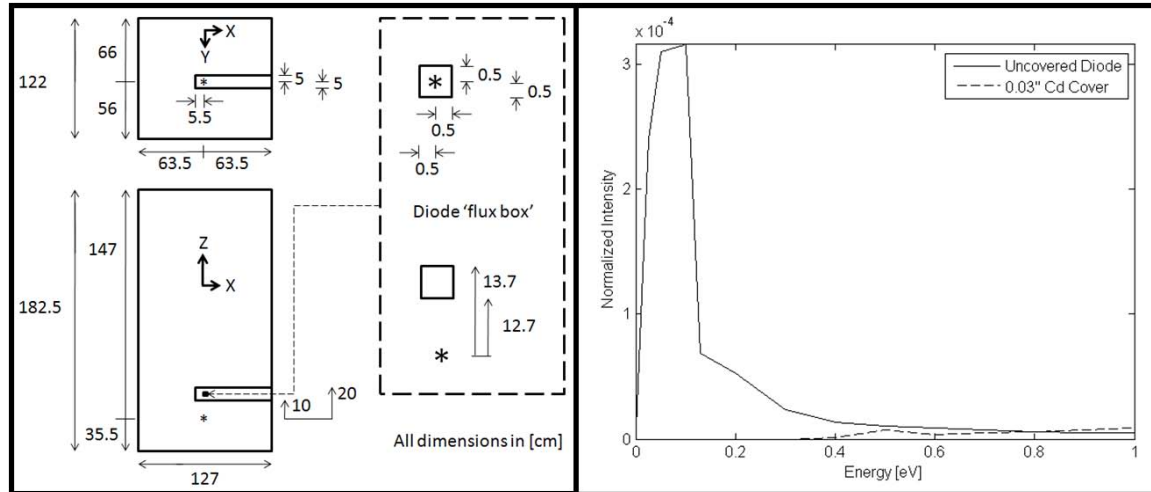


Fig. 48 The geometry of the MCNP5 model of the diode in the pile (LEFT) and the resulting neutron differential flux at the diode (RIGHT). The model results show that Cd absorbs the low energy neutrons as expected and the thermal neutron population is greatly reduced compared to the unshielded population.

Shown in Fig. 49, the 1% point is achieved for neutrons with an energy less than 0.13 eV.

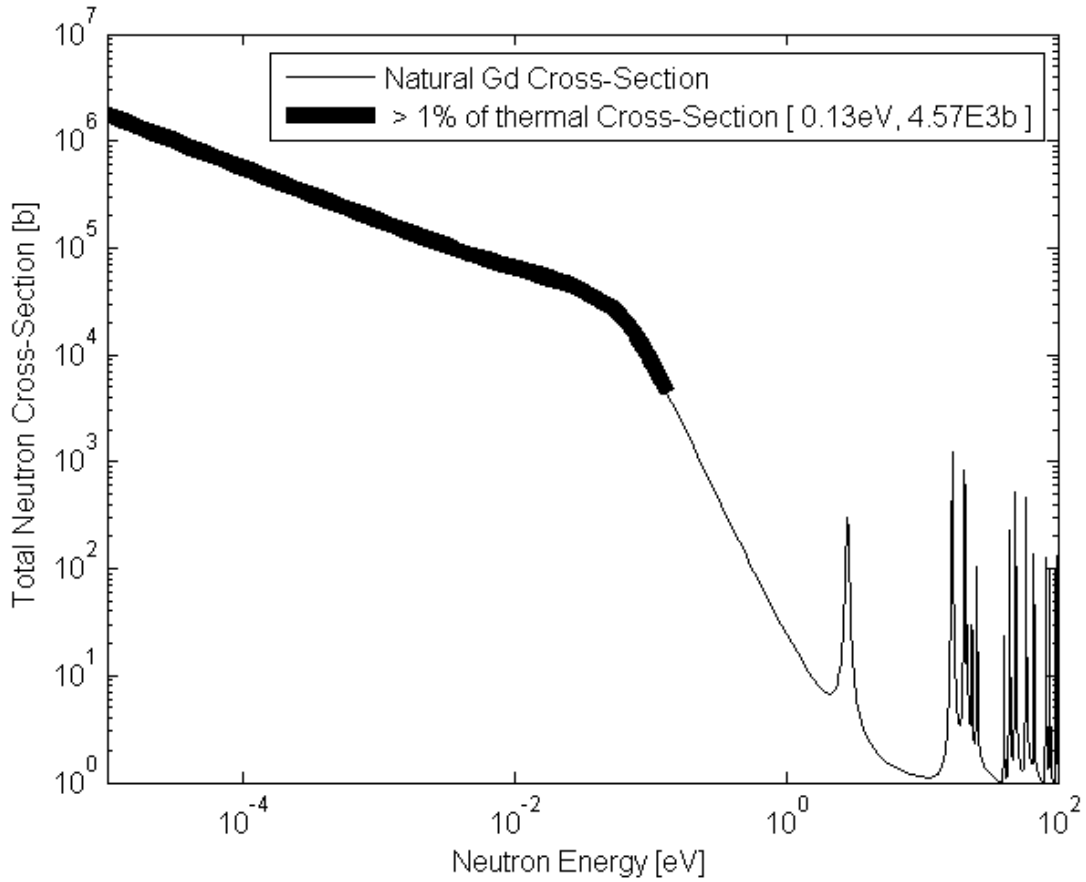


Fig. 49 The total neutron cross-section for naturally abundant Gd. The cross-section is greater than 1% of 46000 b, the thermal energy cross section, for all energies greater than 0.13 eV.

Using the results of the MCNP5 model, the probability per source neutron (PPSN) for energies up to 0.13 eV is 9.349×10^{-4} in a 1 cm^3 volume. PPSN is the output of the energy tally from the MCNP model and is the probability of a single source neutron populating a specified energy bin in the tally. Multiplying the PPSN by the current neutron activity of $1.14 \times 10^7 \text{ n/s}$, the 3600s counting period, and the active volume of the diode yields a total of 8.49×10^5 neutrons that could be detected by the diode. Assuming 100% diode efficiency, this value is still 3 orders of magnitude below the integrated

energy peak of the uncovered sample. With a Cd cover, the MCNP5 model shows no significant neutron population below 0.3 eV.

The diode signal was not due solely to neutron interaction. It was likely that the signal was from gamma ray interaction in the diode or potentially a combination of the two.

It was assumed initially that the diodes were gamma insensitive. The wafer on which the diode samples were prepared is less than 550 μm thick with the active region of the diode less than 16 μm thick. Fig. 50 shows the diode dimensions as it was modeled in MCNP5. A plot of I/I_0 using the thin beam model of photon attenuation is listed as Fig. 51 using the dimensions of Fig. 50.

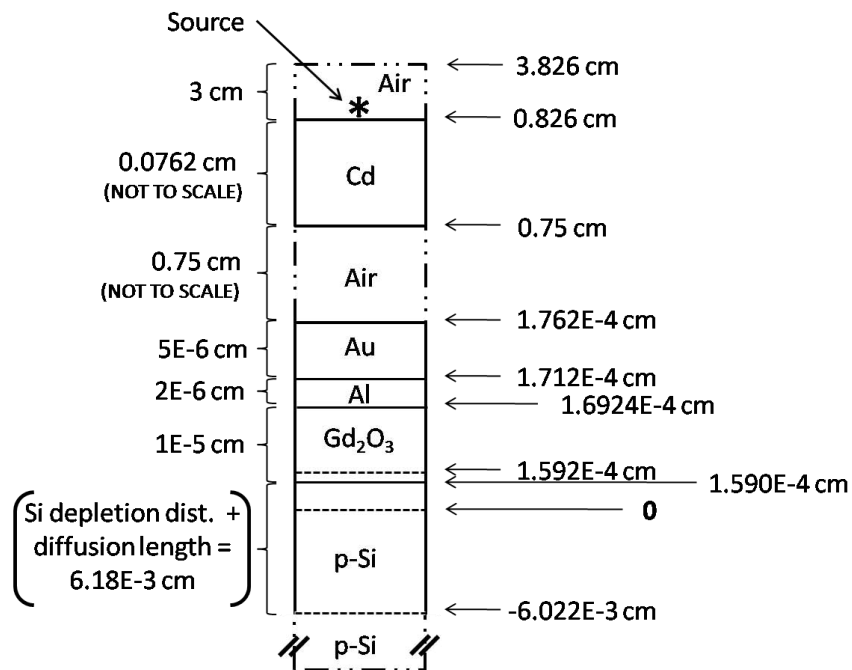


Fig. 50 A dimensional drawing of the diode as modeled in MCNP5.

If the active region of the diode is only the depletion region, the device is insensitive to photons with energies greater than 3 keV as shown in Fig. 51. If the charge, however, is collected over a greater distance such as the sum of the depletion and diffusion length in the Si, then the device is sensitive to photons up to 8 keV, also shown in Fig. 51. Low energy gamma rays could potentially deposit energy in the diode. If the Cd cover down-scattered the gamma spectrum, it would provide an explanation for the larger feature. An experiment was conducted to measure the gamma spectrum at the diode location in the pile using a LaBr scintillator. Lead and cadmium covers of the same thickness as used on the diode were constructed to cover the scintillator.

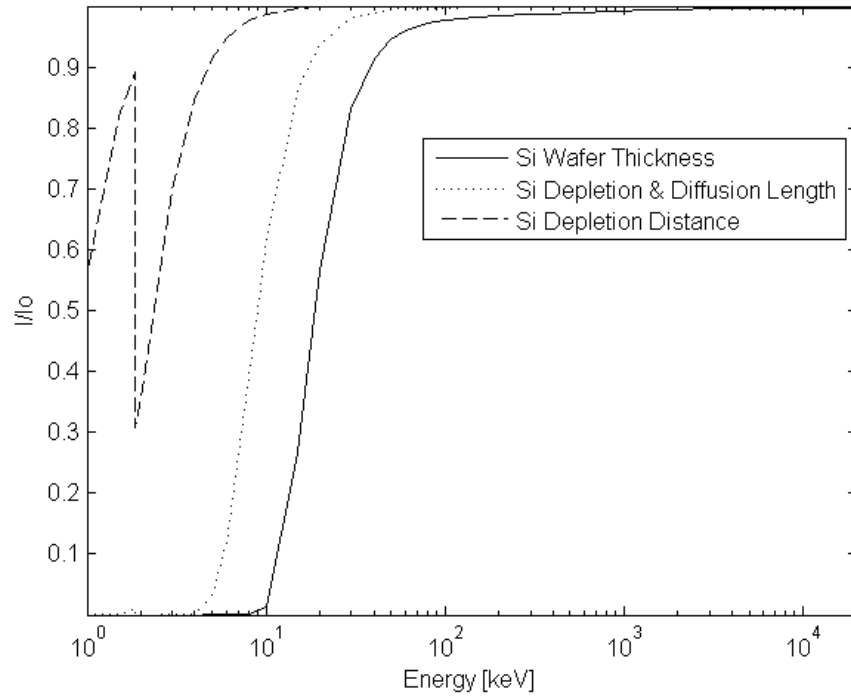


Fig. 51 A comparison of initial and final photon intensity in the narrow beam model for different thicknesses of Si in various regions of the diode. The initial photon intensity is I_0 , the final intensity is I . The thicker the Si, the lower the value of I/I_0 which implies insensitivity at that energy. The thicknesses used are 550×10^{-4} , 6.18×10^{-3} , and 1.59×10^{-4} cm corresponding to the wafer thickness, depletion plus diffusion length, and the depletion length. The spike in I/I_0 is due to a K shell energy level at 1.83 keV.

Pulse height spectra were recorded with and without the different covers as depicted in Fig. 52 and Fig. 53. The covers fit over the entire crystal as well as a portion of the PMT.

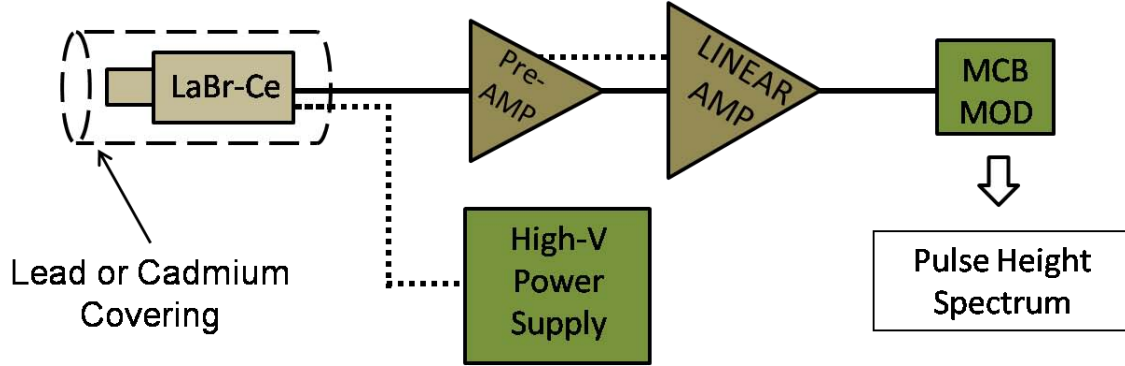


Fig. 52 The instrument diagram used for the gamma spectrum measurement.

An energy calibration was performed using a Co-60 source and 5 characteristic peaks of the PuBe photon spectrum [26]. It was found that a 4th order polynomial, (46), provided an appropriate fit.

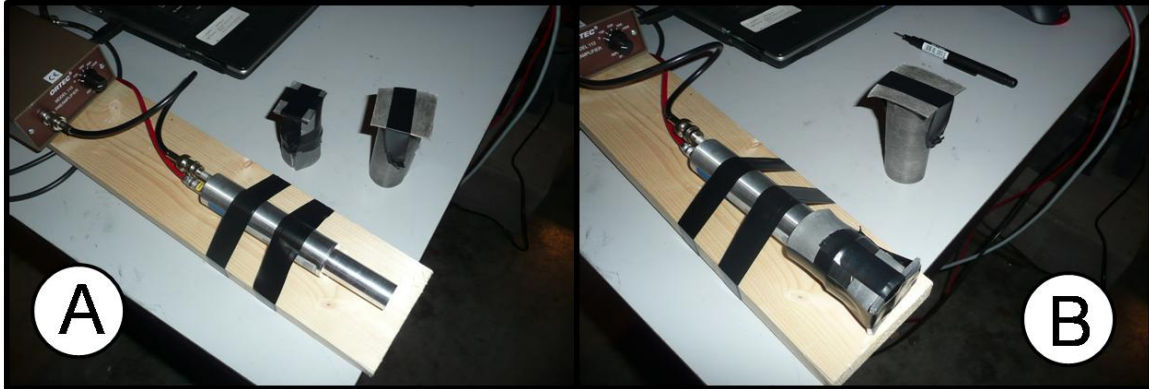


Fig. 53 The LaBr scintillator was mounted to a board which was placed into the pile. This allowed the detector to be replaced in the same location each time it was removed. The detector was placed into the pile without any covering 'A' and with both Lead and Cadmium shields both of which are shown in 'B'.

$$E(Ch) = -1 \times 10^{-10}(Ch)^4 + 3 \times 10^{-7}(Ch)^3 + 1 \times 10^{-4}(Ch)^2 + 0.2787(Ch) + 7.2093 \quad (46)$$

The results, depicted graphically in Fig. 54, show that the shielding materials did soften the gamma ray spectrum. Since lower energy photons have a higher probability of interaction, this provides a reason for the experimental result but only in the energy region below 20 keV. Lead was observed to significantly down-scatter the spectrum and provide a dominant peak centered around 36 keV. Since this feature was not strongly observed in the diode spectrum, it is probable that photons of this higher energy are less likely to interact in the diode.

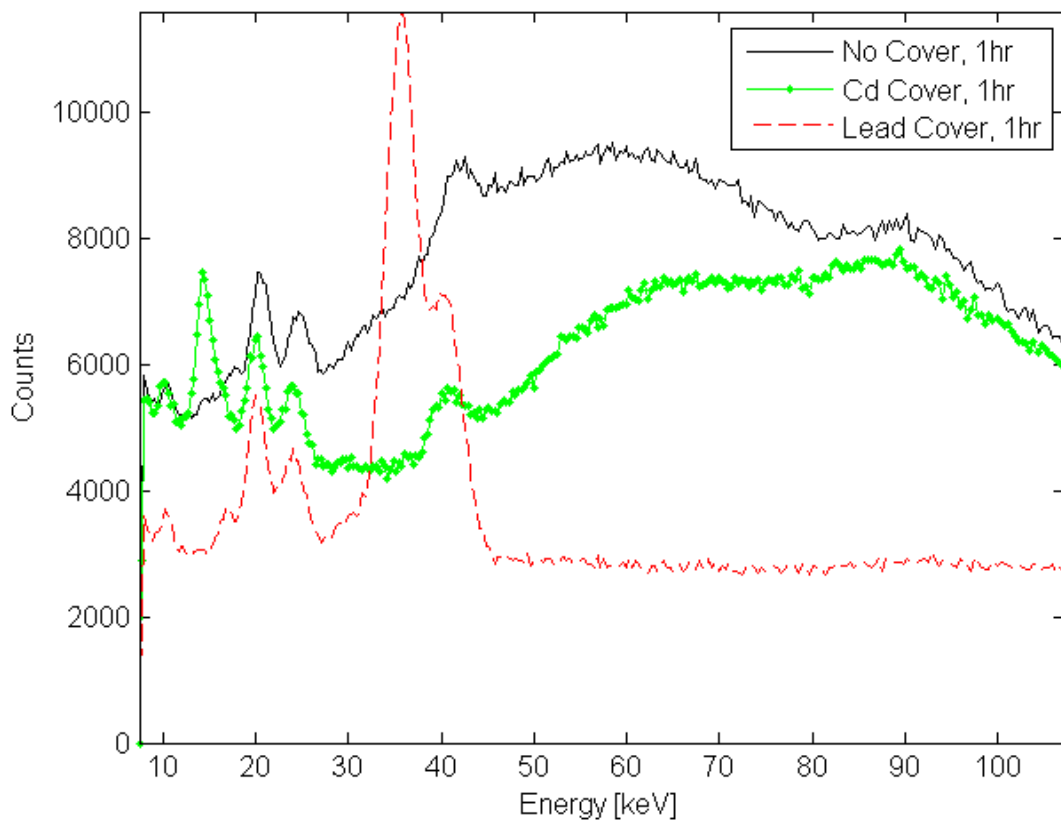


Fig. 54 Pulse height spectra data taken with a LaBr detector inside the graphite pile at the diode location. The presence of shielding material softens the spectra.

A quantitative link between the diode response and the photon spectra was developed using a simple absorbance model. Fig. 55 depicts the observed diode spectrum peaks with the corresponding gamma ray peaks for the same shield configurations.

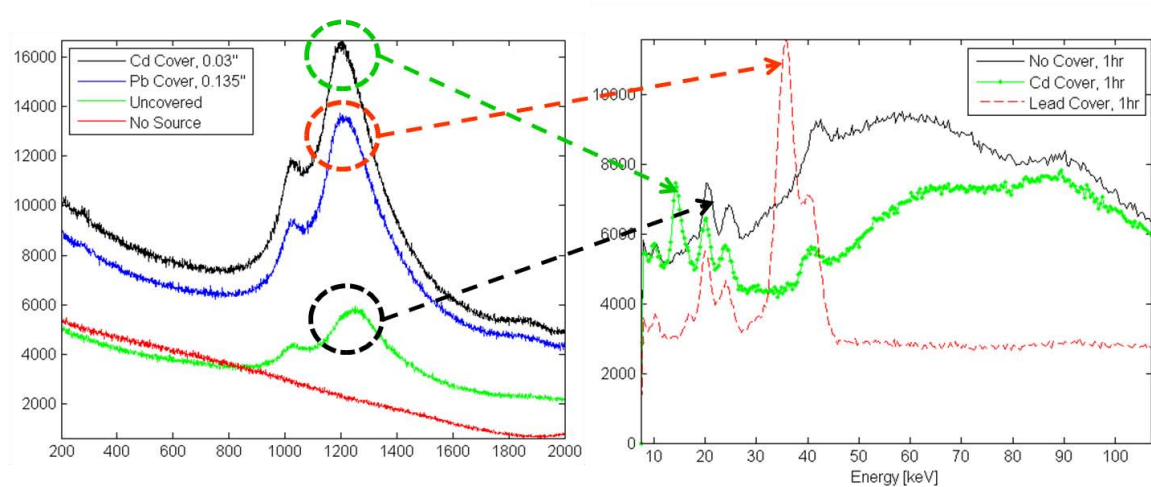


Fig. 55 The PHS from the diode (left) and the PHS from the LaBr detector (right). The arrows show the relationship between the diode response and the gamma ray energy that produced it.

The diode peak centroids are nearly at the same energy because only those electrons liberated in the sensitive diode region are collected as a pulse. A photon that continues to deposit energy as ionization beyond the diffusion length of an electron does not contribute further to the signal. Thus, within a narrow range of photon energies, all photons deposit nearly the same energy in the diode. The amplitude of the diode response increased with the number of photons that interacted. Less energetic photons are more likely to interact than those of high energy. Qualitatively, the Cd shielding produced a number of 15 keV photons which were more likely to interact in the diode than the greater number of 36 keV photons produced by the Pb shielding.

Integrating the spectral peaks from both detectors and applying the calculated absorbance to the LaBr peaks quantitatively corroborates the relationship. The energy dependent absorbance fraction can be calculated using (47). The ratio of photons absorbed to photons incident, or absorbance fraction, is represented by I_a/I_o . The mass energy absorption coefficient is represented by μ_{en} . The material density is ρ and the thickness of the absorbing material is t .

$$\frac{I_a}{I_o} = 1 - e^{-\frac{\mu_{en}}{\rho} \rho(t)} \quad (47)$$

The absorbance fraction for 60 μ m of Si was computed at the energies corresponding to the centroids of the photon spectra experimentally determined using the LaBr detector. Table XI summarizes the result of the calculation.

TABLE XI The computed absorbance fraction of gamma rays in silicon.

Energy [keV]	μ_{en}/ρ [cm ² /g]	I_a/I_o
15	9.79	0.128
22	3.49	0.048
36	0.750	0.010
ρ Si = 2.33 g/cm ³ , thickness Si = 60 μ m		

A plot of the integrated peaks against their centroid energies for both the diode and scintillator spectra is shown as Fig. 56. The diode peaks were recorded at nearly identical energies but the integrated diode peaks (plotted as squares) are displayed at the energy of the most probable photon energy using the relations shown in Fig. 55.

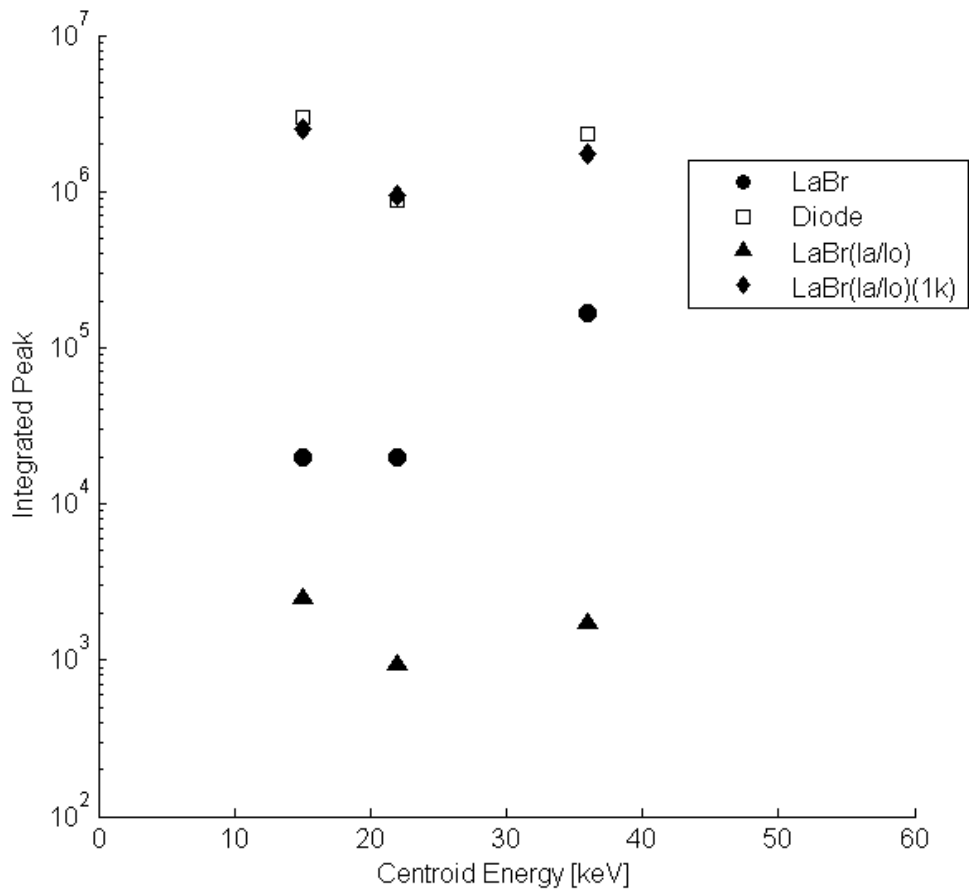


Fig. 56 The diode response explained by the energy deposition by gamma ray photons.

The total number of counts under the peaks at the centroid peak energies of the LaBr spectra are plotted as circles. The peak at 15 keV was observed, or produced by, the presence of the Cd shield. The peak at 36 keV was observed when the Pb shield was used. The 22 keV peak was observed when the diode was un-shielded. Multiplying the absorbance fractions at each energy to the LaBr peaks scales the peaks for absorbance probability. This is plotted as triangles. The integrated diode peaks exhibit the same relative relationship as the absorbance adjusted LaBr peaks. This is more clearly shown when the absorbance adjusted LaBr peaks are scaled by 1000 and plotted as diamonds

which nearly overlap the diode peaks. This provides more evidence that the diode was responding to gamma rays.

MCNP5 was used to model the energy deposited in the diode from the PuBe gamma spectrum with and without the Cd shielding. The MCNP5 input files are in Appendix I. Fig. 57 depicts the modeled PuBe gamma spectrum and Fig. 58 graphically depicts the energy deposition in the modeled diode from the gamma spectrum.

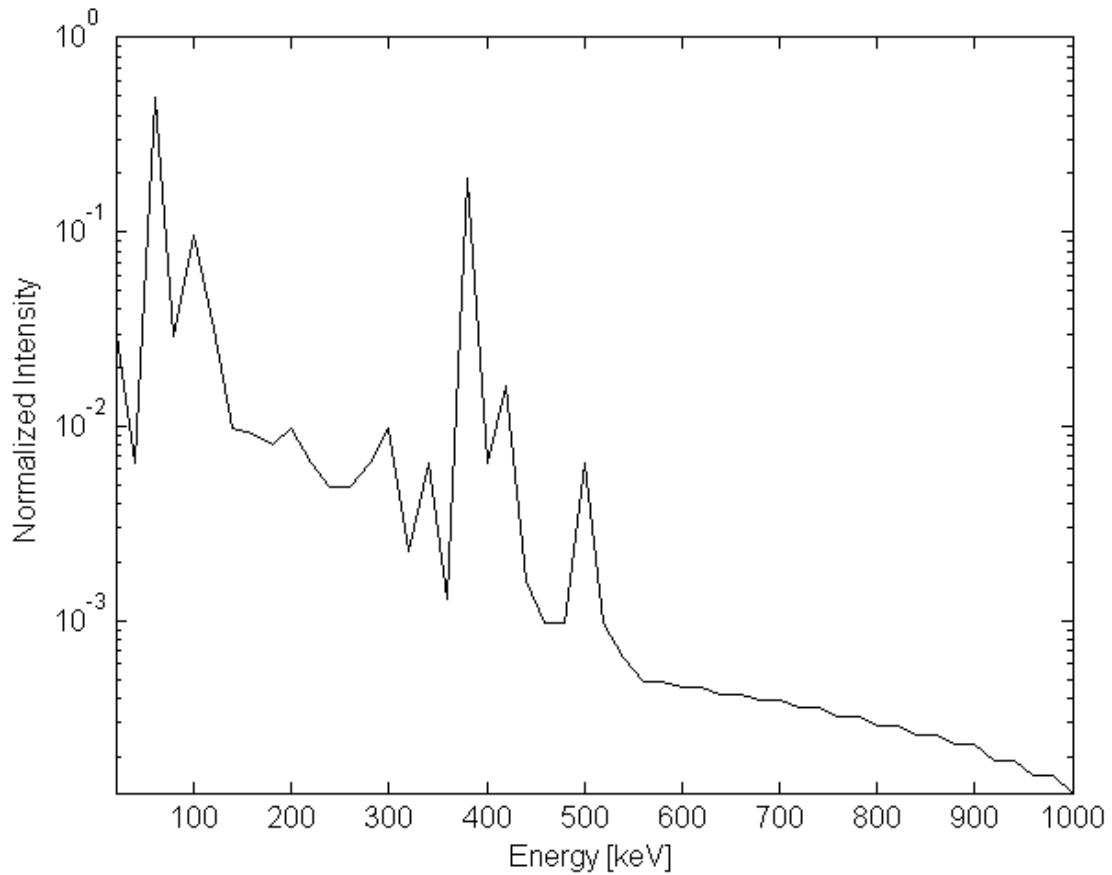


Fig. 57 The photon energy spectrum of the PuBe source used for MCNP simulation. The spectrum was developed from published data taken with a high-purity Germanium detector [26].

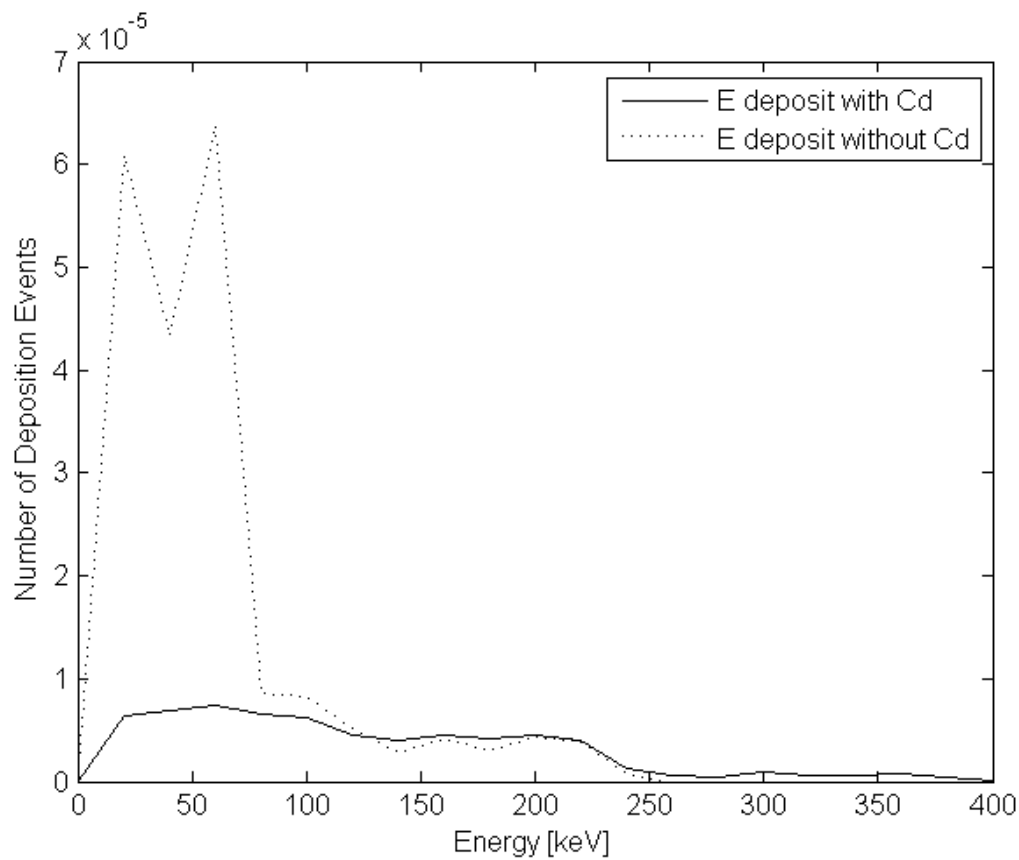


Fig. 58 The deposition of energy in the diode from a PuBe photon spectrum as deposited in Si over an electron diffusion length from the metallurgical junction. The model does not agree with the hypothesis that more energy is deposited in the device when a Cd cover increases the low-energy photon population.

The model produced unexpected results and predicts that more energy is deposited when the Cd cover is not present. The experimental data clearly shows a larger diode response when Cd-shielded. The LaBr detector also had a stronger response at low energies when Cd-shielded. The experimental data and the model do not agree indicating that the model may not accurately represent the physical system. A likely cause of the disagreement may be the coarsely modeled PuBe photon spectrum. A high resolution spectrum may be needed to accurately model the scattering interactions.

It was concluded that the diode produced a signal in response to the gamma ray fluence. It is possible that an indistinguishable neutron signal was present but this could not be confirmed.

4.6 Sr-90 Experiment

The mechanism by which the neutron capture produces a signal in the diode is the ionization of atoms in the material by internal conversion electrons. This process liberates electrons which then are collected as charge in the active diode region. An experiment was conducted using a Strontium-90 source as an external supply of electrons in order to verify that the charge collection process of the diode functioned. Sr-90 has a half life of 28.79 years and decays by emission of a beta particle. It is a pure beta emitter with an end point energy of 546 keV providing an average particle energy of 195.8 keV [28]. The daughter product is Yttrium-90 which has a half-life of 64.1 hours. Y-90 decays through beta emission with an end point energy of 2280.1 keV providing an average particle of 933.7 keV for 99.9885% of decays [28]. It also emits a less intense beta particle with an end point energy of 519.4 keV which has an average energy of 185.6 keV for 0.0115% of decays. The Y-90 nucleus decays to a stable Zr-90 nucleus [28]. Fig. 59 graphically depicts the decay of both Sr-90 and Y-90.

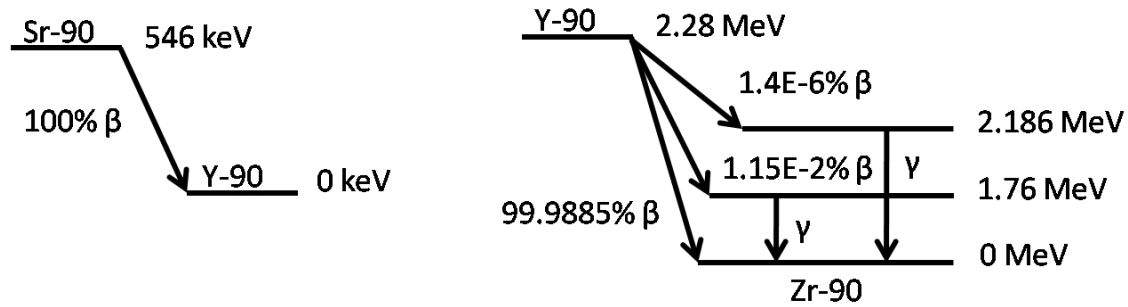


Fig. 59 The decay schemes for Sr-90 and Y-90.

The Sr-90 source was produced originally as a medical device in 1951. This legacy source has not been fully characterized for laboratory use. The activity and containment geometry of the Sr-90 are not precisely known. Table XII summarizes the parameters of the source used for calculation [29].

TABLE XII The parameters of AFIT source number 00365, the Sr-90 eye applicator.

Parameter	Value
Manufacturer	Tracerlab
Initial Activity, 28 Feb. 1951	25mCi
Activity in Dec. 2009	6mCi
Active Source Diameter	5mm
Source Containment Dia.	12.7mm
Protective Shield Diameter	4 inch
Protective Shield Thickness	3/8 inch
Overall Length of Assembly	6.75 inch
Aluminum Source 'Window'	10 mils
S. Steel Source 'Window'	2 mils

Because the beta particle shares its energy with the anti-neutrino, the emitted beta energies follow a distribution out to the maximum, or end point energy. This distribution can be represented by (48) where T_e is the kinetic energy of the beta particle, m_e is the

rest mass of the beta particle, c is the speed of light in a vacuum, and Q is the end point energy [15].

$$N(T_e) = \frac{C}{c^5} (T_e^2 + 2T_e m_e c^2)^{\frac{1}{2}} (Q - T_e)^2 (T_e + m_e c^2) \quad (48)$$

The constant ‘ C ’ represents a number of parameters including the nuclear matrix element which were taken as unity. Since the Sr-90 and Y-90 are in transient equilibrium, it can be assumed that every Sr-90 decay will be immediately followed by a Y-90 decay since the scale of their half-lives are different by nearly 4 orders of magnitude. The emitted beta spectrum is a combination of the two distributions modeled by (48) shown in Fig. 60. Because they are both normalized, the distributions are scaled appropriately for comparison.

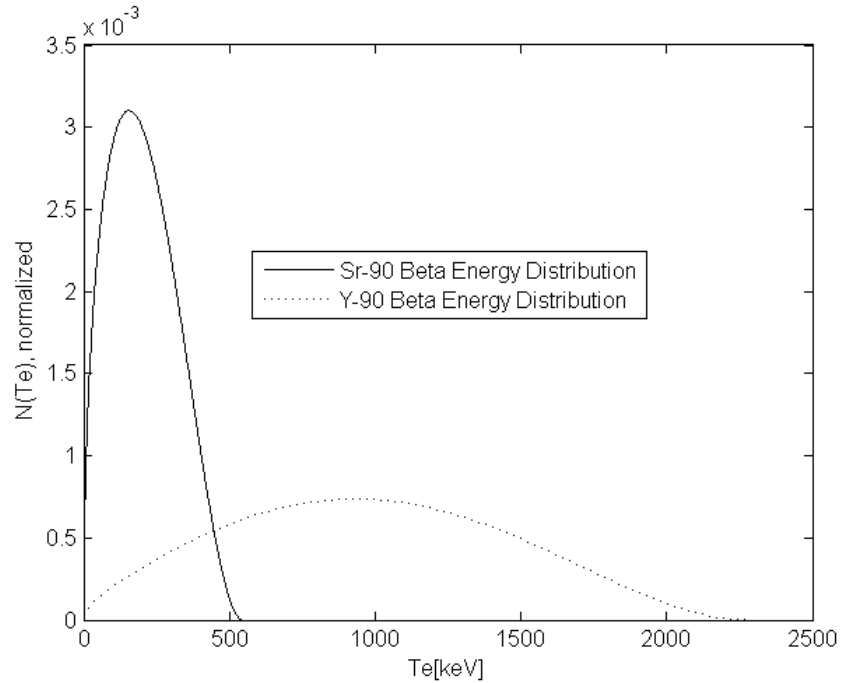


Fig. 60 The overlapping beta-particle energy distributions of Sr-90 and Y-90.

The source is housed in a stainless steel and aluminum body as pictured in Fig. 61. The beta particles that provide a signal must escape the source housing, pass through the air, the inactive layers of the diode, and finally interact in the active region. For the average beta energies of 195.8 and 933.7 keV, the linear stopping power approximation shows that a large fraction of the beta particles do not escape the source housing. Table XIII summarizes the stopping power data.

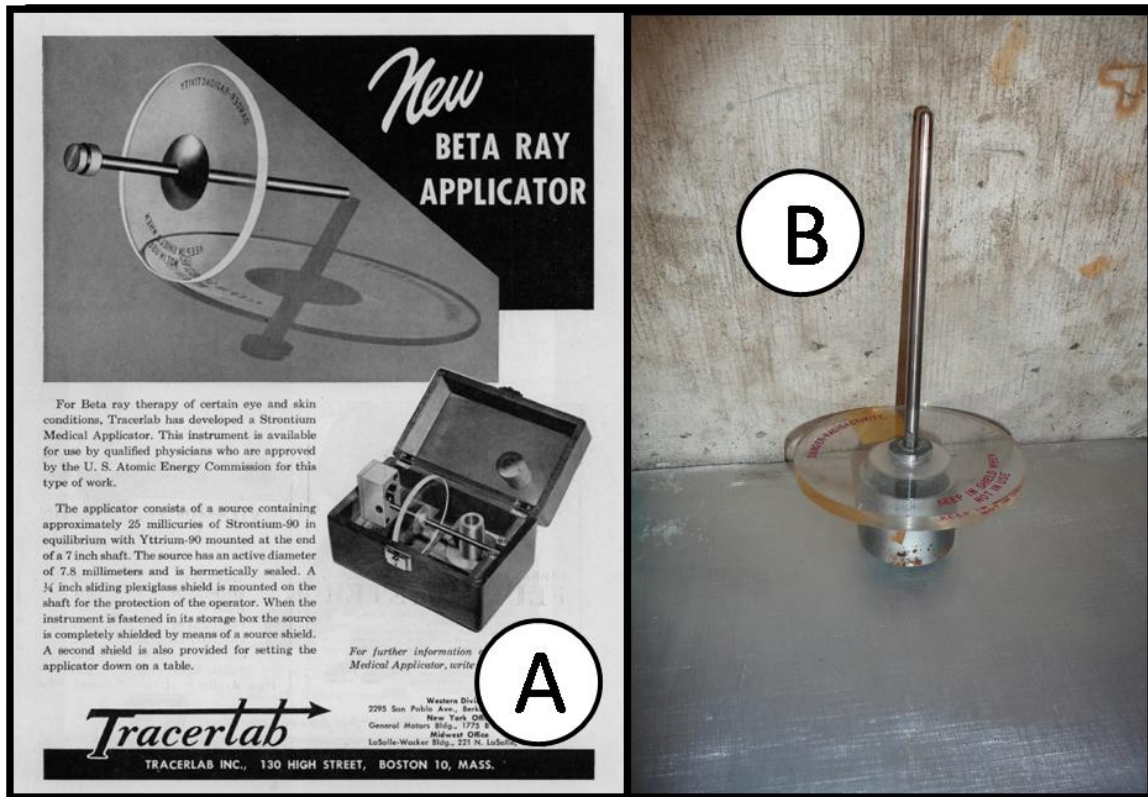


Fig. 61 The Sr-90 source was originally produced as a medical applicator shown in 'A'. The source, pictured in 'B' has a plastic shield that slides up and down the shaft which is designed to shield the operator from radiation. The source is sitting head-down and is covered by a thick aluminum shield for storage which is removed for use. The Sr-90 is enclosed in a stainless steel and aluminum element on the end of the applicator rod.

TABLE XIII The linear stopping power of the Sr-90 source housing.

	Stainless Steel	Aluminum
Thickness [cm]	0.00508	0.0254
ρ [g/cm ³]	8	2.7
Stopping Power for 195.8 keV [keV cm ² /g]	1947	2183
Stopping power for 933.7 keV [keV cm ² /g]	1354	1492
Energy absorbed at 195.8 keV [keV]	79	150
Total [keV]	229	
Energy absorbed at 933.7 keV [keV]	55	102
Total [keV]	157	

Table XIII shows that nearly all of the particles emitted by Sr-90 are contained within the source housing since energies up to 229 keV will be stopped by a combination of the steel and aluminum ‘window’ of the housing. A fraction of the Y-90 beta particles will also be stopped. The stopping power is energy dependent. The threshold of particle absorption listed in Table XII is based upon the average particle energy. A multi-group approach would produce a better approximation for the escaping beta particle energies. The energy distribution of the emitted beta particles is shown in Fig. 62. The source beta particle distribution is nearly all from Y-90, a statement corroborated by others using similar sources [29]. Appendix H contains the MATLAB[®] code to calculate the fraction of emitted beta particles from each nuclide. Only 0.2 % of the Sr-90 emissions are passed through the source windows while 82.3% of the Y-90 particles escape.

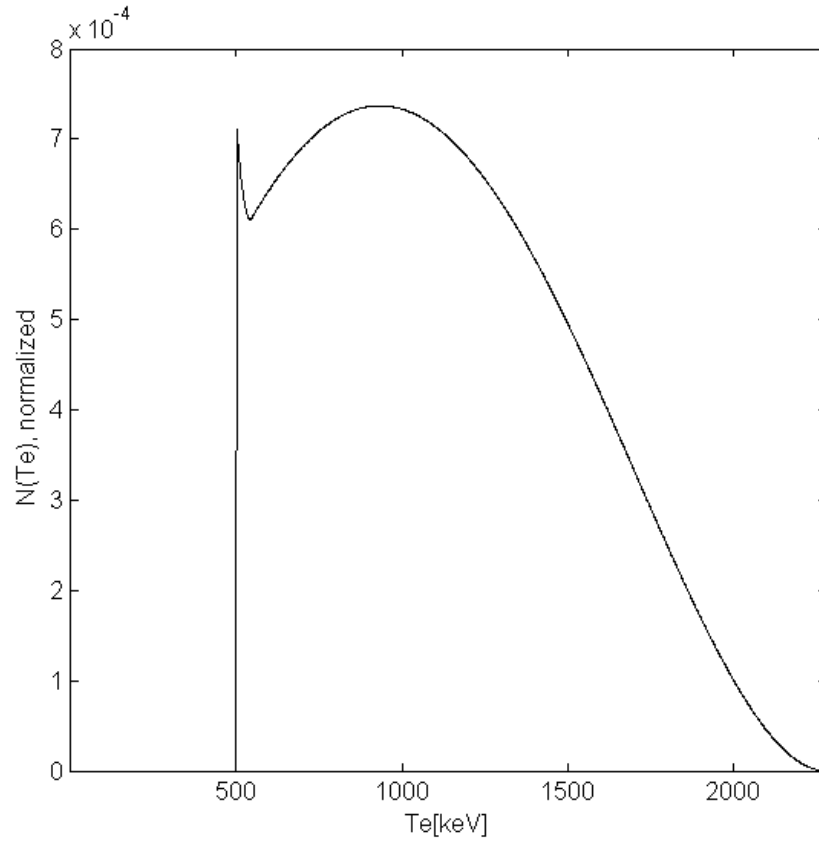


Fig. 62 The energy distribution of the beta particles emitted from the source.

The energy distribution is further altered by the interaction of the air and finally in the gold and aluminum which constitutes the contacts sputtered over the gadolima layer of the diode. After adjusting the distribution for these material interactions and multiplying it by source activity, it was integrated and subsequently divided by the spherical area provided by the source to diode distance as depicted in Fig. 63.

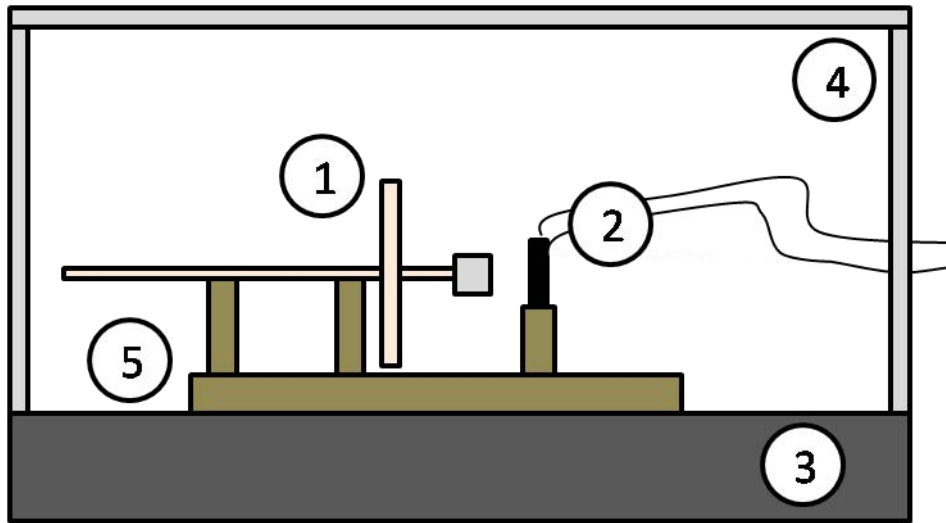


Fig. 63 A diagram of the Sr-90 experiment. Pictured inside aluminum shielding '4', are the diode and signal wires '2', the source '1', the concrete floor '3', and the source and sample stand '5'.

The diode was placed at 0.75" and 1.375" from the source. The flux was calculated to be 1.2×10^7 and 3.57×10^6 $\beta/\text{cm}^2 \text{ s}$ respectively. With the diode under bias using the same parameters as used in the graphite pile, pulse height spectra data was taken at each distance as well as a background when the source was removed from the laboratory. The result is shown graphically as Fig. 64. Subtracting the background and integrating provided 1.00×10^8 counts at 0.75" and 21.52×10^6 counts at 1.375". The counting period was 3600 seconds. The diode sample contained 5 diodes each with approximately $8.14 \times 10^{-12} \text{ cm}^2$ of surface area. The number of beta particle interactions that could be expected at 0.75" should be 1.75×10^{10} and at 1.375", 5.23×10^9 . Using these values, it was found that the diode efficiency for beta particles was 0.005 at 0.75", and 0.0041 at 1.375". Stated another way, the diodes only detected about 0.5 % of the beta particles. The low efficiency is partly due to the 2.001V low level discriminator setting used with the multi-channel buffer. This removed a large fraction of the diode signal but was used

to reduce dead time. Since the low energy channels of the spectrum contain the bulk of the counts as shown in Fig. 64, the actual efficiency may be greater by an order of magnitude or more. Qualitatively, the diode response followed the expectation of a higher signal with a higher flux close to the source and a weaker signal with a lower flux farther from the source.

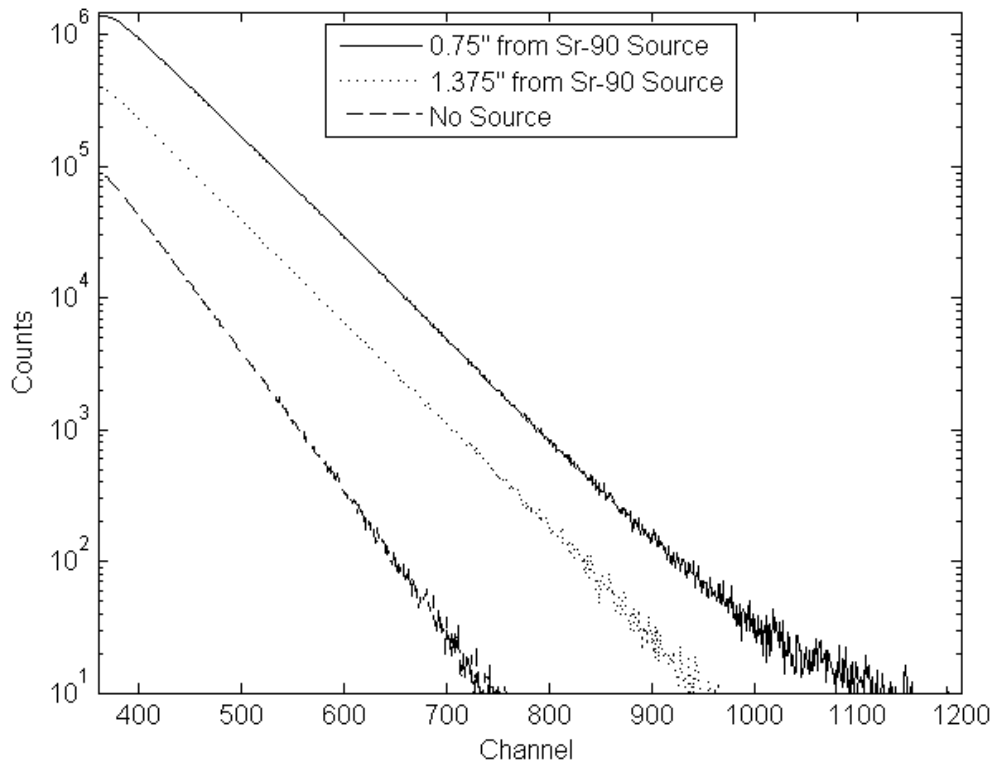


Fig. 64 The pulse height spectrum taken with the diode exposed to a beta source. The diode response was higher closer to the source.

The Sr-90 experiment provided evidence that electrons in the active region of the diode can produce a signal. The total number of gamma rays from the Y-90 decay that could have interacted with the diode was 6.5×10^4 at 0.75" and 1.9×10^4 at 1.375". This

small fraction of the source emissions does not account for the number of events recorded in the PHS. Although the diode is gamma sensitive, this experiment clearly showed that the response was due to the beta particle flux. The experiment does not, however, show the diode response to beta particles at the target energy of 79 keV. The Sr-90 source did not emit beta particles below 200 keV. Only a small fraction of down-scattered beta particles in this energy range would have interacted with the diode.

4.7 Cesium-137 Experiment

A 1.2 Ci Cs-137 source was used to find the diode response to a hard gamma flux. Cs-137 decays to barium-137 with a half-life of 30.04 years. 94.4% of the decays produce a beta particle with an average energy of 174.3 keV and an end point energy of 514 keV [28]. Beta emission is followed immediately by a gamma emission of 661.657 keV. Fig. 65 graphically depicts the decay process.

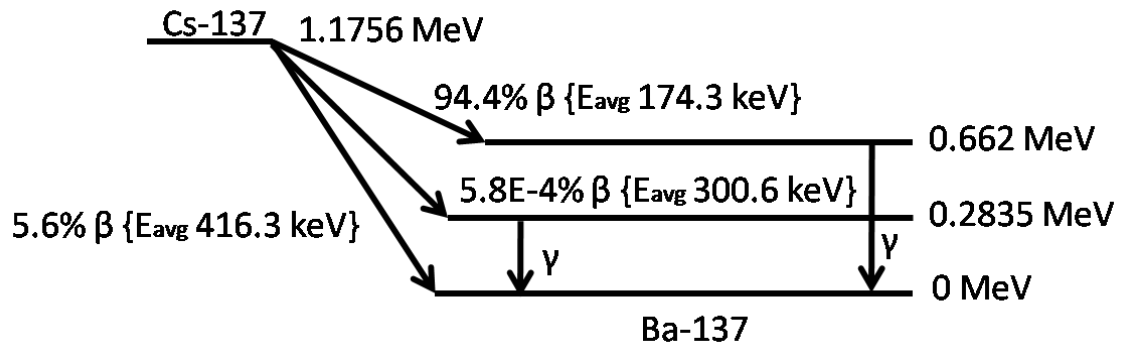


Fig. 65 The decay of Cs-137 to Ba-137.

The precise source activity during the experiment was 2.92×10^{10} Bq. The diode was placed 1.608" from the Cs-137 source as shown in Fig. 66. The solid angle was

0.00194 steradians as determined by using the total diode area for 5 active diodes at the stated distance. For a count duration of 6800 seconds, the number of 661.657 keV gamma rays impinging on the diode is 3.63×10^{11} . There is a fraction of beta particles as well with a maximum number of 2×10^{10} . The encapsulation of the Cs-137 comprises 3 layers of stainless steel totaling 0.12" of shielding. The fraction of beta particles emitted is near zero. The integration of the experimental pulse height spectrum of Fig. 67 yielded 1.2617×10^8 counts over a 6800 second period. The gamma efficiency computes to 0.035%.

The high dead-time experienced during measurement necessitated setting the LLD to 0.996 V in the MCB. This removed the energy events in the first 199 channels. Since the lower channels contain most of the counts, this is likely a contributor to the low efficiency of detection. However, it is likely that most of the gamma rays passed completely through the sample without interaction. Scattering of the spectrum by the containment vessel around the source as well as the sample itself may also have softened the spectrum.

The pronounced energy features observed in response to the PuBe source were not observed with the nearly mono-energetic 662 keV gamma ray source. It is possible to conclude that the diode is reasonably insensitive to gamma rays of 662 keV.

The original purpose of the Cs-137 experiment was to provide a diode response using instrument settings identical to an experiment conducted in the graphite pile. Because the PuBe source and Cs-137 have activities on the order of a Ci, the goal was to determine the contribution of the gamma spectrum to the total diode response. An

amplification shaping time constant of $0.5\ \mu\text{s}$ was used and not the $3\ \mu\text{s}$ constant found to be optimal for the ORTEC preamp.

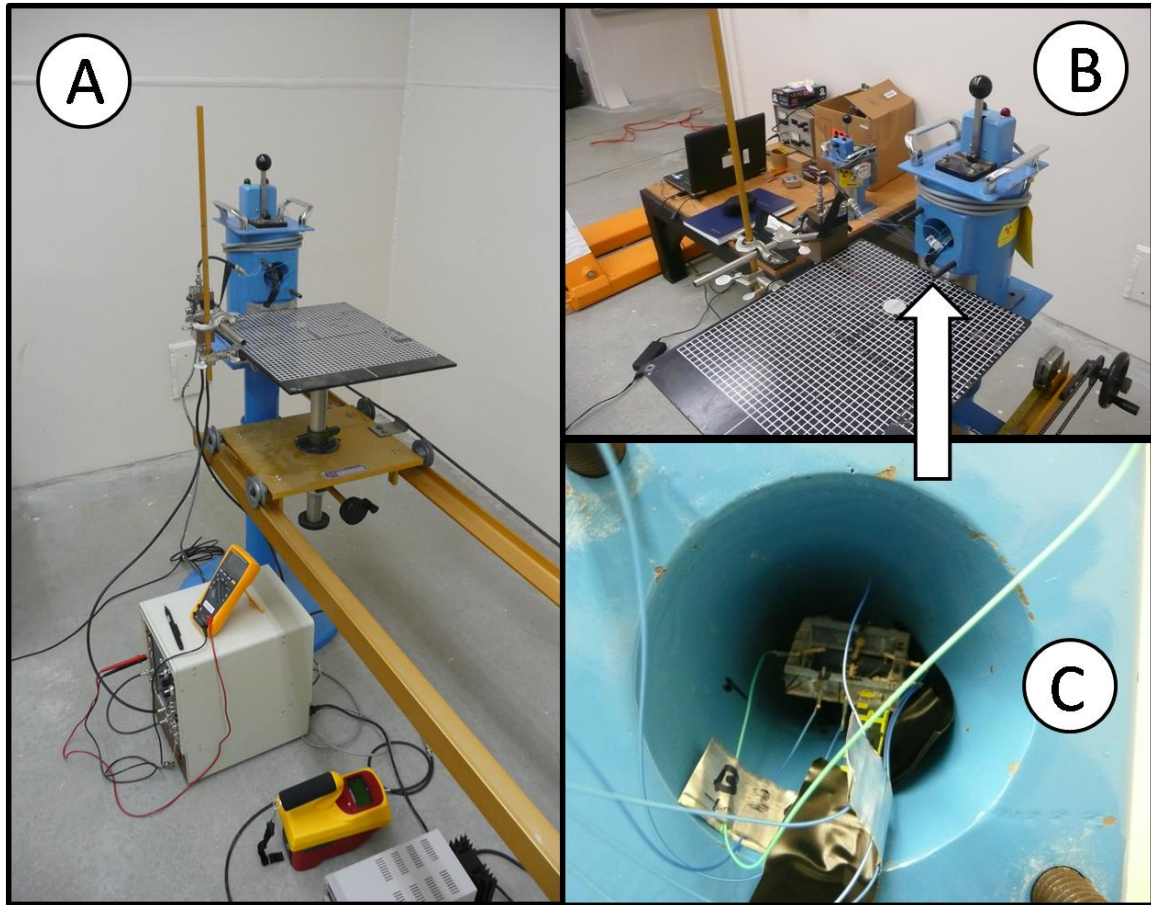


Fig. 66 The Cs-137 source belonged to AFFRAD and is used for calibrating instrumentation. The source is stored inside a containment vessel located at the end of a movable stand shown in ‘A’. The diode was placed 1.608” away from the exposed source. This distance was achieved by placing the diode inside the line-of-sight port of the pig as shown in ‘B’ and ‘C’. Close placement maximized the gamma flux.

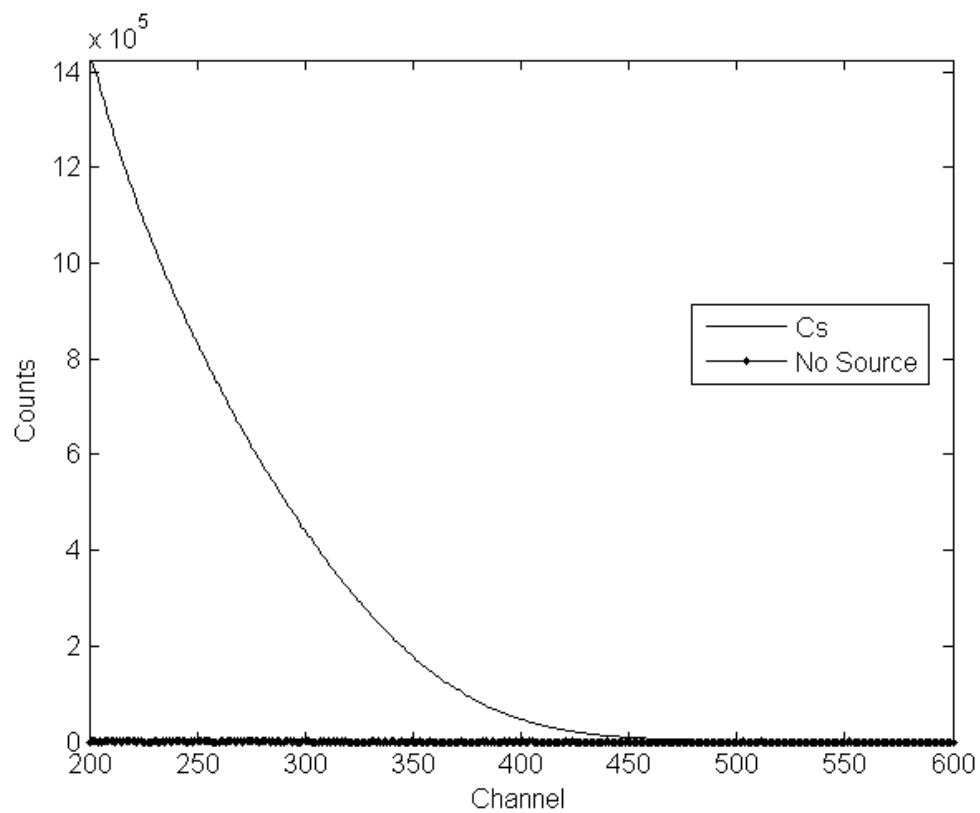


Fig. 67 The pulse height spectrum taken from the diode during irradiation from the 1.2 Ci Cs-137 source.

V. CONCLUSIONS

5.1 Conclusions

No direct evidence of neutron detection was observed during the course of experimentation. Under the experimental conditions, neutron interactions undoubtedly occurred in the diode. However, the presence of a relatively high leakage current and the gamma ray sensitivity of the novel diode produced a signal that may have masked the presence of neutron interaction.

Experimentation supports the following statements:

1. The best diodes prepared using the supercritical water deposition process have leakage currents on the order of tens of micro-Amps at a reverse bias of 1 volt. A typical commercially manufactured diode has a leakage current of pico-amps. The novel diodes are relatively leaky.
2. The diode is capable of collecting charge from ionization produced by energetic electrons in the active region. This was observed as the diode response to the Sr-90 beta particle flux.
3. The diodes are sensitive to low energy gamma rays. It is likely that the energy region in which this was observed was between 10 and 20 keV.

It is not possible to make a complete determination as to the feasibility of a $\text{Gd}_2\text{O}_3/\text{Si}$ diode for neutron detection based on the experimental data. As the process for diode fabrication improves and devices with lower leakage currents become available, the potential as a neutron detector increases. However, the discovery that the diode is gamma sensitive is problematic for neutron detection unless a way is found, by spectroscopy or design, to specifically measure the conversion electron energy.

5.2 Recommendations for future work

5.2.1 Investigate the photon sensitivity.

It was determined that the diode was gamma sensitive. The diverse photon spectrum of the PuBe source is not optimum for determining the specific energy range over which the diode is sensitive. The use of multiple, mono-energetic gamma ray sources would provide a means to determine specific sensitivity. A high-order response to specific energies may yield information as to the region of the diode where the charge is being collected. The double-peak feature of the diode response to low energy gamma-rays may be caused by energy deposition in multiple regions of the diode with differing mobilities.

5.2.2 Calibrate the diode spectrum.

The diode signal is uncalibrated. The resulting PHS may or may not include the region of energies in the 79 keV range. A diode response to several energies of

monoenergetic electrons will determine the optimal instrumentation settings for neutron pulse detection.

5.2.3 Diode modeling.

A more rigorous model of the diode using DaVinci[®] or similar semi-conductor device modeling software package can be produced to determine the character of the heterojunction [36]. It is possible that the active region of the diode is completely infused with Gd₂O₃ due to the high-energy deposition process which would change the depletion characteristics. The diode is currently modeled as an abrupt heterojunction which may not be accurate.

A more rigorous MCNP modeling effort for gamma ray energy deposition may provide the range of energy sensitivity and support an engineered solution to detecting neutrons. Enhanced modeling may provide insight into where the energy is deposited in the Gd / Si system.

APPENDICES

Appendix A: Diode Active Volume and Coincident Counting Time

Variables

```

| Gd2O3 : 7.41 | : g / cm3 : | ;
| Si : 2.33 | : g / cm3 : | ;
AvogadroNum : 6.02*^23;
MolWtGd2O3 : 352 | : g / mole Gd2O3 : | ;
q : 1.602*^-19 | : C : | ;
VbuiltIn : 0.15 | : V : | ;
Vapplied : 1.5 | : V : | ;
NA : 5*^19 | : 1 / cm3 : | ;
ND : 1*^15 | : 1 / cm3 : | ;
kGd2O3 : 17;
kSi : 11.9;
| not : 8.85*^-14 | : F / cm : | ;
| : 46000*^-24 | : cm^2 : | ;
ContactDiameternm : 814000 | : nm : | ;
ContactDiametercm : 814000*^-7 | : cm : | ;
| : 500 | : thermal neutrons / cm2 s : | ;
LaBrCrystalDiam : 0.18 | : cm, measured : | ;
StandOffClose : 0.1 | : cm : | ;
StandOffFar : .75 | : cm : | ;
CountGoal : 100 | : neutron capture count goal : | ;

```

Calculate the Depletion Width, W, as an abrupt Heterojunction

```

Assuming | Xp > 0 && Xn > 0, Solve | { Xp NA q : Xn ND q,  $\frac{NA q Xp^2}{2 kSi | not}$ ,  $\frac{Xn^2 ND q}{2 kGd2O3 | not}$  : : ( VbuiltIn + Vap
| { Xp, Xn } |
| { Xp + 3.18471 | 10^-9, Xn + 0.000159236 |, { Xp + 3.18471 | 10^-9, Xn + 0.000159236 | }

```

! Must update this from the above calculation !

```

Xp :: 3.184714562745104`*^-9 ; Xn :: 0.0001592357281372552` ;

```

```

Wcm : Xp + Xn | : depletion width in | cm | : |

```

```

0.000159239

```

```

Wnm : 10 000 000 Wcm | : depletion width in | nm | : |

```

```

1592.39

```

Calculate Active Gd nucleus density

```

NactiveGd :  $\frac{AvogadroNum | Gd2O3}{MolWtGd2O3}$  | :  $\frac{2}{1}$  | : Gd atoms / cm3 : |

```

```

2.53456 | 10^22

```

```

BigSigma : NactiveGd | : macroscopic x section, | 1 / cm | : |

```

```

1165.9

```

```

ActiveGdVolume :  $\frac{| ContactDiametercm |^2}{4}$  | : Xn | : cm3 : | : 5 | : all 5 diodes at once : |

```

```

4.14333 | 10^-6

```

Number of Gd nuclei present in the Active Gd Volume

```

AbsNactiveGd : NactiveGd | : ActiveGdVolume

```

```

1.05015 | 10^17

```


Number of thermal neutron reactions in the device per second

```
NumThermNeutperSec : AbsNactiveGd | | | | | n| cm2 s| cm2| : | | s| | |
2.41534
```

Number of thermal neutron reactions in the device /s with coincident gamma 1107.6 keV

```
NumThermNeutperSecCoinc : NumThermNeutperSec | | 0.113| | | 0.136| | | 0.3| | | 0.5| | |
0.00556785
```

Calculate LaBr geometric efficiency (One crystal is closer than the other due to the sample preparation)

```
ThetaClose : ArcTan(| LaBrCrystalDiam| 2| | | StandOffClose| |
0.732815
```

```
ThetaFar : ArcTan(| LaBrCrystalDiam| 2| | | StandOffFar| |
0.119429
```

```
OhmegaClose : 2* | 1- Cos| ThetaClose| |
1.61293
```

```
OhmegaFar : 2* | 1- Cos| ThetaFar| |
0.0447561
```

```
GeometricFraction : | OhmegaClose+ OhmegaFar| | | 4* |
0.131915
```

Calculate Isotropic IC electron loss

```
IsoICElectronLoss : 0.25; | | qualitative estimate of what occurs w o full deposi
```

Counting time to obtain significant results:

```
CountEventpers : NumThermNeutperSecCoinc | GeometricFraction| IsoICElectronLoss |
0.00018362
```

```
TimeSec :  $\frac{\text{CountGoal}}{\text{CountEventpers}}$ 
```

```
544.603.
```

```
TimeHr : TimeSec | 3600
```

```
151.279
```

```
TimeDays : TimeHr | 24
```

```
6.30327
```

Appendix B: SNM Spontaneous Neutron Emission Rate Calculation

```

Pu239BR : 3* 10^ 12; ( | | / 100 | )

Pu240BR : 5.7* 10^ 8; ( | | / 100 | )

Pu241BR : 2* 10^ 14; ( | | / 100 | )

Pu239HL : 24110; ( | Y | )

Pu240HL : 6564; ( | Y | )

Pu241HL : 14.35; ( | Y | )

U235BR : 7* 10^ 9; ( | | / 100 | )

U238BR : 0.0000005; ( | | / 100 | )

U238HL : 4.468* 10^9; ( | Y | )

U235HL : 703800000; ( | Y | )

PuNperDecay : 2.89;

UNperDecay : 2.44;

PUInitialAmount : 100.; ( | 1.; ( | 1 gram | ) | )

UInitialAmount : 100.; ( | | ( | 1 gram | ) | )

NA : 6.02* 10^23;

YperS : 1/ 31536000; ( | year / second | )

ActivityPU239 : ( Log[ 2] / Pu239HL | PUInitialAmount | NA/ 239 | YperS; ( | decays per second for
ActivityPU240 : ( Log[ 2] / Pu240HL | PUInitialAmount | NA/ 240 | YperS; ( | decays per second for
ActivityPU241 : ( Log[ 2] / Pu241HL | PUInitialAmount | NA/ 241 | YperS; ( | decays per second for
ActivityU235 : ( Log[ 2] / U235HL | UInitialAmount | NA/ 235 | YperS; ( | decays per second for
ActivityU238 : ( Log[ 2] / U238HL | UInitialAmount | NA/ 238 | YperS; ( | decays per second for
NpersgPu239 : ActivityPU239 | Pu239BR | PuNperDecay | neutrons / | s | | g | for Pu239; |
1.99085

NpersgPu240 : ActivityPU240 | Pu240BR | PuNperDecay | neutrons / | s | | g | for Pu240; |
138359.

NpersgPu241 : ActivityPU241 | Pu241BR | PuNperDecay | neutrons / | s | | g | for Pu241; |
22.1144

NpersgU235 : ActivityU235 | U235BR | UNperDecay | neutrons / | s | | g | for U235; |
0.136643

NpersgU238 : ActivityU238 | U238BR | UNperDecay | neutrons / | s | | g | for U238; |
- - - - -

```

Appendix C: PuBe Source Neutron Emission Rate Calculation [30]

This worksheet was originally created by MAJ Spears in 2005. It was modified to make it applicable to the PuBe source in Dec of 2009.

The subscripts, 1,2,3, and 4, refer to Pu²³⁹, Pu²⁴⁰, Pu²⁴¹, and Am²⁴¹, respectively. The values for $a_{1,2,4}$ were taken from Fig.1 of the article Neutron Yields of Plutonium-Beryllium ((α, n) sources", Nuclear Applications, Vol 4, March 1968 by M. Edward Anderson.

```

Na :: 6.022 * 1023 | ,  $\frac{\text{atoms}}{\text{mol}}$  |
T1 :: 24110 | , half life in years |
T2 :: 6564 | , half life in years |
T3 :: 14.35 | half life in years |
T4 :: 432.2
| , half life in years |
Masstot :: 76.36 | grams |
W1 :: .934 | , composition of Pu239 |
W2 :: .061 | , composition of Pu240 |
W3 :: .0055
| , composition of Pu241 |

```

NOTE: The above % composition of the Plutonium was taken from Table III of the aforementioned article, "Increase in Neutron Yields of P Beryllium ((α, n) sources". I assumed the % composition of this source, M-1170, was similar to that of M-1127. No Am²⁴¹ is present at "birth

```

Mass1 : Masstot * W1 | g | ;
Mass2 : Masstot * W2 | g | ;
Mass3 : Masstot * W3 | g | ;

AM1 :: 239.052156 |  $\frac{\text{g}}{\text{mol}}$  |
AM2 :: 240.053808 |  $\frac{\text{g}}{\text{mol}}$  |
AM3 :: 241.0568453 |  $\frac{\text{g}}{\text{mol}}$  |

N1 :  $\frac{\text{Mass}_1}{\text{AM}_1}$  | Na ; | number of Pu239 atoms present initially |
N2 :  $\frac{\text{Mass}_2}{\text{AM}_2}$  | Na ; | number of Pu240 atoms present initially |
N3 :  $\frac{\text{Mass}_3}{\text{AM}_3}$  | Na ; | number of Pu241 atoms present initially |

| 1 :  $\frac{\text{Log } 2}{\text{T}_1}$  ; | decay constant |
| 2 :  $\frac{\text{Log } 2}{\text{T}_2}$  ;
| 3 :  $\frac{\text{Log } 2}{\text{T}_3}$  ;
| 4 :  $\frac{\text{Log } 2}{\text{T}_4}$  ;

```

The "birth date" of the source is approximately 4/25/61. The following equation solves for the initial neutron yield at the "birth date". Note: T elapsed from "birth date" to the date of measurement is 48.5 years.

```

a :: 9.04 * 106 | 3 * 106 |

```

$$Q_0 : Q_1 \left(1 + 1.23 \left(\frac{\lambda_4 \lambda_3 N_3}{\lambda_1 N_1 + \lambda_2 N_2 + \lambda_3 + \lambda_4} \left(\exp\left(-\lambda_4 \frac{318}{365}\right) + \exp\left(-\lambda_3 \frac{318}{365}\right) \right) \right) \right);$$

$$Q[t_] : Q_0 \left(1 + 1.23 \left(\frac{\lambda_4 \lambda_3 N_3}{\lambda_1 N_1 + \lambda_2 N_2 + \lambda_3 + \lambda_4} \left(\exp\left(-\lambda_4 t\right) + \exp\left(-\lambda_3 t\right) \right) \right) \right);$$

The above equation yields the activity of the source since its "birth" in 1962.

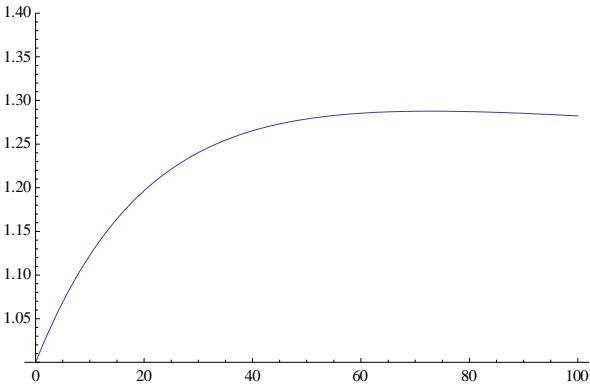
```
Date[] - { 1961, 6, 0, 0, 0, 0}
{ 48, 6, 2, 10, 11, 15.4000399}
```

```
Q[0] | { Neutron flux at birth |
8.92118 10^6
```

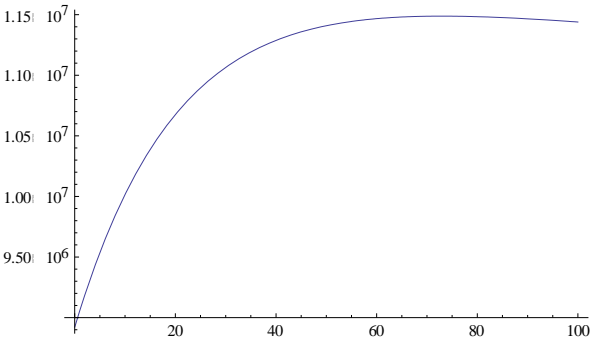
```
Q[48.5] | { 1961 to 2010 |
1.13956 10^7
```

This is the present flux [n/s] of neutrons emitted by the PuBe source

```
Plot[ Q[t]
      Q_0, { t, 0, 100}, PlotRange - { 1.0, 1.4}
```



```
Plot[ Q[t], { t, 0, 100}
```



```
Solve[ t Q[t] : 0, t]
```

Solve::ifun: Inverse functions are being used by Solve, so some solutions may not be found; use Reduce for complete solution info

```
{{ t -> 72.9165}}
```

```
Q[72.9164602138331]
1.14881 10^7
```

So, the present flux of neutrons emitted by the PuBe source is 1.14881 x 10⁷ n/s.

Appendix D: MCNP Code for Neutron Howitzer Design

D.1 Aluminum Howitzer

Howitzer nominal dimensions for thermal neutron generation

c Cell cards for problem

```
2 0 (1:-7:15) $Void outside OD of can, top of can, btm of can
3 1 -7.82 (-1 2 -15 8 -21):(-1 7 -8):(21 -1 2 -15 8 18) $Steel can
4 3 -0.93 (-2 3 -15 14):(-2 5 -14 11 -21):(-2 3 -11 9):(-2 8 -9) &
    :(-2 -14 11 5 18) $Paraffin in can
5 3 -0.93 (-11 16 -4) $Paraffin UNDER source inside inner cylinder
6 3 -0.93 (-4 14 -15) $Paraffin OVER source inside inner cylinder
7 4 -0.001205 (-17 -2 6 21) $Air in beam tube
8 4 -0.001205 (12 -13 -6) $Air in manifold
9 4 -0.001205 (-16 10 -4) $Air under source in inner tube
10 2 -2.7 (-18 17 -1 6 21) $Aluminum inside beam tube
11 2 -2.7 (6 -5 -13 12 -21):(13 -14 4 -5): &
    (11 -12 4 -5):(21 6 -5 18 -13 11) $Aluminum inside manifold walls
12 2 -2.7 (-3 4 -15 14) $Aluminum inside inner tube above manifold
13 2 -2.7 (-3 4 -11 10):(-3 -10 9) $Aluminum inside inner tube below manifold
14 4 -0.001205 (-4 -14 13) $Air at TOP of manifold thickness
15 4 -0.001205 (-4 -12 11) $Air at BOTTOM of manifold thickness
16 4 -0.001205 (-17 -1 2 21) $Air in beam tube at end for flux count
```

c End of cell cards

c Beginning of surfaces

```
1 CZ 29.21    $OD of Can cylinder of radius 29.21 cm centered at origin
2 CZ 29.088588 $ID of Can cylinder of radius 29.08 cm centered at origin
3 CZ 2.8575    $OD of inside cylinder
4 CZ 2.54      $ID of inside cylinder
5 CZ 5.08      $OD of manifold
6 CZ 4.5974    $ID of manifold
7 PZ 0         $Bottom of can
8 PZ 0.121412  $Inside bottom of can
9 PZ 20.32     $Bottom of inner cylinder
10 PZ 20.8026  $Inside bottom of inner cylinder
11 PZ 31.75    $Bottom of manifold
12 PZ 32.2326  $Inside bottom of manifold
13 PZ 41.4274  $Top inside of manifold
14 PZ 41.91    $Top of manifold outside edge
15 PZ 73.66    $Top of poured wax in can
16 PZ 29.21    $Low edge of wax between PuBe and bottom of inner tube
17 C/X 0 36.83 2.07518 $ID of neutron beam tube
18 C/X 0 36.83 2.2225  $OD of neutron beam tube
19 PX 29.21    $Outside end of beam tube
```

```

c 20 SO 0 29.5 .5 $Sphere of radius .5cm centered at beam output
21 PX 0 $Bisecting plane for half manifold cell
c End of surfaces
MODE N P E
IMP:N,P 0 1 1 1 1 1 1 1 1 1 1 1 1 1 1 1
IMP:E 0 1 1 1 1 1 1 1 1 1 1 1 1 1 1 1
VOL 14J 0.39576 $manual vol of cell 16=(2x2.07518)x(pi/4)x(.12142)
c INSERT SOURCE TERMS HERE
SDEF POS=0 0 36.83 ERG=D1
SI1 L 5.00E-01 &
1.00E+00 &
1.50E+00 &
2.00E+00 &
2.50E+00 &
3.00E+00 &
3.50E+00 &
4.00E+00 &
4.50E+00 &
5.00E+00 &
5.50E+00 &
6.00E+00 &
6.50E+00 &
7.00E+00 &
7.50E+00 &
8.00E+00 &
8.50E+00 &
9.00E+00 &
9.50E+00 &
1.00E+01 &
1.05E+01
SP1 D 3.80E-02 &
4.90E-02 &
4.50E-02 &
4.20E-02 &
4.60E-02 &
6.20E-02 &
7.70E-02 &
8.30E-02 &
8.20E-02 &
7.60E-02 &
5.70E-02 &
4.20E-02 &
4.20E-02 &

```

5.20E-02 &
 5.40E-02 &
 5.10E-02 &
 3.80E-02 &
 1.70E-02 &
 1.80E-02 &
 2.20E-02 &
 7.00E-03
 c INSERT TALLY HERE
 F4:N 16 \$avg flux in cell 16 (steel can thickness at beam end)
 E4 0 & \$energy bins for the tally to count in MeV
 .025E-6 &
 .05E-6 &
 .1E-6 &
 .13E-6 &
 .2E-6 &
 .3E-6 &
 .4E-6 &
 .5E-6 &
 .6E-6 &
 .7E-6 &
 .8E-6 &
 .9E-6 &
 1E-6 &
 1 &
 2 &
 3 &
 4 &
 5 &
 6 &
 7 &
 8 &
 9 &
 10 &
 11 &
 12
 M1 6012 -0.005 26000 -0.995 \$Steel
 M2 13027 1 \$Aluminum
 M3 1001 -0.148605 6012 -0.851395 \$Paraffin Wax
 M4 7014 .784437 6000 .000151 8016 .210750 18000 .004671 \$Air
 NPS 5E6

D.2 PVC Howitzer

PVC Howitzer nominal dimensions for thermal neutron generation

c Cell cards for problem

2 0 (1:-7:15) \$Void outside OD of can, top of can, btm of can

3 1 -7.82 (-1 2 -15 8 -21):(-1 7 -8):(21 -1 2 -15 8 18) \$Steel can

4 3 -0.93 (-2 3 -15 14):(-2 5 -14 11 -21):(-2 3 -11 9):(-2 8 -9) &
:(-2 -14 11 5 18) \$Paraffin in can

5 3 -0.93 (-11 16 -4) \$Paraffin UNDER source inside inner cylinder

6 3 -0.93 (-4 14 -15) \$Paraffin OVER source inside inner cylinder

7 4 -0.001205 (-17 -2 6 21) \$Air in beam tube

8 4 -0.001205 (12 -13 -6) \$Air in manifold

9 4 -0.001205 (-16 10 -4) \$Air under source in inner tube

10 2 -1.406 (-18 17 -1 6 21) \$PVC inside beam tube

11 2 -1.406 (6 -5 -13 12 -21):(13 -14 4 -5): &

(11 -12 4 -5):(21 6 -5 18 -13 11) \$PVC inside manifold walls

12 2 -1.406 (-3 4 -15 14) \$PVC inside inner tube above manifold

13 2 -1.406 (-3 4 -11 10):(-3 -10 9) \$PVC inside inner tube below manifold

14 4 -0.001205 (-4 -14 13) \$Air at TOP of manifold thickness

15 4 -0.001205 (-4 -12 11) \$Air at BOTTOM of manifold thickness

16 4 -0.001205 (-17 -1 2 21) \$Air in beam tube at end for flux count

c End of cell cards

c Beginning of surfaces

1 CZ 29.21 \$OD of Can cylinder of radius 29.21 cm centered at origin

2 CZ 29.088588 \$ID of Can cylinder of radius 29.08 cm centered at origin

3 CZ 2.8575 \$OD of inside cylinder

4 CZ 2.54 \$ID of inside cylinder

5 CZ 5.08 \$OD of manifold

6 CZ 4.5974 \$ID of manifold

7 PZ 0 \$Bottom of can

8 PZ 0.121412 \$Inside bottom of can

9 PZ 20.32 \$Bottom of inner cylinder

10 PZ 20.8026 \$Inside bottom of inner cylinder

11 PZ 31.75 \$Bottom of manifold

12 PZ 32.2326 \$Inside bottom of manifold

13 PZ 41.4274 \$Top inside of manifold

14 PZ 41.91 \$Top of manifold outside edge

15 PZ 73.66 \$Top of poured wax in can

16 PZ 29.21 \$Low edge of wax between PuBe and bottom of inner tube

17 C/X 0 36.83 2.07518 \$ID of neutron beam tube

18 C/X 0 36.83 2.2225 \$OD of neutron beam tube

19 PX 29.20 \$Outside end of beam tube


```

c 20 S 0 27 36.83 2 $$Sphere of radius .5cm centered at beam output
21 PX 0      $$Bisecting plane for half manifold cell
c End of surfaces
MODE N P E
c IMP:N,P 0 1 1 1 1 1 1 1 1 1 1
c IMP:E  0 1 1 1 1 1 1 1 1 1 1
IMP:N,P  0 1 1 1 1 1 1 1 1 1 1 1 1 1 1 1
IMP:E    0 1 1 1 1 1 1 1 1 1 1 1 1 1 1 1
VOL 14J 0.4397
c INSERT SOURCE TERMS HERE
SDEF POS=0 0 36.83 ERG=D1
SI1 L 5.00E-01 &
1.00E+00 &
1.50E+00 &
2.00E+00 &
2.50E+00 &
3.00E+00 &
3.50E+00 &
4.00E+00 &
4.50E+00 &
5.00E+00 &
5.50E+00 &
6.00E+00 &
6.50E+00 &
7.00E+00 &
7.50E+00 &
8.00E+00 &
8.50E+00 &
9.00E+00 &
9.50E+00 &
1.00E+01 &
1.05E+01
SP1 D 3.80E-02 &
4.90E-02 &
4.50E-02 &
4.20E-02 &
4.60E-02 &
6.20E-02 &
7.70E-02 &
8.30E-02 &
8.20E-02 &
7.60E-02 &
5.70E-02 &

```

4.20E-02 &
 4.20E-02 &
 5.20E-02 &
 5.40E-02 &
 5.10E-02 &
 3.80E-02 &
 1.70E-02 &
 1.80E-02 &
 2.20E-02 &
 7.00E-03
 c INSERT TALLY HERE
 F4:N 16 \$avg flux in cell 16 (steel can thickness at beam end)
 E4 0 & \$energy bins for the tally to count in MeV
 .025E-6 &
 .05E-6 &
 .1E-6 &
 .13E-6 &
 .2E-6 &
 .3E-6 &
 .4E-6 &
 .5E-6 &
 .6E-6 &
 .7E-6 &
 .8E-6 &
 .9E-6 &
 1E-6 &
 1 &
 2 &
 3 &
 4 &
 5 &
 6 &
 7 &
 8 &
 9 &
 10 &
 11 &
 12
 M1 6012 -0.005 26000 -0.995 \$Steel
 M2 1001 -0.048382 6012 -0.384361 17000 -0.567257 \$PVC pipe
 M3 1001 -0.148605 6012 -0.851395 \$Paraffin Wax
 M4 7014 .784437 6000 .000151 8016 .210750 18000 .004671 \$Air
 NPS 5E6

Appendix E: MCNP Code for Graphite Pile Differential Neutron Flux

E.1 Differential Neutron Flux at the diode

Pile minus a half-stringer for neutron flux on diode

c Cell cards for problem

2 0 (-1:2:-4:7:8:-11) \$Void outside pile

c Diode Box

3 3 -2.7 (12 -13 15 -14 -17 16) \$silicon filled

c Missing Stringer

4 2 -0.001205 (-5 6 3 -2 -9 10)#(12 -13 15 -14 -17 16) \$air filled

c Graphite pile minus missing stringer

5 1 -1.7 (-8 9 -2 1 4 -7):(-10 11 -2 1 4 -7):(-9 10 4 -6 1 -2): &

(-9 10 5 -7 1 -2):(-9 10 1 -3 6 -5) \$graphite filled

c End of cell cards

c Beginning of surfaces

c Top View of Pile, origin is pt source location

1 PX -63.5 \$122 solid left wall

2 PX 63.5 \$122 holed right wall

3 PX -5.5 \$inside wall of missing stringer

4 PY -66 \$127 upper wall

5 PY 5 \$top of removed stringer hole

6 PY -5 \$bottom of removed stringer hole

7 PY 56 \$127 bottom wall

c Side View of Pile

8 PZ 147 \$top of Pile

9 PZ 20 \$top of removed stringer hole

10 PZ 10 \$bottom of removed stringer hole

11 PZ -35.5 \$bottom of pile

c Diode box for flux measurement

12 PX -0.5

13 PX 0.5

14 PY 0.5

15 PY -0.5

16 PZ 12.7

17 PZ 13.7

c End of surfaces

MODE N P E

c IMP:N,P 0 1 1

c IMP:E 0 1 1

IMP:N,P 0 1 1 1

```

IMP:E 0 1 1 1
VOL 1J 1.000 $manually entered volume of diode box as 1 cm3
SDEF POS=0 0 9 ERG=D1
SI1 L 5.00E-01 &
1.00E+00 &
1.50E+00 &
2.00E+00 &
2.50E+00 &
3.00E+00 &
3.50E+00 &
4.00E+00 &
4.50E+00 &
5.00E+00 &
5.50E+00 &
6.00E+00 &
6.50E+00 &
7.00E+00 &
7.50E+00 &
8.00E+00 &
8.50E+00 &
9.00E+00 &
9.50E+00 &
1.00E+01 &
1.05E+01
SP1 D 3.80E-02 &
4.90E-02 &
4.50E-02 &
4.20E-02 &
4.60E-02 &
6.20E-02 &
7.70E-02 &
8.30E-02 &
8.20E-02 &
7.60E-02 &
5.70E-02 &
4.20E-02 &
4.20E-02 &
5.20E-02 &
5.40E-02 &
5.10E-02 &
3.80E-02 &
1.70E-02 &
1.80E-02 &

```

2.20E-02 &
 7.00E-03
 c INSERT TALLY HERE
 F4:N 3 \$avg flux in cell 3, diode box
 E4 0 & \$energy bins for the tally to count in MeV
 .025E-6 &
 .05E-6 &
 .1E-6 &
 .13E-6 &
 .2E-6 &
 .3E-6 &
 .4E-6 &
 .5E-6 &
 .6E-6 &
 .7E-6 &
 .8E-6 &
 .9E-6 &
 1E-6 &
 1 &
 2 &
 3 &
 4 &
 5 &
 6 &
 7 &
 8 &
 9 &
 10 &
 11 &
 12
 M1 6012 -1 \$Graphite
 M2 7014 .784437 6000 .000151 8016 .210750 18000 .004671 \$Air
 M3 14000 -1 \$Silicon
 NPS 1E8

E.2 Differential Neutron Flux at the diode with a Cd absorber

Pile minus a half-stringer for neutron flux on diode
c Uses sphere and Cd covering
c Cell cards for problem
2 0 (-1:2:-4:7:8:-11) \$Void outside pile
c Diode Ball
3 3 -2.7 (-18) \$silicon filled sphere
c 3 3 -2.7 (12 -13 15 -14 -17 16) \$silicon filled box
c Missing Stringer
4 2 -0.001205 (-5 6 3 -2 -9 10)#(-19) \$air filled except Cd cover
c 4 2 -0.001205 (-5 6 3 -2 -9 10)#(12 -13 15 -14 -17 16) \$air filled
c Graphite pile minus missing stringer
5 1 -1.7 (-8 9 -2 1 4 -7):(-10 11 -2 1 4 -7):(-9 10 4 -6 1 -2): &
(-9 10 5 -7 1 -2):(-9 10 1 -3 6 -5) \$graphite filled
c Cadmium cover over diode ball
6 4 -8.65 (-19 18) \$cadmium cover over diode sphere
c End of cell cards

c Beginning of surfaces
c Top View of Pile, origin is pt source location
1 PX -63.5 \$122 solid left wall
2 PX 63.5 \$122 holed right wall
3 PX -5.5 \$inside wall of missing stringer
4 PY -66 \$127 upper wall
5 PY 5 \$top of removed stringer hole
6 PY -5 \$bottom of removed stringer hole
7 PY 56 \$127 bottom wall
c Side View of Pile
8 PZ 147 \$top of Pile
9 PZ 20 \$top of removed stringer hole
10 PZ 10 \$bottom of removed stringer hole
11 PZ -35.5 \$bottom of pile
c Diode box for flux measurement
18 SZ 13.2 0.620345 \$Sphere of r=.620345,vol=1, ctrd in 'diode box'
19 SZ 13.2 0.69655 \$r= 0.6203 + 0.0763(0.03") = .69655 cm radius of Cd
c End of surfaces

MODE N P E
IMP:N,P 0 1 1 1 1
IMP:E 0 1 1 1 1
VOL 1J 1.000 \$manually entered volume of diode box as 1 cm3
SDEF POS=0 0 9 ERG=D1

SI1 L 5.00E-01 &

1.00E+00 &

1.50E+00 &

2.00E+00 &

2.50E+00 &

3.00E+00 &

3.50E+00 &

4.00E+00 &

4.50E+00 &

5.00E+00 &

5.50E+00 &

6.00E+00 &

6.50E+00 &

7.00E+00 &

7.50E+00 &

8.00E+00 &

8.50E+00 &

9.00E+00 &

9.50E+00 &

1.00E+01 &

1.05E+01

SP1 D 3.80E-02 &

4.90E-02 &

4.50E-02 &

4.20E-02 &

4.60E-02 &

6.20E-02 &

7.70E-02 &

8.30E-02 &

8.20E-02 &

7.60E-02 &

5.70E-02 &

4.20E-02 &

4.20E-02 &

5.20E-02 &

5.40E-02 &

5.10E-02 &

3.80E-02 &

1.70E-02 &

1.80E-02 &

2.20E-02 &

7.00E-03

c INSERT TALLY HERE

F4:N 3 \$avg flux in cell 3, diode 'ball'
 E4 0 & \$energy bins for the tally to count in MeV
 .025E-6 &
 .05E-6 &
 .1E-6 &
 .13E-6 &
 .2E-6 &
 .3E-6 &
 .4E-6 &
 .5E-6 &
 .6E-6 &
 .7E-6 &
 .8E-6 &
 .9E-6 &
 1E-6 &
 1 &
 2 &
 3 &
 4 &
 5 &
 6 &
 7 &
 8 &
 9 &
 10 &
 11 &
 12
 M1 6012 -1 \$Graphite
 M2 7014 .784437 6000 .000151 8016 .210750 18000 .004671 \$Air
 M3 14000 -1 \$Silicon
 M4 48000 -1 \$Cadmium
 NPS 1E6

Appendix F: Source and Detector Data Sheets

F.1 PuBe Source.

The following specifications were used for AFIT source T022.

Transmitted from AFIT - SEP

SHIPPING DATA
PLUTONIUM NEUTRON SOURCE
MONSANTO RESEARCH CORPORATION
MOUND LABORATORY
MIAMISBURG, OHIO

TO: MCLI-SE-Phys Dept.
Wright-Patterson Air Force Base,
Ohio
Attn: Dr. George John

March 9, 1962
DATE OF SHIPMENT & CALIBRATION
W-P AFB will pick up

VIA _____
YOUR P.O. No. _____
LICENSE No. SNM-513
SS ALLOTMENT QUOTA No. 7000/SNM-513/410
NEUTRON SOURCE No. M-1170
WITHDRAWN FROM SBX-3101

1. TYPE OF SOURCE - PuBe
2. GRAMS OF BE - 39.28
3. GRAMS OF PU - 76.36
4. CONTAINER MATERIAL - Ta & S.S.
5. DIMENSIONS OF CONTAINER - INSIDE - 0.82" i. d. x 3.72" h
OUTSIDE - 1.02" o. d. x 5.52" h
6. METHOD OF SEALING - WELDED
7. NEUTRON EMISSION - 9.04×10^6 N/SEC
8. TOLERANCE DISTANCE IN AIR FOR 8 HOURS - 46 INCHES
(BASED ON 200 N/SEC/CM²)
55
SHIPPING CONTAINER IS A PARAFFIN-FILLED 15 GALLON DRUM
as per dwg.

SOURCE(S) IS IN A SLOT AT THE BOTTOM OF A PARAFFIN-FILLED TUBE WHICH MAY BE LIFTED AFTER REMOVING THE SEALED CLOSURE OF THE DRUM.

PRICE OF SOURCE \$710
PLUS COST OF SHIPPING CONTAINER 75
TOTAL \$785

REMARKS: Educational
THE TITLE TO THE PLUTONIUM USED IN THIS SOURCE
REMAINS WITH THE ATOMIC ENERGY COMMISSION.
This source is to be charged to
the Educational Program(Budget
Activity 8737.2).
/lg
CC: Dr. George John
M. R. Hertz
GROUP LEADER, SOURCES

U.S. GOVERNMENT CONTRACT NO. AT-33-1-GEN-53
F-2

F.2 Co-60 Source



**Isotope Products
Laboratories**

An Eckert & Ziegler Company

24937 Avenue Tibbitts
Valencia, California 91355

Tel 661•309•1010

Fax 661•257•8303

T-125

CERTIFICATE OF CALIBRATION GAMMA STANDARD SOURCE

Radionuclide:	Co-60	Customer:	WRIGHT PATTERSON AFB
Half-life:	5.272 ± 0.001 years	P.O. No.:	MEIER/VISA
Catalog No.:	GF-060-M	Reference Date:	15-Sep-07 12:00 PST
Source No.:	1263-32-3	Contained Radioactivity:	10.26 µCi 379.6 kBq

Physical Description:

A. Capsule type:	M (25.4 mm OD x 3.18 mm THK)
B. Nature of active deposit:	Evaporated metallic salt
C. Active diameter/volume:	3 mm
D. Backing:	9.23 mg/cm ² kapton
E. Cover:	0.254 mm aluminized mylar

Radioimpurities:

None detected

Method of Calibration:

This source was assayed using gamma ray spectrometry.

Peak energy used for integration:	1173, 1333 keV
Branching ratio used:	0.9986, 0.9998 gammas per decay

Uncertainty of Measurement:

A. Type A (random) uncertainty:	± 0.6 %
B. Type B (systematic) uncertainty:	± 3.0 %
C. Uncertainty in aliquot weighing:	± 0.0 %
D. Total uncertainty at the 99% confidence level:	± 3.1 %

Notes:

- See reverse side for leak test(s) performed on this source.
- IPL participates in a NIST measurement assurance program to establish and maintain implicit traceability for a number of nuclides, based on the blind assay (and later NIST certification) of Standard Reference Materials (as in NRC Regulatory Guide 4.15).
- Nuclear data was taken from IAEA-TECDOC-619, 1991.
- This source has a working life of 5 years.

Daniel James Van Daken
Quality Control

23-Aug-07
Date

IPL Ref. No.: 1263-32

ISO 9001 CERTIFIED

Medical Imaging Laboratory
24937 Avenue Tibbitts Valencia, California 91355

Industrial Gauging Laboratory
1800 North Keystone Street Burbank, California 91504

F.3 LaBr(Ce) Detector Data Sheets

**SAINT-GOBAIN
CRYSTALS**

S/N : P572CS_C **AIR FORCE**

Informations / Informations

Designation SGCD : 10X10SE51_B380 N° de commande : 865541 Order Number Code produit : 22600115 Product Code N° de plan : 2-4-6990 Drawing Number	Designation PMT : XP28200FB N° de série PMT : 223 PMT Serial Number Isotope : 137Cs_662keV2048 Isotope N° de source : 50414 Source Number
--	---

Spectre / Spectrum

Mesures nucléaires / Nuclear measurements

Haute Tension High Voltage	Résolution	Résolution	Pic / Vallée Peak To Valley	Intégrale Integral	Efficacité 1251 1251 Efficiency
778 V	-	-	-	-	-

Commentaires / Comments

Résolution @662KeV: 3.6%

DATE jeudi 26 février 2009
Chaine de contrôle CN004

Opérateur PM
VISA

**SAINT-GOBAIN
CRYSTALS**

S/N : P902CS_B **AIR FORCE**

Informations / Informations

Designation SGCD : 10X10SE51_B380 N° de commande : 865541 Order Number Code produit : 22600115 Product Code N° de plan : 2-4-6990 Drawing Number	Designation PMT : XP28200FB N° de série PMT : 244 PMT Serial Number Isotope : 137Cs_662keV2048 Isotope N° de source : 50414 Source Number
--	---

Spectre / Spectrum

Mesures nucléaires / Nuclear measurements

Haute Tension High Voltage	Résolution	Résolution	Pic / Vallée Peak To Valley	Intégrale Integral	Efficacité 1251 1251 Efficiency
823 V	-	-	-	-	-

Commentaires / Comments

Résolution @662KeV: 3.3%

DATE lundi 30 mars 2009
Chaine de contrôle CN004

Opérateur PM
VISA

**SAINT-GOBAIN
CRYSTALS**

S/N : P572CO_C **AIR FORCE**

Informations / Informations

Designation SGCD : 10X10SE51_B380 N° de commande : 865541 Order Number Code produit : 22600115 Product Code N° de plan : 2-4-6990 Drawing Number	Designation PMT : XP28200FB N° de série PMT : 223 PMT Serial Number Isotope : 57Co_122keV2048 Isotope N° de source : 50082 Source Number
--	--

Spectre / Spectrum

Mesures nucléaires / Nuclear measurements

Haute Tension High Voltage	Résolution	Résolution	Pic / Vallée Peak To Valley	Intégrale Integral	Efficacité 1251 1251 Efficiency
924 V	-	-	-	-	-

Commentaires / Comments

Résolution @122KeV: 7.3%

DATE jeudi 26 février 2009
Chaine de contrôle CN004

Opérateur PM
VISA

**SAINT-GOBAIN
CRYSTALS**

S/N : P902CO_B **AIR FORCE**

Informations / Informations

Designation SGCD : 10X10SE51_B380 N° de commande : 865541 Order Number Code produit : 22600115 Product Code N° de plan : 2-4-6990 Drawing Number	Designation PMT : XP28200FB N° de série PMT : 244 PMT Serial Number Isotope : 57Co_122keV2048 Isotope N° de source : 50082 Source Number
--	--

Spectre / Spectrum

Mesures nucléaires / Nuclear measurements

Haute Tension High Voltage	Résolution	Résolution	Pic / Vallée Peak To Valley	Intégrale Integral	Efficacité 1251 1251 Efficiency
988 V	-	-	-	-	-

Commentaires / Comments

Résolution @122KeV: 7.4%

DATE lundi 30 mars 2009
Chaine de contrôle CN004

Opérateur PM
VISA

Appendix G: BF₃ Calculations

G.1 Calculated thermal neutron flux using a BF₃ detector

```
% Plot the 1 inch windowed thick Cd cover BF3 Data
clear all
close all
clc
BacklGap = xlsread('BF3ThickSpectraData.xlsx', 'BF3ThickBacklGap');
BackNoGap = xlsread('BF3ThickSpectraData.xlsx', 'BF3ThickBackNoGap');
BF3PileUp = xlsread('BF3ThickSpectraData.xlsx', 'BF3ThickPile1InchUp');
BF3PileDown = xlsread('BF3ThickSpectraData.xlsx',
'BF3ThickPile1InchDn');
BF3PileCdUp = xlsread('BF3ThickSpectraData.xlsx', 'BF3PileCdUp');
BF3PileCdDown = xlsread('BF3ThickSpectraData.xlsx', 'BF3PileCdDn');
%% Calculate macroscopic Cross-section
R = 0.0820574587; %L atm / K mol
T = 305.3; %90 F
P = 0.9; %atm
VoverN = R*T*(1/P)*1000; %cm3/mol
B10Xsection = 3840E-24; %cm2/atom for thermal neutrons
Sigma = (6.02E23/VoverN)*B10Xsection; %1/cm
%% PLOT BACK OF HOWITZER DATA, PuBe Up Only
BackCount = BacklGap-BackNoGap;
BackCount(:,1) = BacklGap(:,1); %put the first column back in
for i = 1:1024
    if BackCount(i,2) < 0
        BackCount(i,2) = 0;
    end
end
BackCountTotal = sum( BackCount(80:1023,2) );
BackCountPerSec = BackCountTotal/3600;
OD = 1.008; %in
WallThick = 0.0825; %inch
BackCountWindow = 1; %inch
BackCountActVol = (pi*((OD/2)-WallThick)^2*BackCountWindow)*16.387064;
%in3 to cm3
BackCountFlux = BackCountTotal*(1/3600)*(1/BackCountActVol)*(1/Sigma);
figure(1)
plot( BackCount(:,1),BackCount(:,2), '-' );
xlabel('Channel');
ylabel('Count');
set(gca, 'XMinorTick', 'on')
axis([70 500 0 5500]);
legend('5.25" back, 17" up, Source Up: 57cps, 75[n/cm2 s]',2);
hold on
plot( BacklGap(:,1),BacklGap(:,2), '-.' );
hold on
plot( BackNoGap(:,1),BackNoGap(:,2), '-.' );
%% PLOT FRONT OF HOWITZER DATA PuBe in down positions with 1" window
Down = BF3PileDown-BF3PileCdDown;
Down(:,1) = BF3PileDown(:,1); %put the first column back in
for i = 1:1024
    if Down(i,2) < 0
        Down(i,2) = 0;
```

```

    end
end
DownTotal = sum( Down(75:1023,2) );
DownPerSec = DownTotal/3600;
FrontCountWindow = 1; %inch
FrontCountActVol = (pi*((OD/2)-
WallThick)^2*FrontCountWindow)*16.387064; %in3 to cm3
FrontCountFluxDn = DownTotal*(1/3600)*(1/FrontCountActVol)*(1/Sigma);
figure(2)
plot( Down(:,1),Down(:,2), '-' );
xlabel('Channel');
ylabel('Count');
set(gca,'XMinorTick','on')
axis([70 500 0 6500]);
legend('At Diode, PuBe Dn: 61cps, 81[n/cm2 s]',2);
hold on
plot( BF3PileDown(:,1),BF3PileDown(:,2), '-.' );
hold on
plot( BF3PileCdDown(:,1),BF3PileCdDown(:,2), '-.' );
%% PLOT FRONT OF HOWITZER DATA PuBe in Up position, 1" window
Up = BF3PileUp-BF3PileCdUp;
Up(:,1) = BF3PileUp(:,1); %put the first column back in
for i = 1:1024
    if Up(i,2) < 0
        Up(i,2) = 0;
    end
end
UpTotal = sum( Up(75:1023,2) );
UpPerSec = UpTotal/3600;
UpOpen = sum( BF3PileUp(75:1023,2) );
UpCd = sum( BF3PileCdUp(75:1023,2) );
UpNet = UpOpen-UpCd;
FluxUp = UpTotal*(1/3600)*(1/FrontCountActVol)*(1/Sigma);
figure('Color',[1 1 1]);
plot( Up(:,1),Up(:,2), 'k' );
xlabel('Channel');
ylabel('Count');
set(gca,'XMinorTick','on')
axis([70 500 0 12000]);
legend('At Diode, PuBe Up: 129cps, 170[n/cm2 s]',2);
hold on
plot( BF3PileUp(:,1),BF3PileUp(:,2), '--b' );
hold on
plot( BF3PileCdUp(:,1),BF3PileCdUp(:,2), ':r' );
h = legend('Net Counts', 'Cd Covered Tube Counts', 'Open Tube Counts',0);
figure('Color',[1 1 1]);
plot( Up(:,1),Up(:,2), 'k' );
xlabel('Channel');
ylabel('Count');
set(gca,'XMinorTick','on')
axis([70 500 0 12000]);
legend('At Diode, PuBe Up: 129cps, 170[n/cm2 s]',2);
h = legend('BF3 Tube Net Counts',0);

```

G.2 Neutron attenuation of the Cd shield

```
% Plot the I vs Io for neutron attenuation of Cd
clear all
close all
clc
CdXsxn = xlsread('BandCdXsections.xls', 'CdNAT');
figure(1)
loglog( CdXsxn(:,1),CdXsxn(:,2), '-' );
ylabel('Cross-Section [b]');
xlabel('Energy [MeV]');
set(gca, 'XMinorTick', 'on')
legend('Natural Cd Neutron Cross Section',1);
%Choose energies below 10 eV, convert to eV, convert b to cm2
for i=1:5467
    if CdXsxn(i,1) <= 1E-5 % 10eV is 1E-5MeV
        CdX(i,1) = CdXsxn(i,1)*1E6; %convert to eV from MeV
        CdX(i,2) = CdXsxn(i,2)*1E-24; % b to cm2
    end
end
figure(2)
loglog( CdX(:,1),CdX(:,2), '-' );
ylabel('Cross-Section [cm2]');
xlabel('Energy [eV]');
set(gca, 'XMinorTick', 'on')
legend('Natural Cd Neutron Cross Section',1);
%% Cd thickness
x = 0.3277; %cm .043"=.10922 cm times 3 is .3277
%% Sigma
NA = 6.02E23; %atom/mol
rho = 8.648; %g/cm3
mw = 112.411; %g/mol
N = rho*NA*(1/mw); %nuclei/cm3
for i = 1:172
    IoverINot(i,1) = CdX(i,1); %first column is energy
    IoverINot(i,2) = exp( -CdX(i,2).*N.*x ); %second column is I/Io
end
for i = 1:172
    IoverINot1(i,1) = CdX(i,1); %first column is energy
    IoverINot1(i,2) = exp( -CdX(i,2).*N.*x/3 ); %second column is I/Io
end
for i = 1:172
    IoverINot2(i,1) = CdX(i,1); %first column is energy
    IoverINot2(i,2) = exp( -CdX(i,2).*N.*x/10 ); %second column is I/Io
end
figure('Color',[1 1 1]);
plot( IoverINot(:,1),IoverINot(:,2), 'k' );
hold on
plot( IoverINot1(:,1),IoverINot1(:,2), ':k' );
hold on
plot( IoverINot2(:,1),IoverINot2(:,2), '--k' );
xlabel('Energy [eV]');
set(gca, 'XMinorTick', 'on')
h = legend('0.33cm Cd','0.11cm Cd','0.033cm Cd',0);
axis([.025 5 0 1]);
```

G.3 Calibration of the BF₃ Tube using the Standard Graphite Pile

```
% Calibrate the BF3 Tube using the graphite pile
% This will determine an efficiency factor for the Tube as configured
clear all
close all
clc
% Input Standard Data
OldD4stdFlux = 5720; % n /cm2 s FROM AFIT STD PILE TM
OldD3stdFlux = 7920; % n /cm2 s FROM AFIT STD PILE TM
OldD2stdFlux = 6920; % n /cm2 s FROM AFIT STD PILE TM
PuBeActivity1961 = 8.92118E6; % n/s FROM MATHEMATICA PGM
PuBeActivity2009 = 1.13956E7; % n/s
OD = 1.008; %inch, BF3 Parameter
WallThick = 0.0825; %inch, BF3 Parameter
Window = 1; %inch, BF3 Parameter
% Input Pile Experimental Data
D4rawBF3win = 82901590; % cts
D3rawBF3win = 114887792; % cts
D2rawBF3win = 96523485; % cts **UPDATE THIS**
D4rawBF3cvrd = 28423306; % cts
D3rawBF3cvrd = 54636873; % cts
D2rawBF3cvrd = 49004385; % cts **UPDATE THIS**
PHStime = 3600; %s
% Calculate Corrected Flux to current PuBe activity
FM = PuBeActivity2009/PuBeActivity1961;
D4stdFlux = OldD4stdFlux*FM; % n /cm2 s
D3stdFlux = OldD3stdFlux*FM; % n /cm2 s
D2stdFlux = OldD2stdFlux*FM; % n /cm2 s
% Calculate macroscopic Cross-section
R = 0.0820574587; %L atm / K mol
T = 305.3; %90 F
P = 0.9; %atm
VoverN = R*T*(1/P)*1000; %cm3/mol
B10Xsection = 3840E-24; %cm2/atom for thermal neutrons
Sigma = (6.02E23/VoverN)*B10Xsection; %1/cm
% Calculate D4 Measured Flux
D4ActiveVol = (pi*((OD/2)-WallThick)^2*Window)*16.387064; %in3 to cm3
D4ExpFlux = (D4rawBF3win-
D4rawBF3cvrd)*(1/PHStime)*(1/D4ActiveVol)*(1/Sigma); %n/cm2 s
% Calculate D3 Measured Flux
D3ActiveVol = (pi*((OD/2)-WallThick)^2*Window)*16.387064; %in3 to cm3
D3ExpFlux = (D3rawBF3win-
D3rawBF3cvrd)*(1/PHStime)*(1/D3ActiveVol)*(1/Sigma); %n/cm2 s
% Calculate D2 Measured Flux
D2ActiveVol = (pi*((OD/2)-WallThick)^2*Window)*16.387064; %in3 to cm3
D2ExpFlux = (D2rawBF3win-
D2rawBF3cvrd)*(1/PHStime)*(1/D2ActiveVol)*(1/Sigma); %n/cm2 s
%% Plot the Standard and Measured Flux Data
figure('Color',[1 1 1]);
xlabel('Pile Position (Drawer)');
ylabel('Thermal Neutron Flux [n/cm2 s]');
bar([D2stdFlux,D2ExpFlux; D3stdFlux,D3ExpFlux; D4stdFlux,D4ExpFlux]);
set(gca,'XTickLabel',2:4)
xlabel('Pile Position (Drawer)');
```

```

ylabel('Thermal Neutron Flux [n/cm2 s]');
h=legend('Calibrated 0.025 eV flux in Graphite Pile','BF3 Uncalibrated
Flux', 0);
%% Determine an efficiency factor for the BF3 Tube
D4efficiency = D4stdFlux/D4ExpFlux; %this (x100) efficiency at D4
**CHECK THIS**
D3efficiency = D3stdFlux/D3ExpFlux;
D2efficiency = D2stdFlux/D2ExpFlux;
AvgEfficiency = (D4efficiency+D3efficiency+D2efficiency)/3;

```


Appendix H: Sr-90 Experiment Calculations

H.1 Determine the Beta flux into the diode from the Sr-90 source

```
%Determine the Beta Flux into the Diode from Sr-90
clear all
close all
clc

Dist_in = 0.75;%1.375; %Source to detector distance [in]
Sr90_Ci = 0.005973; %Current Sr90 activity [Ci], 25mCi on 28 Feb 1951

Sr90_Bq = Sr90_Ci * 3.7E10; % [Bq]
Dist_cm = Dist_in * 2.54; % [cm]
Air_rho = .0012; %[g/cm3]
Gd2O3_rho = 7.41; %[g/cm3]
Al_rho = 2.7; %[g/cm3]
Au_rho = 19.3; %[g/cm3]
SS_rho = 8; %[g/cm3]
Al_thick_cm = 0.000002 + 0.0254; %[cm] (contact + 10mil source window)
SS_thick_cm = 0.00508; %[cm] (2 mil Stainless Steel)
Au_thick_cm = 0.000005; %[cm]
Gd2O3_thick_cm = 0.000159; %[cm] thickness of non-depleted Gd2O3

Gamma_196_init = 195.8; %initial average beta energy from Sr90 [keV]
Gamma_934_init = 933.7; %initial average beta energy from Y90 [keV]

%% Air Loss
CSDA_196_air = 5.0E-2;% [g/cm3]
Range_196_air = CSDA_196_air / Air_rho; %(g/cm2) (cm3/g)=[cm]
SP_196_air = 2474 * Air_rho; %(keV cm2/g) (g/cm3)=[keV/cm]
CSDA_934_air = .4316;% [g/cm3]
Range_934_air = CSDA_934_air / Air_rho; %(g/cm2) (cm3/g)=[cm]
SP_934_air = 1681 * Air_rho; %(keV cm2/g) (g/cm3)=[keV/cm]

%% Al Loss
CSDA_196_al = 5.8E-2;% [g/cm3]
Range_196_al = CSDA_196_al / Al_rho; %(g/cm2) (cm3/g)=[cm]
SP_196_al = 2183 * Al_rho; %(keV cm2/g) (g/cm3)=[keV/cm]
CSDA_934_al = .4874;% [g/cm3]
Range_934_al = CSDA_934_al / Al_rho; %(g/cm2) (cm3/g)=[cm]
SP_934_al = 1492 * Al_rho; %(keV cm2/g) (g/cm3)=[keV/cm]

%% Au Loss
CSDA_196_au = 9.004E-2;% [g/cm3]
Range_196_au = CSDA_196_au / Au_rho; %(g/cm2) (cm3/g)=[cm]
SP_196_au = 1466 * Au_rho; %(keV cm2/g) (g/cm3)=[keV/cm]
CSDA_934_au = .6873;% [g/cm3]
Range_934_au = CSDA_934_au / Au_rho; %(g/cm2) (cm3/g)=[cm]
SP_934_au = 1122 * Au_rho; %(keV cm2/g) (g/cm3)=[keV/cm]

%% SS Loss
CSDA_196_SS = 6.556E-02;%[g/cm2] Iron
Range_196_SS = CSDA_196_SS / SS_rho; %(g/cm2) (cm3/g)=[cm]
SP_196_SS = 1947 * SS_rho; %(keV cm2/g) (g/cm3)=[keV/cm]
CSDA_934_SS = 5.420E-01;% [g/cm2]
Range_934_SS = CSDA_934_SS / SS_rho; %(g/cm2) (cm3/g)=[cm]
SP_934_SS = 1354 * SS_rho; %(keV cm2/g) (g/cm3)=[keV/cm]
```

```

%% Gadolina Loss (Uranium Oxide Proxy)
CSDA_196_Gd2O3 = 8.854E-2;% [g/cm3]
Range_196_Gd2O3 = CSDA_196_Gd2O3 / Gd2O3_rho; %(g/cm2) (cm3/g)=[cm]
SP_196_Gd2O3 = 1487 * Gd2O3_rho; %(kev cm2/g) (g/cm3)=[keV/cm]
CSDA_934_Gd2O3 = .6778;% [g/cm3]
Range_934_Gd2O3 = CSDA_934_Gd2O3 / Gd2O3_rho; %(g/cm2) (cm3/g)=[cm]
SP_934_Gd2O3 = 1136 * Gd2O3_rho; %(kev cm2/g) (g/cm3)=[keV/cm]
%% Stopping Power, Beta at Deposition Energy, non-E-loss Estimate
E_loss_196 = (SP_196_air*Dist_cm) + (SP_196_al*Al_thick_cm) +
(SP_196_au*Au_thick_cm) ...
+ (SP_196_Gd2O3*Gd2O3_thick_cm) + (SP_196_SS*SS_thick_cm) ; %
(keV/cm) (cm) = [keV]
E_loss_934 = (SP_934_air*Dist_cm) + (SP_934_al*Al_thick_cm) +
(SP_934_au*Au_thick_cm) ...
+ (SP_934_Gd2O3*Gd2O3_thick_cm)+(SP_934_SS*SS_thick_cm); %
(keV/cm) (cm) = [keV]

SP_alum_drop_196 = SP_196_al*Al_thick_cm;
SP_alum_drop_934 = SP_934_al*Al_thick_cm;
SP_SS_drop_196 = SP_196_SS*SS_thick_cm;
SP_SS_drop_934 = SP_934_SS*SS_thick_cm;

Gamma_196_finalSP = Gamma_196_init - E_loss_196; %[keV]
Gamma_934_finalSP = Gamma_934_init - E_loss_934; %[keV]
% This does not account for the fact that the energy is lowered at each
% step which will adjust the stopping powers
%% CSDA approximation
Drop_196_air = (Gamma_196_init / Range_196_air)*(Dist_cm);
%(keV/cm) (cm)=[keV]
Drop_934_air = (Gamma_934_init / Range_934_air)*(Dist_cm);
%(keV/cm) (cm)=[keV]
Drop_196_al = (Gamma_196_init / Range_196_al)*(Al_thick_cm);
%(keV/cm) (cm)=[keV]
Drop_934_al = (Gamma_934_init / Range_934_al)*(Al_thick_cm);
%(keV/cm) (cm)=[keV]
Drop_196_SS = (Gamma_196_init / Range_196_SS)*(SS_thick_cm);
%(keV/cm) (cm)=[keV]
Drop_934_SS = (Gamma_934_init / Range_934_SS)*(SS_thick_cm);
%(keV/cm) (cm)=[keV]
Drop_196_au = (Gamma_196_init / Range_196_au)*(Au_thick_cm);
%(keV/cm) (cm)=[keV]
Drop_934_au = (Gamma_934_init / Range_934_au)*(Au_thick_cm);
%(keV/cm) (cm)=[keV]
Drop_196_Gd2O3 = (Gamma_196_init / Range_196_Gd2O3)*(Gd2O3_thick_cm);
%(keV/cm) (cm)=[keV]
Drop_934_Gd2O3 = (Gamma_934_init / Range_934_Gd2O3)*(Gd2O3_thick_cm);
%(keV/cm) (cm)=[keV]
Gamma_196_final_CSDA = (Gamma_196_init)-
(Drop_196_air+Drop_196_al+Drop_196_SS+Drop_196_au+Drop_196_Gd2O3);
%[keV]
Gamma_934_final_CSDA = (Gamma_934_init)-
(Drop_934_air+Drop_934_al+Drop_934_SS+Drop_934_au+Drop_934_Gd2O3);
%[keV]

%% Results

```

```

% Beta energy blocked by 1.375" air and aluminum/SS window
Al_Block_196 = SP_alum_drop_196;
Al_Block_934 = SP_alum_drop_934;
Air_Block_196 = (SP_196_air*1.375);
Air_Block_934 = (SP_934_air*1.375);
SS_Block_196 = SP_SS_drop_196;
SS_Block_934 = SP_SS_drop_934;
No_Fraction_196 = Al_Block_196 + Air_Block_196 + SP_SS_drop_196;
No_Fraction_934 = Al_Block_934 + Air_Block_934 + SP_SS_drop_934;
%% R-Squared for Beta flux on diode
R2 = (Dist_cm)^2; %cm2
Basic_Flux = (Sr90_Bq * 2) / R2; %Beta/cm2 s, ignores low energy cut-
off
%% Determine advanced flux and Beta energies
Q1 = 546; %[keV]
Q2 = 2280.1; %[keV]
Q1_cutoff = 500;% 204; %set temp for nice plot...299; %this is the
energy of the betas that don't make it
Q2_cutoff = 500;%204;
step_size = 1; %[keV]
i=0;
Big_C = 1; %Matrix constant set equal to 1
c = 9.8; %[m/s]
mc2 = 511; %[keV]
%Q1
for i = 1:(Q1/step_size)
    T = step_size * i;
    Q1_spectrum(i,1) = T;
    Q1_spectrum(i,2) = ((Big_C)/c^5)*((T^2 + 2*T*mc2)^.5)*((Q1-
T)^2)*(T+mc2);
    % (1/keV){(keV)^2 + (keV)(keV)}^.5 (keV)^2 *keV = [kev]^4/[m/s]^5
end
Num_Integrate_Q1 = sum(Q1_spectrum(:,2));
Q1_spectrum(:,3) = Q1_spectrum(:,2)/Num_Integrate_Q1;
%check the normalized distribution
check = sum(Q1_spectrum(:,3)); %should equal unity
%%
figure('Color',[1 1 1]);
plot( Q1_spectrum(:,1), Q1_spectrum(:,3),'k' ) % position 3 is
normalized
    xlabel('Te[keV]');
    ylabel('N(Te), normalized');
hold on
for i = 1:(Q1/step_size)
    if Q1_spectrum(i,1) <= Q1_cutoff
        Q1_spectrum(i,4) = 0;
    else Q1_spectrum(i,4) = Q1_spectrum(i,3);
    end
end
%figure(2)
area( Q1_spectrum(:,1), Q1_spectrum(:,4), 'FaceColor',[0.0,0.0,0.0])
Transmitted_fraction = sum(Q1_spectrum(:,4));
%the normalized fraction emitted = [0.220222563676303]
%Q2
for i = 1:(Q2/step_size)

```

```

        T = step_size * i;
        Q2_spectrum(i,1) = T;
        Q2_spectrum(i,2) = ((Big_C)/c^5)*((T^2 + 2*T*mc2)^.5)*((Q2-
T)^2)*(T+mc2);
    end
    Num_Integrate_Q2 = sum(Q2_spectrum(:,2));
    Q2_spectrum(:,3) = Q2_spectrum(:,2)/Num_Integrate_Q2;
    %check the normalized distribution
    check2 = sum(Q2_spectrum(:,3)); %should equal unity
%%
figure('Color',[1 1 1]);
plot( Q2_spectrum(:,1), Q2_spectrum(:,3) )
    xlabel('Te[keV]');
    ylabel('N(Te), normalized');
hold on
for i = 1:(Q2/step_size)
    if Q2_spectrum(i,1) <= Q2_cutoff
        Q2_spectrum(i,4) = 0;
    else Q2_spectrum(i,4) = Q2_spectrum(i,3);
    end
end
%%
%figure(4)
area( Q2_spectrum(:,1), Q2_spectrum(:,4), 'FaceColor',[0.0,0.0,0.0])
Transmitted_fraction2 = sum(Q2_spectrum(:,4));
    %the normalized fraction emitted = [0.959610083044573]

%Plot the fraction that actually transmits
for i = 1:(Q1/step_size)
    Emit_Spectrum(i,1)= i;
    if Q1_spectrum(:,4) <= 0
    then Emit_Spectrum(i,2)= 0;
    else Emit_Spectrum(i,2)= Q1_spectrum(i,4);
    end
end
for i = 1:(Q2/step_size)
    if Q2_spectrum(:,4) <= 0
    then Emit_Spectrum(i,3)= 0;
    else Emit_Spectrum(i,3)= Q2_spectrum(i,4);
    end
    Emit_Spectrum(i,1) = i; %add empty columns for Q1 to equalize the
vectors
end
%%
Emit_Spectrum(Q1/step_size:Q2/step_size,2) = 0;
%Q1_spectrum(Q1/step_size:Q2/step_size,4) = 0;
%figure(5)
figure('Color',[1 1 1]);
area( Emit_Spectrum(:,1), Emit_Spectrum(:,2) )
    xlabel('Te[keV]');
    ylabel('N(Te), normalized');
hold on
area( Emit_Spectrum(:,1), Emit_Spectrum(:,3) )
%%
figure('Color',[1 1 1]); %add the emitted fractions

```

```

area( Emit_Spectrum(:,1), (Emit_Spectrum(:,2)+Emit_Spectrum(:,3)) )
    xlabel('Te[keV]');
    ylabel('N(Te), normalized');

%% Betas emitted calculated from energy distro spectrum
Beta_low = Sr90_Bq * Transmitted_fraction; %Sr90
Beta_high = Sr90_Bq * Transmitted_fraction2; %Y90
Flux_1_375 = (Beta_low + Beta_high)/(3.14*(4)*R2); %Beta /cm2 s {1E8}
[3E7 betas]
Diode_Area = 814000E-7; %cm, approximation as if Betas have LOS flight
Number_Diodes = 5;

Beta_Count = Number_Diodes*Diode_Area*Flux_1_375*3600; %[Beta/hour]
    % 1.5E11 Beta/hr [4.6E10]

%% Simplified Version

Sr_90_escape_fraction = 0.03;
Y_90_escape_fraction = 0.6;
Bq_escape =(Sr90_Bq*Sr_90_escape_fraction +
Sr90_Bq*Y_90_escape_fraction)
Beta_flux_simple = Bq_escape / (4*pi*Dist_in^2) %B/cm2 s, 2.2E7 at 3.5
cm
%%
%Plot both distributions Together
figure('Color',[1 1 1]);
plot( Q1_spectrum(:,1), Q1_spectrum(:,3),'k' ) %3 is normalized
hold on
plot( Q2_spectrum(:,1), Q2_spectrum(:,3),':k' )
xlabel('Te[keV]');
ylabel('N(Te), normalized');
h = legend('Sr-90 Beta Energy Distribution','Y-90 Beta Energy
Distribution',0);
%%
%compute counting efficiency
Count_p_75=100.2384E6;
Count_1p375=21.5127E6;
TCount_p_75=1.75E10;
TCount_1p375=5.23E9;
RelError_p75 = (TCount_p_75-Count_p_75)/(TCount_p_75+Count_p_75)
RelError_1p375= (TCount_1p375-Count_1p375)/(TCount_1p375+Count_1p375)
Eff_p75 = Count_p_75/TCount_p_75
Eff_1p375 = Count_1p375/TCount_1p375

```

H.2 Sr-90 Source Protocol

MEMORANDUM FOR RECORD

17 NOV 2009

SUBJECT: Protocol for Safety Review and Self Study Documentation

I am requesting that AFIT/ENP conduct a safety review of the experiment identified below.

Title of Experiment: $\text{Gd}_2\text{O}_3/\text{Si}$ diode interaction with beta-particles

Principle Investigators: MAJ Chris Young

Experiment's Location: Basement of Bldg. 470, Neutron Room

Personnel Involved: LTC John McClory

Date of Previous Peer Review: None

A self study was conducted and the hazards associated with the experiment are summarized below. Attached are all general guidelines, as well as experimental schematics. A copy of the WPAFB radiation guideline and this protocol will be posted at the experimental station.

DESCRIPTION OF EXPERIMENT: The experiment is designed to determine if a novel diode made from Gd_2O_3 deposited on Si can successfully produce an electrical signal in the presence of beta-particles. Successful signal generation is desired to corroborate neutron interactions in which auger electrons are produced within the diode.

Experimental procedures:

- 1. Personal Protective Equipment, Accountability, and Shielding:* All radiation sources will remain in the location for which they are signed out. If the source must change locations (e.g. room), a qualified person must sign it out and into the new location. The use of the Sr-90 source (AFIT ID 00365) will require gloves and a lab coat. A survey meter with a beta-window will be used to check for any contamination of the experiment by the source once it is placed back into storage. Any surface that has the potential to be contaminated will be tested using a survey meter with beta-window to include PPE. Aluminum shielding 0.25" thick will be employed to protect personnel in the room from beta emissions. The experiment will take place in the neutron room of Bldg. 470.
- 2. Mounting:* The source will rest on supports to facilitate a quick transition from storage into the shielded experiment area to reduce the time of exposure.
- 3. Measurements:* The signal from the diode will be recorded through a series of amplifiers using a multi-channel analyzer.

4. Cleanup and Monitoring: Because the source is sealed but has the potential to leak, anything it comes in contact with will be monitored for possible contamination. All experimental hardware, PPE, and the floor surrounding the experiment will be interrogated with an appropriate, beta-sensitive, survey meter for signs of contamination. Any contamination found will be immediately reported to the RSO and the experiment halted. The source is leak tested every 6 months. The last test showed no leakage on 28 Aug 2009.

SUMMARY OF MAJOR SAFETY ISSUES: Potential hazards are from Radioactive sources and High Voltages.

DETAILED SAFETY ANALYSIS:

Identify all hazardous chemicals use with this experiment.

Identify the location of all stored chemicals:

Identify all hazardous waste generated by this experiment:

Identify all ventilation requirements:

Identify all electrical hazards associated with this experiment:

Identify all laser hazards associated with this experiment:

Identify all source of ionizing radiation:

The Sr-90 source has an activity of 6 mCi. The beta decay of Sr-90 emits beta particles with an end-point energy of 546 keV. The daughter product, Y-90, also beta decays with particles of end-point energy 2.27 MeV. The half-life of Sr-90 is 28.7 years. The half-life of Y-90 is 64.1 hours.

Identify all other safety or bio-environmental hazards:

Sr-90 is a well-known bone-seeking compound due to its biological similarity to calcium. For this reason, proper PPE, handling procedures, and leak testing are used.

Identify all available protective equipment:

PPE: Lab coat, gloves, dosimetry.

Shielding: For shielding requirements, the more energetic beta energies of Y-90 were considered with a range of 1.1 g/cm^2 in air. Sea level air on a standard day has a density of 0.0012 g/cm^3 (Cerber). The farthest traveling beta-particle would be stopped in air in 916 cm [$(1.1 \text{ g/cm}^2 / 0.0012 \text{ g/cc}) = 916 \text{ cm}$]. Considering that the preponderance of beta-particles would be from the Sr-90 itself, the range of a 0.54 MeV beta has a range in air of 0.12 g/cm^2 which will travel 100 cm. The source will only be handled to place it onto the experimental apparatus or put it back into its storage container. A 0.25 in plastic shield is fixed to the source handle and is designed to protect the user from beta radiation when holding the source. This shield will stop most of the expected beta particles but the most energetic betas (2.3 MeV) require 0.37 in of plexiglass (Cerber). Aluminum plate will also be used to shield the experiment from the researcher. 0.2 in of

Al will stop a 2.3 MeV beta particle. The aluminum that will be employed is 0.25 inches thick. The concrete floor and walls of the neutron room are thicker than the minimum 0.2 in required to stop the most energetic beta emission and will contain the sources effects to the lab.

Identify all exposure monitors, alarms, or detectors:

A Ludlum model 2224-1 ratemeter in conjunction with a Ludlum model 43-89 probe will be used to detect beta activity.

Describe all emergency plans and procedure:

In the case of an emergency, the radiation source being used will be shielded and secured prior to implementation of AFIT approved evacuation plan. In the event of a fire or other similar event, the investigator will ensure that the responders are aware of the additional consideration.

The source is solid. Liquid spills will not be an issue.

In the event of an accident or emergency, the RSO will be notified as quickly as possible.

Identify all unresolved safety and bio-environmental issues:

Identify and limitation currently imposed by safety issues:

Recommendations for improving safety conditions:

Miscellaneous Issues:

I recommend conduction of this experiment as described and specified above. I am prepared to discuss this self study with the AFIT/ENP Safety Committee.

Attachments: (***Omitted for this Appendix***)

Attachment A: Guidelines for Working with Radioactive Material

Attachment B: Guidelines for Working with High Voltage/High Current Equipment

Attachment C: Basic Experimental Setup

Attachment D: AFIT Radiation Safety Program

Attachment E: WPAFB I 40-201 (2007)

Attachment F: Drawing of Sr-90 Source

MAJ Chris Young

AFIT/ENP

Appendix I: MCNP Code for gamma ray energy deposition in the diode

I.1 Energy deposition in the diode from a PuBe photon spectrum

Energy deposition in cylinder diode from gamma source

c Cell cards for problem

2 5 -0.001205 -11 10 -1 \$ Free Air

3 5 -0.001205 -10 9 -1 \$ air

4 5 -0.001205 -9 8 -1 \$ Inner Air

5 1 -19.3 -8 7 -1 \$ Gold Contact

6 2 -2.7 -7 6 -1 \$ Al Contact

7 4 -7.41 -6 5 -1 \$ non depleted Gd2O3 layer

8 4 -7.41 -5 4 -1 \$ depleted Gd2O3 layer

9 3 -2.33 (-4 3 -1):(2 -3 -1) \$ depleted Si layer and diffusion vol

10 0 (1:11:-2) \$ VOID out cylinder, btm and top

c End of cell cards

c Beginning of surfaces

1 CZ .0407 \$ cylinder of radius .0407 cm centered at origin

2 PZ -6.022E-3 \$ Diffusion Length in Si

3 PZ 0 \$ Si Depletion Distance

4 PZ 1.590E-4 \$ Metallurgical Junction

5 PZ 1.592E-4 \$ Gd2O3 Depletion Distance

6 PZ 1.6924E-4 \$ Top of Gd2O3 and bottom of Al

7 PZ 1.712E-4 \$ Top of Al, bottom of Au

8 PZ 1.762E-4 \$ Top of Au, bottom of inner air

9 PZ 0.75 \$ Top of inner Air, bottom of Cadmium

10 PZ 0.826 \$ Top of Cadmium, bottom of free air

11 PZ 3.826 \$ Top of free air and void start

c End of surfaces

MODE P E

IMP:P 1 1 1 1 1 1 1 0

IMP:E 1 1 1 1 1 1 1 0

VOL 7J 1.61E-5 \$ VOLUME of depletion+diff Length ***CHECK THIS***

SDEF POS=0 0 1 PAR=2 ERG=D1 \$ ***Change position of SOURCE in X Y Z***

c GAMMA SPECTRUM

SI1 L 2.0E-02 &

4.0E-02 &

6.0E-02 &

8.0E-02 &

1.0E-01 &

1.2E-01 &

1.4E-01 &

1.6E-01 &
1.8E-01 &
2.0E-01 &
2.2E-01 &
2.4E-01 &
2.6E-01 &
2.8E-01 &
3.0E-01 &
3.2E-01 &
3.4E-01 &
3.6E-01 &
3.8E-01 &
4.0E-01 &
4.2E-01 &
4.4E-01 &
4.6E-01 &
4.8E-01 &
5.0E-01 &
5.2E-01 &
5.4E-01 &
5.6E-01 &
5.8E-01 &
6.0E-01 &
6.2E-01 &
6.4E-01 &
6.6E-01 &
6.8E-01 &
7.0E-01 &
7.2E-01 &
7.4E-01 &
7.6E-01 &
7.8E-01 &
8.0E-01 &
8.2E-01 &
8.4E-01 &
8.6E-01 &
8.8E-01 &
9.0E-01 &
9.2E-01 &
9.4E-01 &
9.6E-01 &
9.8E-01 &
1.0E+00

SP1 D 3.2E-02 &
6.5E-03 &
4.9E-01 &
2.9E-02 &
9.7E-02 &
3.2E-02 &
9.7E-03 &
9.1E-03 &
8.1E-03 &
9.7E-03 &
6.5E-03 &
4.9E-03 &
4.9E-03 &
6.5E-03 &
9.7E-03 &
2.3E-03 &
6.5E-03 &
1.3E-03 &
1.9E-01 &
6.5E-03 &
1.6E-02 &
1.6E-03 &
9.7E-04 &
9.7E-04 &
6.5E-03 &
9.7E-04 &
6.5E-04 &
4.9E-04 &
4.9E-04 &
4.5E-04 &
4.5E-04 &
4.2E-04 &
4.2E-04 &
3.9E-04 &
3.9E-04 &
3.6E-04 &
3.6E-04 &
3.2E-04 &
3.2E-04 &
2.9E-04 &
2.9E-04 &
2.6E-04 &
2.6E-04 &

2.3E-04 &
 2.3E-04 &
 1.9E-04 &
 1.9E-04 &
 1.6E-04 &
 1.6E-04 &
 1.3E-04
 c TALLY DATA
 F4:E 9 \$Flux avg in cell 9, MeV/cm2, diff vol
 E4 0 &
 2.0E-02 &
 4.0E-02 &
 6.0E-02 &
 8.0E-02 &
 1.0E-01 &
 1.2E-01 &
 1.4E-01 &
 1.6E-01 &
 1.8E-01 &
 2.0E-01 &
 2.2E-01 &
 2.4E-01 &
 2.6E-01 &
 2.8E-01 &
 3.0E-01 &
 3.2E-01 &
 3.4E-01 &
 3.6E-01 &
 3.8E-01 &
 4.0E-01 &
 4.2E-01 &
 4.4E-01 &
 4.6E-01 &
 4.8E-01 &
 5.0E-01 &
 5.2E-01 &
 5.4E-01 &
 5.6E-01 &
 5.8E-01 &
 6.0E-01 &
 6.2E-01 &
 6.4E-01 &
 6.6E-01 &

6.8E-01 &
 7.0E-01 &
 7.2E-01 &
 7.4E-01 &
 7.6E-01 &
 7.8E-01 &
 8.0E-01 &
 8.2E-01 &
 8.4E-01 &
 8.6E-01 &
 8.8E-01 &
 9.0E-01 &
 9.2E-01 &
 9.4E-01 &
 9.6E-01 &
 9.8E-01 &
 1.0E+00
 c MATERIALS
 M1 79197 1 \$Au
 M2 13027 1 \$Al
 M3 14000 1 \$Si
 M4 64000 2 8016 3 \$Gd2O3
 M5 7014 .784437 6000 .000151 8016 .210750 18000 .004671 \$Air
 M6 48000 1 \$Cadmium
 NPS 5E9

I.2 Energy deposition in the Cd-covered diode from a PuBe photon spectrum

Energy deposition in cylinder diode from gamma and neutron source

c Cell cards for problem

2 5 -0.001205 -11 10 -1 \$ Free Air

3 6 -8.65 -10 9 -1 \$ Cadmium

4 5 -0.001205 -9 8 -1 \$ Inner Air

5 1 -19.3 -8 7 -1 \$ Gold Contact

6 2 -2.7 -7 6 -1 \$ Al Contact

7 4 -7.41 -6 5 -1 \$ non depleted Gd2O3 layer

8 4 -7.41 -5 4 -1 \$ depleted Gd2O3 layer

9 3 -2.33 (-4 3 -1):(2 -3 -1) \$ depleted Si layer and diffusion vol

10 0 (1:11:-2) \$ VOID out cylinder, btm and top

c End of cell cards

c Beginning of surfaces

1 CZ .0407 \$ cylinder of radius .0407 cm centered at origin

2 PZ -6.022E-3 \$ Diffusion Length in Si

3 PZ 0 \$ Si Depletion Distance

4 PZ 1.590E-4 \$ Metallurgical Junction

5 PZ 1.592E-4 \$ Gd2O3 Depletion Distance

6 PZ 1.6924E-4 \$ Top of Gd2O3 and bottom of Al

7 PZ 1.712E-4 \$ Top of Al, bottom of Au

8 PZ 1.762E-4 \$ Top of Au, bottom of inner air

9 PZ 0.75 \$ Top of inner Air, bottom of Cadmium

10 PZ 0.826 \$ Top of Cadmium, bottom of free air

11 PZ 3.826 \$ Top of free air and void start

c End of surfaces

MODE P E

IMP:P 1 1 1 1 1 1 1 1 0

IMP:E 1 1 1 1 1 1 1 1 0

VOL 7J 1.61E-5 \$ VOLUME of depletion+diff Length

SDEF POS=0 0 1 PAR=2 ERG=D1

c GAMMA SPECTRUM

SI1 L 2.0E-02 &

4.0E-02 &

6.0E-02 &

8.0E-02 &

1.0E-01 &

1.2E-01 &

1.4E-01 &

1.6E-01 &

1.8E-01 &
2.0E-01 &
2.2E-01 &
2.4E-01 &
2.6E-01 &
2.8E-01 &
3.0E-01 &
3.2E-01 &
3.4E-01 &
3.6E-01 &
3.8E-01 &
4.0E-01 &
4.2E-01 &
4.4E-01 &
4.6E-01 &
4.8E-01 &
5.0E-01 &
5.2E-01 &
5.4E-01 &
5.6E-01 &
5.8E-01 &
6.0E-01 &
6.2E-01 &
6.4E-01 &
6.6E-01 &
6.8E-01 &
7.0E-01 &
7.2E-01 &
7.4E-01 &
7.6E-01 &
7.8E-01 &
8.0E-01 &
8.2E-01 &
8.4E-01 &
8.6E-01 &
8.8E-01 &
9.0E-01 &
9.2E-01 &
9.4E-01 &
9.6E-01 &
9.8E-01 &
1.0E+00
SP1 D 3.2E-02 &

6.5E-03 &
4.9E-01 &
2.9E-02 &
9.7E-02 &
3.2E-02 &
9.7E-03 &
9.1E-03 &
8.1E-03 &
9.7E-03 &
6.5E-03 &
4.9E-03 &
4.9E-03 &
6.5E-03 &
9.7E-03 &
2.3E-03 &
6.5E-03 &
1.3E-03 &
1.9E-01 &
6.5E-03 &
1.6E-02 &
1.6E-03 &
9.7E-04 &
9.7E-04 &
6.5E-03 &
9.7E-04 &
6.5E-04 &
4.9E-04 &
4.9E-04 &
4.5E-04 &
4.5E-04 &
4.2E-04 &
4.2E-04 &
3.9E-04 &
3.9E-04 &
3.6E-04 &
3.6E-04 &
3.2E-04 &
3.2E-04 &
2.9E-04 &
2.9E-04 &
2.6E-04 &
2.6E-04 &
2.3E-04 &

2.3E-04 &
 1.9E-04 &
 1.9E-04 &
 1.6E-04 &
 1.6E-04 &
 1.3E-04
 c TALLY DATA
 F4:E 9 \$Flux avg in cell 9, MeV/cm2, diff vol
 E4 0 &
 2.0E-02 &
 4.0E-02 &
 6.0E-02 &
 8.0E-02 &
 1.0E-01 &
 1.2E-01 &
 1.4E-01 &
 1.6E-01 &
 1.8E-01 &
 2.0E-01 &
 2.2E-01 &
 2.4E-01 &
 2.6E-01 &
 2.8E-01 &
 3.0E-01 &
 3.2E-01 &
 3.4E-01 &
 3.6E-01 &
 3.8E-01 &
 4.0E-01 &
 4.2E-01 &
 4.4E-01 &
 4.6E-01 &
 4.8E-01 &
 5.0E-01 &
 5.2E-01 &
 5.4E-01 &
 5.6E-01 &
 5.8E-01 &
 6.0E-01 &
 6.2E-01 &
 6.4E-01 &
 6.6E-01 &
 6.8E-01 &

7.0E-01 &
 7.2E-01 &
 7.4E-01 &
 7.6E-01 &
 7.8E-01 &
 8.0E-01 &
 8.2E-01 &
 8.4E-01 &
 8.6E-01 &
 8.8E-01 &
 9.0E-01 &
 9.2E-01 &
 9.4E-01 &
 9.6E-01 &
 9.8E-01 &
 1.0E+00
 c MATERIALS
 M1 79197 1 \$Au
 M2 13027 1 \$Al
 M3 14000 1 \$Si
 M4 64000 2 8016 3 \$Gd2O3
 M5 7014 .784437 6000 .000151 8016 .210750 18000 .004671 \$Air
 M6 48000 1 \$Cadmium
 NPS 9E9

Appendix J: Instrument Settings

Instrument Setting Group 1 - Coincident Gamma Detection Instrument Settings (Neutron Howitzer)											
Left Scintillator Circuit Linear Amplifier						Right Scintillator Circuit Linear Amplifier					
CG	FG	BLR	Input	Output	ST Constant	CG	FG	BLR	Input	Output	ST Constant
20	0.5	Auto	NEG	Unipolar	0.5	20	5.02	Auto	Neg	Unipolar	0.5
Diode Circuit											
Linear Amplifier						Multi-Channel Buffer				LV DC PWR	Scintillator
CG	FG	BLR	Input	Output	ST Constant	MC B	LLD	Zero	Live Time	Bias	HV
20	0.5	Auto	POS	Unipolar	0.5	2048	0.007	0.05	60 to 36E6	-1	770

Instrument Setting Group 2 - Current Mode Circuit (Neutron Howitzer)										
Linear Amplifier						Multi-Channel Buffer				LV DC PWR
CG	FG	BLR	Input	Output	ST Constant	MC B	LLD	Zero	Live Time	Bias
100	1.5	Auto	NEG	Unipolar	0.5	2048	2.28	0.05	3600	-1
Ammeter set to 2nA range										

Instrument Setting Group 3 -LaBr Scintillator (Graphite Pile Experiment)										
Linear Amplifier						Multi-Channel Buffer				LV DC PWR
CG	FG	BLR	Input	Output	ST Constant	MC B	LLD	Zero	Live Time	Bias
20	0.85	Auto	POS	Unipolar	1	2048	0.114	0.05	60 to 36E6	-1

Instrument Setting Group 4 - Sr-90 Experiment										
Linear Amplifier						Multi-Channel Buffer				LV DC PWR
CG	FG	BLR	Input	Output	ST Constant	MC B	LLD	Zero	Live Time	Bias
20	0.5	Auto	POS	Unipolar	0.5	2048	2.001	0.05	60 to 36E6	-1

Instrument Setting Group 5 - Cs-137 Experiment										
Linear Amplifier						Multi-Channel Buffer				LV DC PWR
CG	FG	BLR	Input	Output	ST Constant	MC B	LLD	Zero	Live Time	Bias
20	0.5	Auto	POS	Unipolar	0.5	2048	0.996	0.05	60 to 36E6	-1

Instrument Setting Group 6 - BF ₃ Detector Experiment										
Linear Amplifier						Multi-Channel Buffer				HV
CG	FG	BLR	Input	Output	ST Constant	MC B	LLD	Zero	Live Time	Bias
20	1.5	Auto	POS	Unipolar	2	2048	1.872	0.05	60 to 36E6	1200

Appendix K: Equipment List

Item	Manufacturer	Model	Serial #	Note	Experiment / Circuit
Voltage Regulator / Transient Surge Suppressor	Tripp-Lite	LCR-2400	na	75db at 1 MHz	
Digital Phosphor Oscilloscope	Tektronix	DPO7104	B022196		
Uninterruptable Power Supply	APC	BR1500LCD	3B0936X14564	1500VA	
Pico-Ammeter	Keithley	6485	0927008		Diode Circuit
Laptop Computer	Gateway	na	0040350828		
Multi-Channel Analyzer (Software)	GammaVision	A66-B32	na	V 6.01	
Low Voltage DC Power Supply	Mastech	HY3006D	237707		Diode Circuit
Multimeter	Fluke	179	85790382		
AFIT Standard Graphite Pile	American Machine & Foundry Co.	AF NETF Graphite Standard Pile	na	Installed July 1960, Calib. September 1961	
LaBr(Ce) Scintillator and Integrated PMT	St Gobain	10x10 SE51 Brilliance380	P902 / XP28200FB	Crystal / PMT	'Left' Scintillator Circuit
Linear Amplifier	ORTEC	572A	253A		'Left' Scintillator Circuit

Timing Single Channel Analyzer	ORTEC	551	3824T		'Left' Scintillator Circuit
Preamplifier	ORTEC	113	7945	Rev G.	'Left' Scintillator Circuit
LaBr(Ce) Scintillator and Integrated PMT	St Gobain	10x10 SE51 Brilliance380	P572/XP28200F B	Crystal / PMT	'Right' Scintillator Circuit
Linear Amplifier	ORTEC	572A	4753		'Right' Scintillator Circuit
Timing Single Channel Analyzer	ORTEC	551	3645		'Right' Scintillator Circuit
Preamplifier	ORTEC	113	7939	Rev G.	'Right' Scintillator Circuit
High Voltage Power Supply	ORTEC	556	2064	Dual Output	Coincident Gamma Circuit
Gate and Delay Generator	ORTEC	416A	3640	Rev 34	Coincident Gamma Circuit
Delay Line Amplifier	ORTEC	427A	163		Coincident Gamma Circuit
Delay Line Amplifier	ORTEC	427A	3745	Rev 22	Coincident Gamma Circuit
Delay Line Amplifier	ORTEC	427A	4369		Diode Circuit
Linear Amplifier	ORTEC	572A	536	Rev B	Diode Circuit / LaBr in Pile

Multi-Channel Buffer	ORTEC	926	337		Diode/LaBr Calibration
Pulser	ORTEC	480	06055791	Rev 29	Calibration & Testing
Preamplifier	ORTEC	142IH	2034	Rev 13	Diode Circuit
NIM Bin and Power Supply	ORTEC	4006	442		Diode/LaBr Circuit
Preamplifier	Amptek	A250CF	1537		Diode Circuit
Preamplifier	ORTEC	113	6606	Rev 0	BF ₃ Experiment
Multi-Channel Buffer	ORTEC	926	338		BF ₃ Experiment
Linear Amplifier	ORTEC	572A	4745		BF ₃ Experiment
High Voltage Power Supply	ORTEC	556	030156	Dual Output	BF ₃ Experiment
Laptop Computer	Gateway	na	0040350831		BF ₃ Experiment
BF ₃ Detector	Unknown	RS-P4-0812-217	H6058		BF ₃ Experiment

REFERENCES

- [1]. U.S. Nuclear Regulatory Commission, definition of Special Nuclear Material accessed August 2008, available: <http://www.nrc.gov/materials/sp-nucmaterials.html>.
- [2]. R.C. Runkle *et al.*, "Lynx: An unattended sensor system for detection of gamma-ray and neutron emissions from special nuclear materials," *Nuclear Instruments and Methods in Physics Research A*, vol. 598, 2009, pp. 815-825.
- [3]. Defense Threat Reduction Agency Mission, accessed August 2009, available: <http://www.dtra.mil/faq/FAQs.cfm>.
- [4]. Advanced Detector Development and Nuclear Forensics Research and Development Solicitation Number: HDTRA1-09-NTD-BAA, accessed August 2009, available: https://www.fbo.gov/index?s=opportunity&mode=form&id=eef5a2dd1ba47c1ac185905aa857246f&tab=core&_cview=1
- [5]. G. Choppin, J. Liljenzin, and J. Rydberg, *Radiochemistry and Nuclear Chemistry*, 3rd ed., Woburn, MA: Butterworth-Heinemann, 2002 p. 585.
- [6]. S. Fetter, T.B. Cochran, L. Grodzins, H.L. Lynch, M.S. Zucker, "Gamma-Ray Measurements of a Soviet Cruise-Missile Warhead," in *Science*, vol. 24-8, May 1990, pp. 828-834
- [7]. C.J. Bridgman, *Introduction to the Physics of Nuclear Weapons Effects*. USA: Defense Threat Reduction Agency, 2001.
- [8]. G.F. Knoll, *Radiation Detection and Measurement*, 3rd ed. Hoboken, NJ: John Wiley and Sons, 2000.
- [9]. J.E. Turner, *Atoms, Radiation, and Radiation Protection*, 3rd ed. Weinheim, Germany: Wiley-VCH Verlag GmbH and Co., 2007.
- [10]. D. Schultz, *et al.* "Single Neutron Pulse Counting with p-type Gd Doped HfO₂ Thin Film Heterojunctions with Silicon," unpublished.
- [11]. H.T. Motz, "Slow Neutron Capture Gamma-rays from Sodium and Cadmium," *Physical Review*, vol. 104-5, 1956, pp. 1353-1364.
- [12]. National Nuclear Data Center, Brookhaven National Laboratory Q-Value calculator, accessed August 2009, available: <http://www.nndc.bnl.gov/qcalc/qcalcr.jsp>
- [13]. L. Carlson, "Cobalt Doping of Semiconducting Boron Carbide using Cobaltocene," MS thesis, Department of Engineering Physics, Air Force Institute of Technology, Wright-Patterson AFB, OH, 2007.
- [14]. B. Blasy, "Neutron Detection Utilizing Gadolinium Doped Hafnium Oxide Films," MS thesis, Department of Engineering Physics, Air Force Institute of Technology, Wright-Patterson AFB, OH, 2008.

- [15]. K.S. Krane, *Introductory Nuclear Physics*, New York: John Wiley and Sons, 1988.
- [16]. M.A. Ali, V.A. Khitrov, A.M. Sokhovej, and A.V. Vojnov, "Properties of the ^{158}Gd compound state Gamma-decay cascades," *J. Phys. G: Nucl. Part. Phys.*, vol. 20, 1994, pp. 1943-1953.
- [17]. Y. Sakurai and T. Kobayashi, "Experimental Verification of the Nuclear Data of Gadolinium for Neutron Capture Therapy," *Nuclear Science and Technology*, sup. 2, Aug 2002, pp. 1294-1297.
- [18]. A. Holmes-Seidel and L. Adams, *Handbook of Radiation Effects*, 2nd Ed. New York: Oxford University Press, 2002.
- [19]. P.Y. Kuei and C.C. Hu, "Gadolinium oxide high-k dielectrics prepared by anodic oxidation," *Applied Surface Science*, vol. 254, 2008, pp. 5487-5491.
- [20]. J.A. Colon Santana, B. Nordell, N. Wu, A. Sokolov, P. Molnar, and J.I. Brand, "Comparison of cubic Gd_2O_3 with monoclinic Gd_2O_3 ," unpublished.
- [21]. G. Adachi and N. Imanaka, "The Binary Rare Earth Oxides," *Chem. Rev.* vol. 98, 1998, pp. 1479-1514.
- [22]. S.M. Sze, *Semiconductor Devices, Physics and Technology*. Hoboken, NJ: John Wiley and Sons, 2002 pp. 84-129.
- [23]. R.G. Williams III, C.J. Gesh, R.T. Pagh, *Compendium of Material Composition Data for Radiation Transport Modeling*. USA: Pacific Northwest National Laboratory under the Dept. of Energy, April 2006 p. 74.
- [24]. W.S. Rawls and H.G. Voss, "A Versatile, Inexpensive Neutron Howitzer," *American Journal of Physics*, vol. 34, iss. 12, Dec. 1966, pp. 1182-1184.
- [25]. H. Cember, *Introduction to Health Physics*. USA: McGraw-Hill, 1983, pp. 393-396.
- [26]. C.T. Nguyen, "Verification of the Pu239 content, isotopic composition, and age of plutonium in Pu-Be neutron sources by gamma-spectroscopy," *Nuclear Instruments & Methods in Physics Research*, vol. 251, 2006, pp. 227-236.
- [27]. AF NETF Graphite Standard Pile, USAF Technical Report No. WADD-TR-61-174, March 1962.
- [28]. Chart of the Nuclides, Korea Atomic Energy Research Institute(KAEIR), accessed Dec. 2009, Available: <http://atom.kaeri.re.kr/>
- [29]. J.G. Kereiakes and A.T. Krebs, *X-Radiography with Beta-Emitting Isotopes*. Radiobiology Dept., Army Medical Research Laboratory, 20 Dec. 1954, p. 2.
- [30]. J. Speers, "Characterizing a neutron energy spectrum using "forward-edge" neutron time-of-flight spectroscopic technique," MS thesis, Department of Engineering Physics, Air Force Institute of Technology, Wright-Patterson AFB, OH, 2008.

- [31]. Monte-Carlo Simulation of Electron Trajectory in Solids (CASINO) , accessed August 2009, available: <http://www.gel.usherbrooke.ca/casino/index.html>
- [32]. Monte Carlo N-Particle Transport Code System, Version 5, Release 1.51, Radiation Safety Informational Computation Center, Oak Ridge, TN, January 2009.
- [33]. Gamma Vision Software Package for Windows. Model A66-B32 Version 6.01. Advanced Measurement Technology, Inc., 2003.
- [34]. Mathematica. Version 7 for Windows, Release 7.0.0, Wolfram Research Inc. Nov 2008.
- [35]. MATLAB. Version 7.8.0.347, R2009a, The MathWorks, Inc. Feb 2009.
- [36]. DaVinci. Version Y-2006.06, Taurus Medici, Jun 2006.

REPORT DOCUMENTATION PAGE				Form Approved OMB No. 0704-0188	
Public reporting burden for this collection of information is estimated to average 1 hour per response, including the time for reviewing instructions, searching existing data sources, gathering and maintaining the data needed, and completing and reviewing this collection of information. Send comments regarding this burden estimate or any other aspect of this collection of information, including suggestions for reducing this burden to Department of Defense, Washington Headquarters Services, Directorate for Information Operations and Reports (0704-0188), 1215 Jefferson Davis Highway, Suite 1204, Arlington, VA 22202-4302. Respondents should be aware that notwithstanding any other provision of law, no person shall be subject to any penalty for failing to comply with a collection of information if it does not display a currently valid OMB control number. PLEASE DO NOT RETURN YOUR FORM TO THE ABOVE ADDRESS.					
1. REPORT DATE (DD-MM-YYYY) 25-03-2010		2. REPORT TYPE Master's Thesis		3. DATES COVERED (From - To) October 2009 – March 2010	
4. TITLE AND SUBTITLE Gadolinium Oxide / Silicon Thin Film Heterojunction Solid-State Neutron Detector				5a. CONTRACT NUMBER	
				5b. GRANT NUMBER	
				5c. PROGRAM ELEMENT NUMBER	
6. AUTHOR(S) Young, Christopher M., MAJ, USA				5d. PROJECT NUMBER na	
				5e. TASK NUMBER	
				5f. WORK UNIT NUMBER	
7. PERFORMING ORGANIZATION NAME(S) AND ADDRESS(ES) AND ADDRESS(ES) Air Force Institute of Technology Graduate School of Engineering and Management (AFIT/EN) 2950 Hobson Way Wright-Patterson AFB, OH 45433-7765				8. PERFORMING ORGANIZATION REPORT NUMBER AFIT/GNE/ENP/10M-10	
9. SPONSORING / MONITORING AGENCY NAME(S) AND ADDRESS(ES) Domestic Nuclear Detection Office ATTN: Mr. William Ulicny 245 Murray Drive, BLDG 410 Washington, DC 20528				10. SPONSOR/MONITOR'S ACRONYM(S) HSHQDC-08-X-00641	
				11. SPONSOR/MONITOR'S REPORT NUMBER(S)	
12. DISTRIBUTION / AVAILABILITY STATEMENT APPROVED FOR PUBLIC RELEASE; DISTRIBUTION UNLIMITED					
13. SUPPLEMENTARY NOTES					
14. ABSTRACT The internal conversion electron emission from the de-excitation of the Gd-158m nucleus was explored as a means for neutron detection. Thin film gadolinium oxide (Gd ₂ O ₃) and p-type silicon heterojunction diodes were produced using a supercritical water deposition process. Pulse height spectroscopy was conducted on the novel diodes while they were subjected to a moderated plutonium-beryllium (PuBe) source flux of 10 ⁴ thermal neutrons/cm ² s. Coincident gamma spectroscopy was employed to verify the 1107.6 keV photon emissions from the diode indicative of successful neutron capture by Gd-157 and the subsequent de-excitation of the Gd-158m nucleus. Neutron capture in the diodes could not be confirmed experimentally. The diodes were found to be sensitive to gamma rays between 10 and 20 keV.					
15. SUBJECT TERMS Gadolinium Oxide, Gd2O3, Gadolina, Neutron Detection					
16. SECURITY CLASSIFICATION OF:			17. LIMITATION OF ABSTRACT UU	18. NUMBER OF PAGES 171	19a. NAME OF RESPONSIBLE PERSON John W. McClory, LTC, USA
a. REPORT U	b. ABSTRACT U	c. THIS PAGE U			19b. TELEPHONE NUMBER (include area code) (937) 255-3636, ext7308